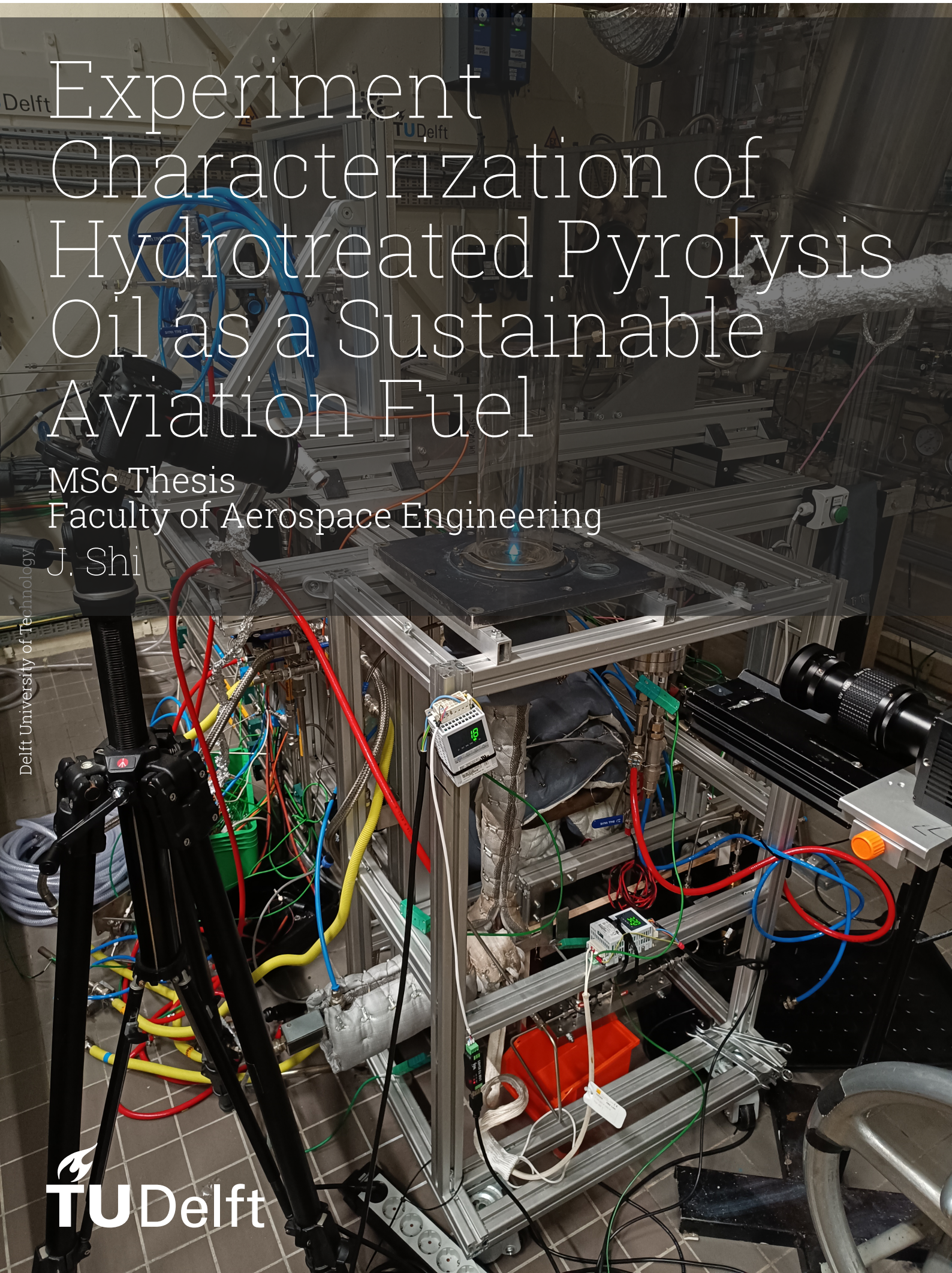

# Experiment Characterization of Hydrotreated Pyrolysis Oil as a Sustainable Aviation Fuel

MSc Thesis
Faculty of Aerospace Engineering

J. Shi

Delft University of Technology

TU Delft

# Experiment Characterization of Hydrotreated Pyrolysis Oil as a Sustainable Aviation Fuel

by

J. Shi

as a MSc thesis for the fulfillment of the degree Master of Science at TU Delft to be defended publicly on Tuesday April 22, 2025 at 13:00.

| | | |
|---|---|---|
| Supervisor: | Prof. dr. A. Gangoli Rao | |
| Daily Supervisor: | Dr. R.P. Sampat & Ir. K.A. Dave | |
| Thesis Committee: | Dr. S.M. Cazaux | Chairman |
| | Dr. F. De Domenico | Examiner |
| | Prof. dr. A. Gangoli Rao | Responsible supervisor |
| Thesis Duration: | Feb, 2024 - Apr, 2025 | |
| Faculty: | Faculty of Aerospace Engineering, Delft | |

TU Delft

# Preface

This thesis brings the journey of my university education in the Netherlands to a close. I have learned a lot and change a lot from my studies and environment I was exposed to. It has been an interesting and meaningful experience for me to study in the Netherlands.

I am grateful for the opportunity by my responsible supervisor Prof. dr. Arvind Gangoli Rao, and the guidance of my daily supervisors, Rishikesh P. Sampat and Kaushal A. Dave. Kaushal A. Dave is especially helpful during the middle part of my thesis. I am also thankful for the inputs provided by Dr. Francesca De Domenico and Sarah Link in my thesis. They have all played crucial roles in my thesis.

Above all, I would like to thank my parents for their continued support throughout my studies.

*J. Shi*
*Delft, April 2025*

# Abstract

As green transition in aviation continues to be pushed, SAFs becomes increasingly important. Hydrotreated Pyrolysis Oils (HPO) could potentially expand the ways SAFs could be produced. This thesis looks at the flame speed as well as NOx and CO emissions of this potential SAF when blended with Jet-A1. Experiment was performed in a bunsen burner setup, with flame speed determined from chemiluminescence images and emission data obtained from a gas analyzer. The results showed higher NOx emission, especially when equivalence ratio is close to stoichiometric condition. Higher CO was also observed for rich conditions, while no significant change in flame speed was seen. Experiment was also performed for Jet-A1 & hydrogen blend, which saw higher NO and CO emission at stoichiometric condition, and much higher flame speed.

# Contents

# Nomenclature

*If a nomenclature is required, a simple template can be found below for convenience. Feel free to use, adapt or completely remove.*

## Abbreviations

| Abbreviation | Definition |
|---|---|
| AAI | Axial Air Injection |
| AFR | Air to Fuel Ratio |
| APU | Auxiliary Power Unit |
| APPU | Advanced Propulsion & Power Unit |
| BTG | Biomass Technology Group BV |
| CO | Carbon Monoxide |
| $CO_2$ | Carbon Dioxide |
| DCN | Derived Cetane Number |
| FPBO | Fast Pyrolysis Bio-Oil |
| FT | Fischer-Tropsch |
| GHG | Greenhouse Gases |
| HEFA | Hydroprocessed Ester Fatty Acids |
| HPO | Hydrotreated Pyrolysis Oil |
| ICCD | intensified charge coupled device |
| Le | Lewis Number |
| LBO | Lean Blow-off |
| LDI | Lean Direct Injection |
| LDV | Laser Doppler Velocimetry |
| LHV | Lower Heating Value |
| LPP | Lean Premixed/Prevaporized |
| $NO_x$ | Nitrogen Oxides |
| P&ID | Power and Instrumentation Diagram |
| PIV | Particle Image Velocimetry |
| PLIF | Planar Laser Induced Fluorescence |
| PM | Particulate Matters |
| PSR | Perfectly Stirred Reactor |
| Re | Reynolds Number |
| RQL | Rich, Quick-Mix, Lean |
| SAF | Sustainable Aviation Fuels |
| UV | Ultraviolet |
| VBD | Vortex BreakDown |
| | ... |

## Symbols

| Symbol | Definition | Unit |
|---|---|---|
| $\bar{A}_f$ | Characteristic mean flame front area | [kg/m$^3$] |
| C | Concentration of mixture | |
| $C_{fuel}$ | Heat capacity of fuel | $J\ kg^{-1}K^{-1}$ |
| D | Diameter [m] | |

| Symbol | Definition | Unit |
|---|---|---|
| $d_p$ | Flame penetration distance | [m] |
| $d_q$ | Flame quenching distance | [m] |
| $d_j$ | Diameter of jet injection port | [m] |
| $G'_\phi$ | Axial flux of tangential momentum | $[kg\ m^2/s^2]$ |
| $G'_x$ | Axial flux of axial momentum | $[kg\ m/s^2]$ |
| $h_c$ | Convective heat transfer coefficient | $[W/m^2]$ |
| J | Momentum ratio | |
| L | Characteristic length | |
| $L_{vap}$ | Latent heat of vaporization | K/kg |
| $\dot{m}$ | mass flow rate | kg/s |
| $Nu_L$ | Nusselt Number | |
| P | Power | [W] |
| $Pr$ | Prandtl number | |
| $\dot{Q}$ | Volumetric flow rate | $[m^3/s]$ |
| $\dot{Q}_{conv}$ | Heat loss through convection | $[m^3/s]$ |
| $\dot{Q}_{rad}$ | Heat loss through radiation | $[m^3/s]$ |
| $R$ | Radius | [m] |
| $Ra_x$ | Rayleigh number | |
| $R_h$ | Hub radius | [m] |
| $R_t$ | Tip radius | [m] |
| $s_d$ | Local flame displacement speed | [m/s] |
| $S_l$ | Laminar flame speed | [m/s] |
| $S_n$ | Swirl number | |
| $S_{T,GC}$ | Turbulent global consumption speed | [m/s] |
| $S_{T,GD}$ | Turbulent global displacement speed | [m/s] |
| $S_{T,LC}$ | Turbulent local consumption speed | [m/s] |
| $S_{T,LD}$ | Turbulent local displacement speed | [m/s] |
| $S'$ | Geometrical swirl number | |
| $t$ | time | [s] |
| T | Temperature | K or $^\circ C$ |
| $U$ | Velocity in axial direction | [m/s] |
| $U_0$ | Bulk flow velocity | [m/s] |
| $U_s$ | Spatial unmixedness | |
| $u$ | Flame front velocity | [m/s] |
| $u_t$ | Local burning velocity for Figure 3.12 | [m/s] |
| V | Volume | $[m^2]$ |
| $W$ | Velocity in tangential direction | |
| $V_G$ | Velocity | [m/s] |
| $v$ | Flow velocity | [m/s] |
| X | Axial distance from fuel injection plane | [m] |
| $Y$ | Jet penetration distance | [m] |
| ... | | |
| $\alpha$ | Flame cone angle | $^\circ$ |
| $\alpha_s$ | Swirler angle | $^\circ$ |
| $\beta$ | Swirl Decay constant | |
| $\delta_q$ | equivalent distance | [m] |
| $\epsilon$ | Emissivity | |
| $\phi$ | Equivalence ratio | |
| $\rho$ | Density of burnt mixture | [kg/m$^3$] |
| $\rho_u$ | Density of unburnt mixture | [kg/m$^3$] |
| $\sigma$ | Stefan Boltzmann constant | $[Wm^{-2}K^{-4}]$ |
| ... | | |

# 1

# Introduction

The transition to green energy is a common problem encountered by many industries. Aviation is one of the sectors with the greatest challenge in reducing emsissions. It is projected that contribution of $CO_2$ emission from aviation would increase from about $3\%$ to $25\%$ by 2050 [1]. Hydrogen and Sustainable Aviation Fuels (SAFs) are the two areas where the focus of green transition in aviation is put. However, because of the challenges in cost and infrastructure encountered in the in the use of hydrogen [2], it is expected that SAF would still play the majority role in the reduction of greenhouse gases, accounting to over $85\%$ of fuel demand in 2050[1].

The use of SAFs in aviation would keep increasing as production increases. Currently, there are various certified pathways for producing SAF through ATSM D4054. These production pathways are continuously being expanded to expand the production of SAFs through other biomass. As outlined in ATSM D7566, SAFs produced through these certified methods can be used together with Jet-A1 up to a $50\%$. The thesis is part of PureJet project, where a new potential pathway of SAF production through pyrolysis of lignocellulosic biomass is being explored. The project is made up of a consortium of several companies, with Biomass Technology Group BV (BTG), SkyNRG, and TU Delft. BTG would produce the fuel, and TU Delft performing combustion analysis and experiments.

Because the use of hydrotreated pyrolysis oil (HPO) as SAf is relatively new, flame speed and emission data for the fuel is relatively scarce. The two properties, are however, of great importance. Flame speed directly relates to the stability of the flame, while combustion emissions influence the reduction of greenhouse gases obtained from the use of the fuel. The goal of this thesis is to evaluate the difference in emission and flame speed of this pyrolysis oil made by BTG relative to Jet-A1. An experiment was performed in a bunsen burner setup, followed a single PSR and freely propagating flame simulation was made to help understand the emission and flame speed results observed. A modification to existing setups in the lab is also proposed. The proposed setup would allow for swirl stabilized premixed prevaporized combustion experiments.

A background and problem statement of the thesis is first presented in chapter 2. Literature survey performed for the thesis is then presented next in chapter 3. This chapter includes an overview of the existing combustors for gas turbines, drop-in requirements, diagnostic techniques, and systems that can be used to ensure swirl stabilized premixed combustion. Research objective and research outline is then presented next in chapter 4, followed by the methods used for the research in chapter 5. Subsequently, analysis of the results obtained is presented in chapter 6, and the proposed modification is described in chapter 7. Finally, the thesis is concluded in chapter 8.

# 2

# Background and Problem Statement

This chapter will provide an overview of the relevant background information of the thesis. Aviation contribution to global greenhouse gas emission and potential alternative fuels will be provided in section 2.1 to section 2.3. section 2.4 will then describe the Purejet project, and subsection 2.4.1 the relevance of the thesis.

## 2.1. Aviation Greenhouse gases contribution and potential growth

Aviation is one of the major contributors to climate change, with an estimated contribution of $3.5\%$ to $4.9\%$ measured through radiative forcing [3] [4]. This contribution is expected to increase since the number of passengers is expected to increase at a rate of $4\%$ per year, and there is not a clear pathway yet for green transition in the sector to meet the goals set in the Paris agreement for 2100 [5]. Ivo Abrantes et al. [6] projected that the highest $CO_2$ reduction possible from the technological standpoint in the aviation sector is $15\%$ by 2050 from the value in 2005. The overall $CO_2$ and $No_x$ emission from the sector is projected to grow up to 3.6 times and 2.7 times, respectively from the value in year 2000 [7]. Largest GHG contribution comes from contrail cirrus, followed by $CO_2$ & $NO_x$, while effects of soot and sulfate on GHG contribution was undetermined [3].

Aside from emission reduction that can be achieved through increase in efficiency, studies also analyze the possibility of substituting polluting jet fuels with the main focus placed on renewable hydrogen and sustainable aviation fuels (SAF). The two possible substitutes will be discussed in more details in the following two subsections.

## 2.2. Sustainable Hydrogen as Alternative Fuel

Although green hydrogen has the potential to greatly reduce Greenhouse gases (GHG) emission, there are problems in introducing the fuel in a large scale. This is because of constraint in current production capacity and the high cost of hydrogen [2], but also also because of the high weight storage systems required [8] and airport logistical considerations [9]. Other problems include the low volumetric energy density of the fuel and high flame speed, which increases flashback propensity [10]. These factors mean that pure hydrogen cannot be used as a drop-in fuel, and is not an immediate substitute to jet fuels in the near future, although it may be a viable alternative in the long term [10] [11]. A large focus, is therefore, also placed on SAF as it is believed to be much more viable in the short term [12].

## 2.3. Sustainable Aviation Fuels (SAF)

SAF provides a possible alternative to current jet fuels,in achieving carbon neutrality. SAF has its own challenges in terms of its production/generation capacity and cost [9]. However, with its characteristic of being a drop-in fuel, it could still be part of a series of solutions for reduction in GHG emission in the future. This drop-in characteristic means the use of SAF as jet fuel-substitute does not typically require modifications to an aircraft since the fuel properties are typically very similar.

At the time of writing, there are eight production pathways certified for blending with conventional aviation fuel as specified in ASTM D7566-23b [13]. The certified production methods are continuously expanded to accommodate other pathways, but the requirements imposed on all the fuels are identical. The standard mainly assess physical and chemical properties of the fuel, but not emission or combustion stability of the fuels. Impact of using SAF synthesized towards material and elastomer compatibility, blow-off limits, and altitude re-ignition are some of the other fuel properties that are determine if a production pathway is certified for use. Elastomer properties are important in ensuring that the fuels have sufficient seal-swelling capacity to prevent fuel leakage, while understanding of the blow-off limits will prevent blowout in the combustion chamber when operating under lean conditions.

Other than the current eight certified production pathways, there are still other methods of synthesizing SAFs. This thesis project is part of a project that looks into one of the alternative pathways.

## 2.4. PureJet: Producing Alternative Jet Fuels through Pyrolysis Oil

There are various methods to generate renewable fuels, including those intended to be used as SAFs. Figure 2.1 provides an overview of this. Biomass can be obtained from first, second, and third generation feedstocks. First generation feedstock refer to those obtained from agricultural source, which could also be used as food source, Second generation feedstocks are those that come from lignocellulosic materials, and are mainly made-of non-edible plant materials. Third generation feedstocks are obtained from algae or seaweed [14].

As described in the previous section, the certified pathways of producing SAF are continuously being expanded. Currently, 95% of SAFs produced come from Hydrotreated Esters and Fatty Acids (HEFA) [15]. This production method is only used to convert oils or fats into SAFs, and does not process the widely available lignocellulosic feedstocks [16]. PureJet project attempts to fill this gap.

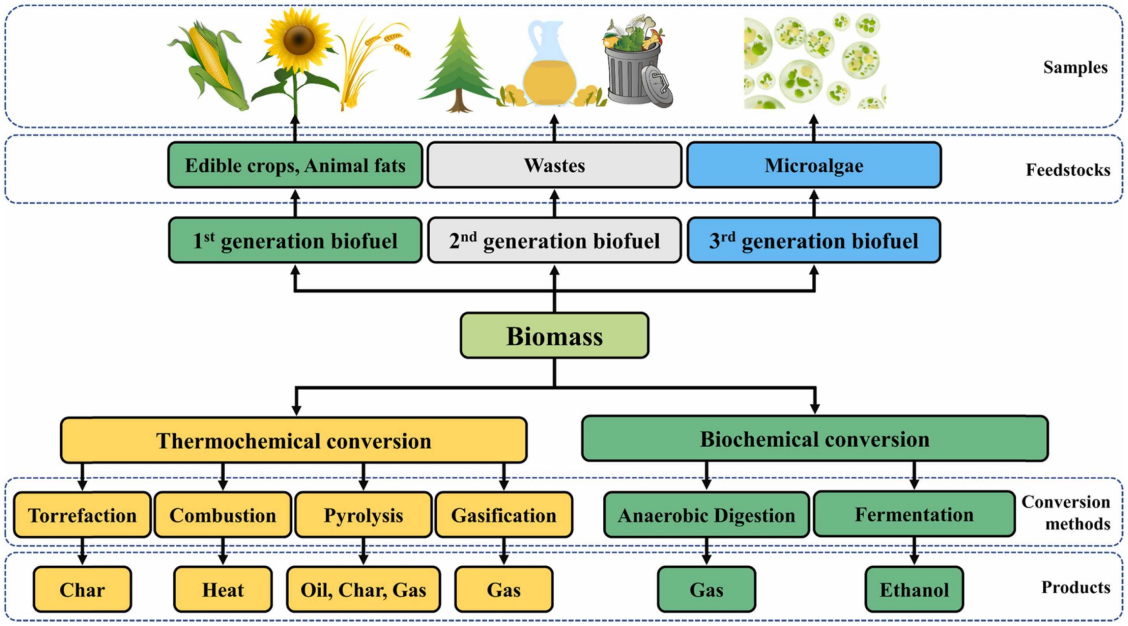


**Figure 2.1:** Biofuel generation pathways & conversion. The project looks into generating SAF through second generation biofuel, and thermochemical conversion of pyrolysis to bio-oil. This is bio-oil is then hydrotreated to generate SAF [17].

Through PureJet, second generation lignocellulosic material is converted into Fast Pyrolysis Bio-Oil (FPBO) through pyrolysis, as shown in Figure 2.2. This FPBO is then hydrotreated to produce HPO, which may be used as SAF. The project is a collaboration between BTG Biomass Technology BV, TU Delft, and SkyNRG. BTG is responsible for the general research & production of the biofuels, while TU Delft will perform research into the combustion properties of the biofuels. SkyNRG performs advisory role.

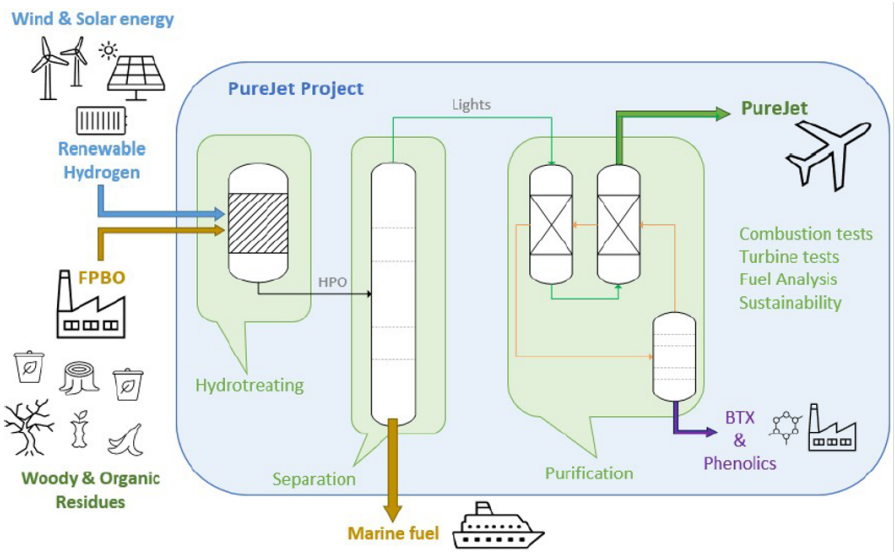


**Figure 2.2:** Purejet production outline.

### 2.4.1. Thesis Framework

As previously mentioned, biofuels used as SAF has to fulfill certain physical, chemical, and combustion properties. Knowledge of emission generated by SAF would provide valuable information on the change of GHG contribution, while knowledge of combustion properties would also provide information to ensure stability of combustion. The flame and emission characteristics of Jet-A1 are already relatively well established. However, combustion characteristics of biofuel is still pretty limited, especially considering differences that may be caused by the wide range of available production pathways.

This report will thus look into characterizing the HPO produced in the PureJet project in terms of its flame speed and emission through experiment in a laminar bunsen setup. A recommendation on modifications to be made to existing swirl-stabilized burner setup in the lab for use in a premixed prevaporized configuration is also made in the last chapter.

# 3

# Literature Survey

This chapter will introduce relevant literature of the thesis.Different commonly used combustor design is introduced in section 3.1, and the relevant SAF certification requirements are described in section 3.2. An overview of studies on emission of SAF is provided on section 3.3, and the NO generation pathways are explained in section 3.4, while the relevant combustion diagnostics methods are provided in section 3.5. Blowoff and flashback are two subjects of importance in combustion, and an overview of studies that have been performed on SAFs are provided in section 3.6. Subsequently, literature review of the relevant swirl generation and fuel injection in the combustion lab are provided in section 3.7 and section 3.8, respectively. Finally, the estimation of thermal emissivity used in heat loss calculation is described in section 3.9.

## 3.1. Combustor Designs

Combustor in an aero-engines convert chemical energy of the fuel to thermal energy, which can then be converted into kinetic energy by the turbines. This energy conversion can be achieved through various injector/combustor designs. Three of the most common architecture used and studied are the lean direct injection (LDI), Rich - Quick mix - Lean (RQL), and Lean premixed/prevaporized (LPP) systems. All of these architectures aim to lower $NO_x$ emission by burning at the lean condition, which would lower temperature, thereby decreasing thermal $NO_x$ generation. This topic would be explored in more detail in section 3.3.

Regardless of the combustor architecture, they have to be compatible with the fuel used to ensure combustion stability, as well as pollutant and noise emission. Combustion stability is split into static and dynamic stability. Static stability refers to the capacity to maintain continuous combustion without blowout. This covers stability of the flame, flashback, and blow-off of the flame. Blow-off and blowout are typically coupled, and reignition comes into focus when blowout occurs. To maintain the power generated by an aero-engine, it thus becomes important to understand blowout mechanism, and the blow-off limits. This has been an extensive topic studied for the three different combustor design for kerosene and gaseous fuels. However, studies that look into the change in stability caused by the use of SAF is relatively more limited.

Flame stability can be induced with various flame anchoring mechanisms. This includes pilot stabilized flame, or more commonly studied bluff-body and swirl stabilized systems. This master thesis project will be conducted in a swirl stabilized combustion system, with modifications to available setup in the lab. The next several subsections would look into the various combustor architectures that are commonly used today.

### 3.1.1. Lean Direct Injection (LDI)

LDI architecture directly injects (liquid) fuel into the combustor at lean conditions. Since $NO_x$ emission is a function of local temperature, the local equivalance ratio has to similarly avoid stoichiometric equivalence ratio. This requires effective fuel atomization, vaporization, and mixing [18]. In other words, the

design of the injector and combustor should try to quickly create a homogeneous fuel-air mixture after fuel injection. This is typically achieved by using multiple fuel injectors and fuel-air swirlers to create multiple recirculation zone [18], as shown in Figure 3.1. An example of an engine utilizing LDI is the Trent XWB, which uses 20 fuel nozzles [19]. The main disadvantage of the system is the size of the combustor.

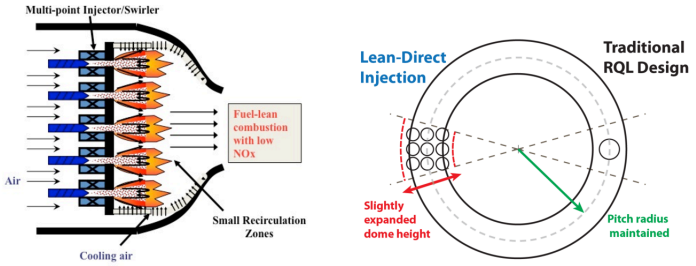


**Figure 3.1:** Lean Direct Injection Combustor, adapted from Derick S. Endicott [20]

### 3.1.2. Rich - Quick mix - Lean (RQL)

RQL combustors is another combustor architecture which is commonly used. In RQL combustors, air is first mixed in the primary (Rich zone) zone, under rich conditions. It is in this region that fuel is atomized and injected. In the secondary zone (quick mix), additional air is introduced and mixed. Finally, combustion is continued in the tertiary (lean) zone under lean condition [21] [22]. This is illustrated in Figure 3.2

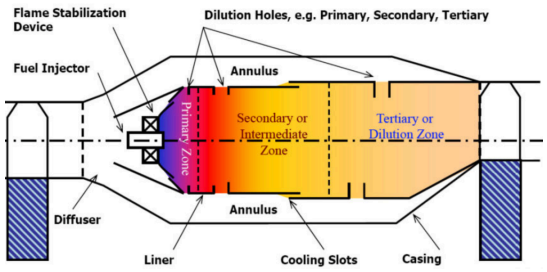


**Figure 3.2:** Example of RQL combustor [20]

A disadvantage of RQL combustor is that combustion occurs in the diffusion regime in the rich zone, but it also offers the benefits of better dynamic stability [18]. An example of a RQL combustor is the Talon-X combustor used in PW1000 Geared Turbo-Fan (GTF).

### 3.1.3. Lean premixed/prevaporized (LPP)

LPP completely prevaporizes fuel and mixes it with air before combustion at lean condition. This minimizes should, in theory, produces homogeneous mixture, and minimizes pockets of stochiometric equivalence ratio mixture. In this way, hot spots are minimized, and $NO_x$ emission should be the lowest compared to the other combustor design.

## 3.2. Drop-in Requirements

Drop in requirements is an important condition for SAFs. It ensures that the SAFs could be readily used as substitutes for Jet-A1 without modifying aircraft engines. These requirements are defined in different standards, ATSM D4054, ATSM D7566, and ATSM D1655, which are used internationally. The three standards are linked in the certification process, and can be split into certification for production process and certification for fuel batch. ATSM D4054 and ATSM D7566 certifies production method, while ATSM D7566 and ATSM D1655 certifies produced fuels as SAFs. The three standards are described in more detail in the following paragraphs.

ATSM D7566 serves as batch certification of synthesized hydrocarbons, which production method has

been certified through ATSM D4504. At the time of writing, there are eight certified methods for synthesizing SAFs. The standard provides limits on several chemical and physical properties of these synthesized fuels, which includes among others its distillation temperature, flash point, density, freezing point, and thermal stability. Fuels produced through these methods are then blended with conventionally produced Jet-A1, with a maximum blending ratio depending on the production method.

The conventionally produced jet fuel-used for blending has to be certified as Jet-A or Jet-A1 through ATSM D1655. This is also achieved through limits imposed on the chemical properties similar to the ones used to certify synthesized hydrocarbons in ATSM D7566, but also include limitations on corrosive property of the fuel, heat of combustion, and smoke point. Synthesized hydrocarbons which has been blended with certified Jet A/A-1 has to be then re-certified with the same requirements used for Jet A/A-1 as outlined in D1655. The simplified batch certification process is illustrated in Figure 3.3.

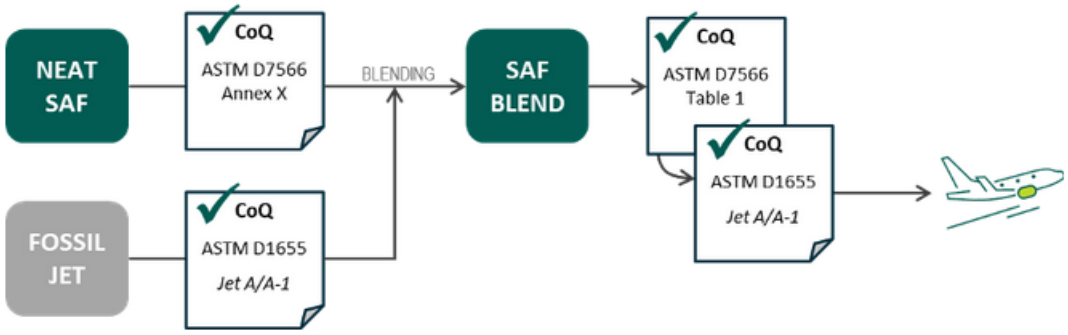


**Figure 3.3:** SAFs drop-in certification process

ATSM D4054 certifies the production method of synthesized hydrocarbons for use as SAFs. The process is split into four tiers, as shown in Figure 3.4. Tier 1 requires a sample fuel from the production method to fulfill the general chemical and physical properties as specified in ATSM D7566. Tier 2 would then tests the fuel for more detailed chemical, properties, and electrical properties, with respect to safety, ground handling, and materials compatibility. Tier 3 looks into fuel seal-swelling capacity, compatibility with coatings, metals, additives, and various components in aircraft fuel systems. Combustion test also has to be performed in this step to characterize fuel combustion performance, in the form of LBO, cold start, altitude re-ignition, and emission among others. Finally, tier 4 tests look into influence of the fuel on aircraft performance, endurance, and operability through flight tests. This thesis will help to answer some of the Tier 3 requirements, by looking into the lean blowout and flashback of a set of potential hydrotreated pyrolysis oil. This would provide preliminary information on whether it is feasible for the oils to be used as SAFs.

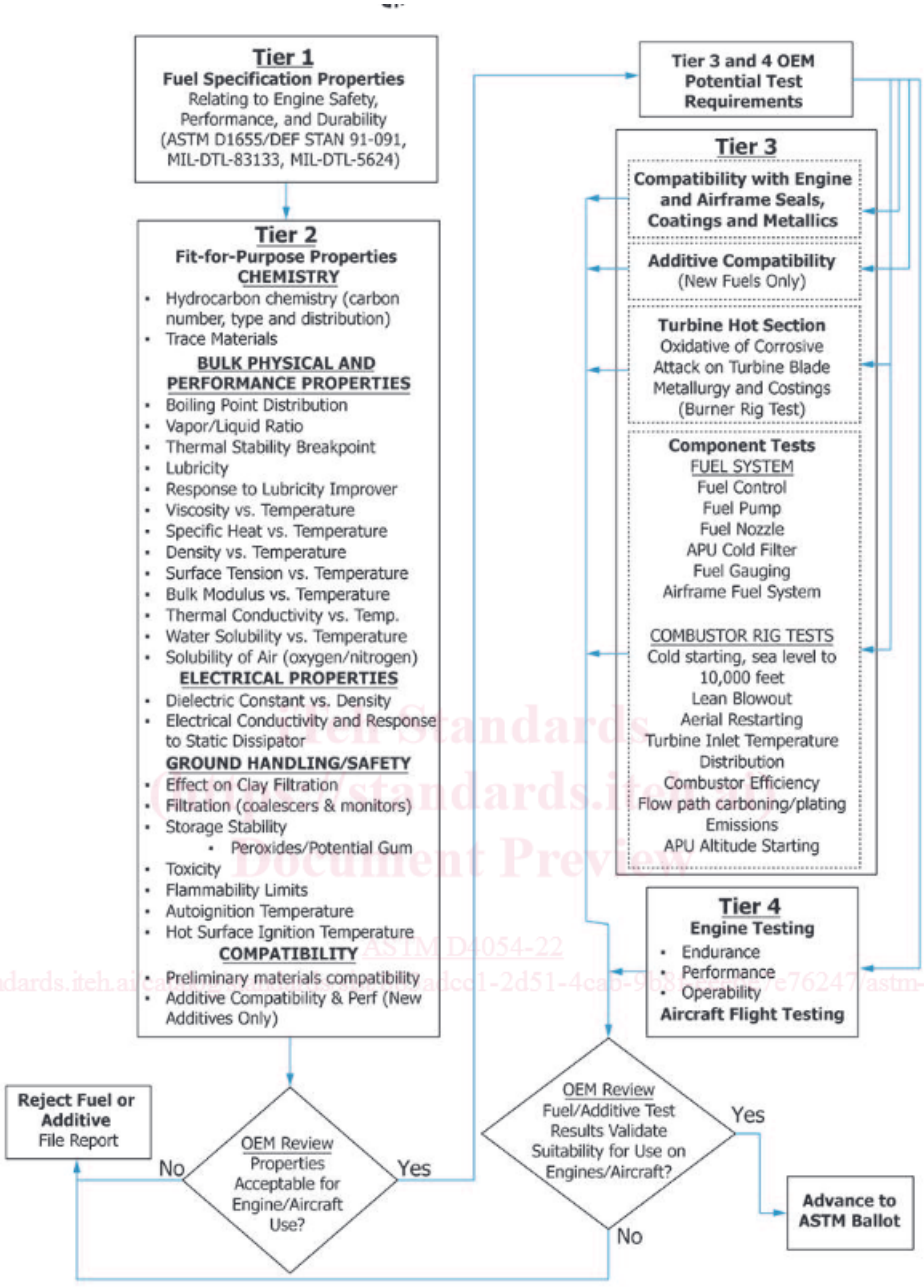


**Figure 3.4:** ASTM D4054 procedure for evaluation of new SAFs and fuel additives [23]

## 3.3. SAF emission

Emission differences of SAF from conventional jet fuels has been a topic of significant interest in research. However, most of these research were performed in a practical gas turbine combustor, which limits the observation the flame dynamics. Most papers that compare SAF noted minimal change in gaseous emission products, including $NO_x$ and CO. Lower PM 2.5 emission were, however, found on SAF. This is often attributed to the lower aromatics content of SAF. This was found in studies conducted by Liu et al. [24], which compares RP-3 with hydrothermal condensation hydrotreated jet biofuel (HCHJ) obtained from cellulosic biomass. A similar result was also observed in the study of Khandewal et al. [25] [26] comparing Fischer-Tropsch (FT) biofuel with Jet-A1 and JP-8.

On the other hand, Corporan et al. [27] and Timko et al. [28], noted lower PM emission attributed to the lower aromatics compound, but saw a slight decrease in $NO_x$ emission from a FT derived SAF. Contrary

to these findings, a separate study by Corporan et al. [29]with a blend of JP-8 with hydroprocessed renewable jet (HRJ) and FT fuel saw a decrease in CO emission, but not $NO_x$ emission. Riebl et al. [30] saw an increase in NOx emission for FT SAF.

However, a separate study by Lobo et al. [31], performed in an Auxiliary Power Unit (APU) noted a $5-10\%$ reduction in CO emission and a $5\%$ reduction in $NO_x$ emission relative to Jet-A1. An overview of the emission measured compared to jet fuels from the different papers are also presented in Table 3.1. Differences in emission measured was also seen in previous research on pyrolysis oil. However, since this production method has not been certified and standardized, the wide variation in the quality and treatment of the tested pyrolysis oil makes a comparison less reliable, and is not presented in this review. It can be said, however, large differences was seen in the emission measured from the different pyrolysis fuels, as expected from the wide variation of quality and treatment process.

**Table 3.1:** Overview of emission of FT fuels compared to conventional jet fuels measured in different studies

| Emission | Slightly Higher | Similar | Slightly Lower |
|---|---|---|---|
| Nox | Riebl et al. [30], Lobo et al. [31] | Liu et al. [24], Khandewal et al. [25], [26] | Corporan et al. [27], Timko et al. [28] |
| CO | Lobo et al. [31] | Liu et al., [24] Khandewal et al. [25][26] | Corporan et al. [29] |

## 3.4. NO generation Pathways

NO can be generated through four primary routes, Figure 3.5. Thermal route, Equation 3.1 to Equation 3.3, is dominant at high temperature, above 1800K. At moderate temperature and high pressure, $N_2O$ route is dominant through Equation 3.4 to Equation 3.6. The third NO generation pathway is through the prompt route. Prompt NO is significant under fuel rich condition, where $N_2$ react with hydrocarbon radicals, forming NCN, HCN, and HNCN which react to form NO, Equation 3.7 to Equation 3.10. The fourth possible pathway for NO formation is through the NNh route, Equation 3.11 & Equation 3.12. This route is favoured at lower temperature [32].

$$N_2 + O \leftrightarrow NO + N \tag{3.1}$$
$$N + O_2 \leftrightarrow NO + O \tag{3.2}$$
$$N + OH \leftrightarrow NO + H \tag{3.3}$$

$$N_2 + O(+M) \leftrightarrow N_2O(+M) \tag{3.4}$$
$$N_2O + O \leftrightarrow NO + NO \tag{3.5}$$
$$N_2O + H \leftrightarrow NO + NH \tag{3.6}$$

$$CH + N_2 \leftrightarrow NCN + H \tag{3.7}$$
$$NCN + O \leftrightarrow CN + NO \tag{3.8}$$
$$NCN + H \leftrightarrow HCN + N \tag{3.9}$$
$$NCN + OH \leftrightarrow HCN + NO \tag{3.10}$$

$$N_2 + H(+M) \leftrightarrow NNH(+M) \tag{3.11}$$
$$NNH + O \leftrightarrow NO + NH \tag{3.12}$$

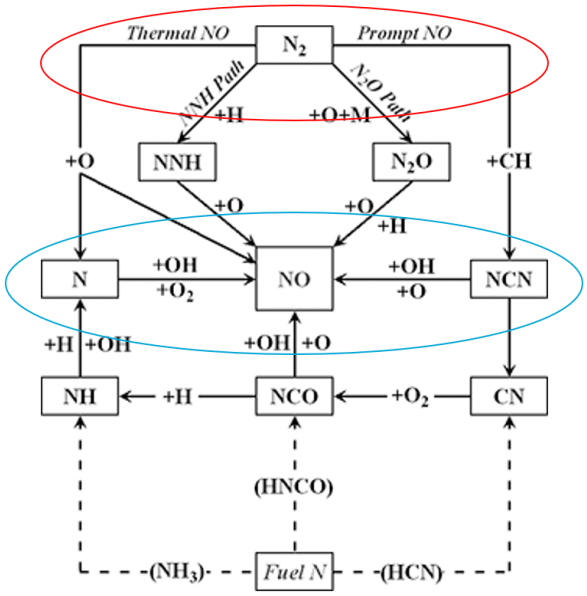


**Figure 3.5:** NO generation pathways [32]

## 3.5. Diagnostic techniques in combustion experiments

Flame-front analysis has been a topic that is widely explored in research. It provides insight into the combustion process and may allow optimization to increase combustion efficiency. This is typically achieved by natural Chemiluminescence or Planar Laser Induced Fluorescence to measure species concentration, and Particle Image Velocimetry (PIV) to measure velocity field. Of relevance to this thesis is the potential use of these systems in determining flame speed of the different fuel samples. The next few subsections would describe these systems.

### 3.5.1. Flame Speed

Flame speed refers to the velocity of the flame front with respect to the velocity of the flow (unburned gas mixture), Equation 3.13. $s_d$ refers to local flame displacement speed and n is the normal vector of the flame front, while **w** and **v** refer to flame front velocity and flow velocity, respectively. Burning velocity, defined as $s_d \cdot \mathbf{n}$ is also a method of quantification that is often observed in literature. Flame speed is important because together with flow speed, it affects the position of the flame front. This means it is related to flame blowout, flashback, and stabilization [18]. In Figure 3.8, flow speed equals flame speed, and flame front velocity is zero in both cases. In the case of laminar flame, the flame front position is also constant in time.

$$s_d \cdot \mathbf{n} = \mathbf{w} - \mathbf{v} \tag{3.13}$$

### 3.5.2. OH Chemiluminescence

Chemiluminescence is usually the simplest non-intrusive diagnostic technique used in combustion experiment. An example of a chemiluminescence measurement setup is shown in Figure 3.6. Typically an ICCD camera with UV lens and a narrow-band-pass filter is used to capture the images. The wavelength of this filter depends on the species that the camera is intended to capture. For OH Chemiluminescence, this wavelength is 308 nm [33].

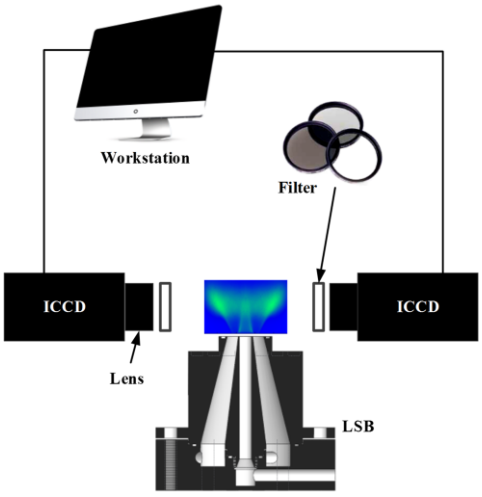


**Figure 3.6:** Example of chemiluminescence measurement system [33]

The captured images also has to be further processed before being analyzed. First, a set of captured images is averaged to reduce noise. Background emission is then subtracted from the averaged images, symmetrized, and smoothed by an average filter. Finally, inverse Abel transformation to transform the image into a radial distribution image [33]. An example of the result of the aforementioned processes is shown in Figure 3.7.

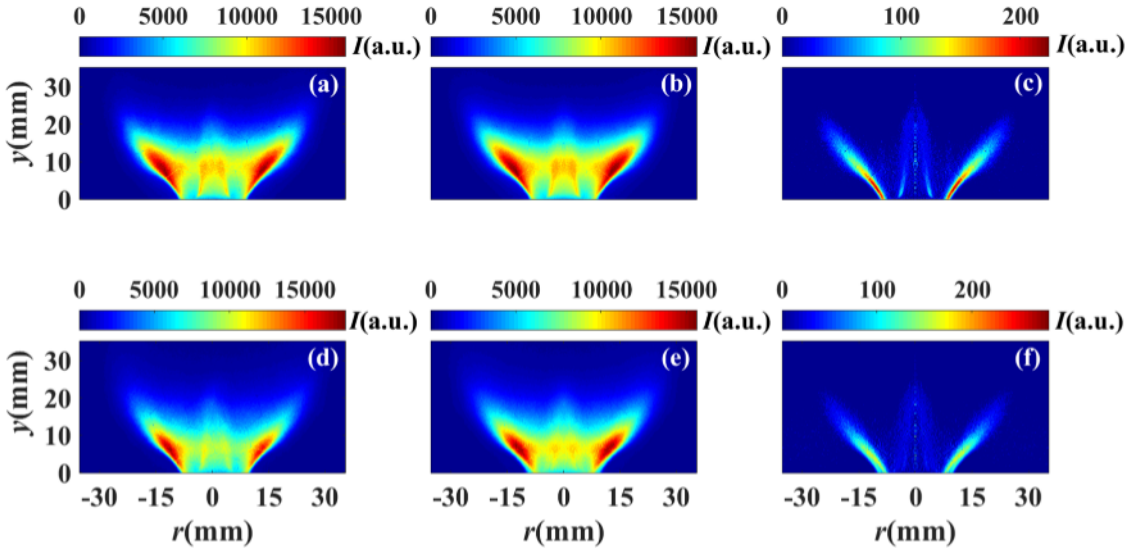


**Figure 3.7:** Example of chemiluminescence processing result for low swirl flames. (a) Averaging process of OH, (b) symmetrizing , (c) Inverse Abel transformation result. d to e are similar processes performed for CH images

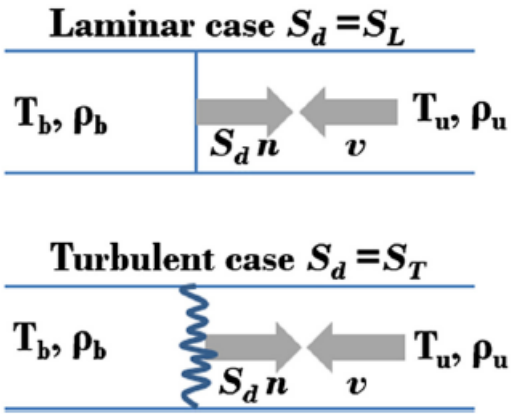


**Figure 3.8:** Balance of flame speed and flow speed. Top schematic shows flow speed balance with laminar flame speed, and bottom schematic illustrates a similar balance with turbulent flame speed. [18]

### 3.5.3. Area method through OH-PLIF/Chemiluminescence

Turbulent flame speed can be accounted in various forms in experiments. For systems utilizing only PLIF, the three commonly used approach to define burning velocity are the global consumption speed $(S_{T,GC})$, local consumption speed $(S_{T,LC})$, and local displacement speed $(S_{T,LD})$ [34]. Global or area-averaged displacement speed $(S_{T,GD})$ is another approach. It was also observed that there are some variation in the way these flame speeds are defined.

Wang et al. defines $(S_{T,GC})$ as Equation 3.14 and $S_{T,GD}$ as Equation 3.15. $\dot{m}_{ih}$ is the mass flow rate, $\rho_u$ is the unburned mixture density, $\bar{A}_f$ is the characteristic area of the mean flame front, and $s_{LD}$ is the local displacement speed. He reasoned that the two flame speed would be equal in the preheat zone since $\rho_u = \rho$. $S_{T,GD}$ can therefore be determined through Equation 3.14 by defining $\bar{A}_f$ at the beginning of the preheat zone, where progress variable $(c)$ is 0.1. The flame brush used to identify location of $c = 0.1$ is first identified by overlapping multiple flame front boundaries as obtained from OH-PLIF images, Figure 3.9. This approach is also used in the papers of Zhang et al. [35], Griebel et al(a). [36], Daniele S. [37][38]. A similar approach by Griebel et al(b). [39] defines the flame front as the location of the most common flame front position over 800 images. A different equation, Equation 3.16 could also be used to quantify the speed through the conical angle formed by the flame[40].

$$S_{T,GC} = \dot{m}_{ih} / \left(\rho_u \bar{A}_f\right), \tag{3.14}$$

$$S_{T,GD} = \int s_{LD} dA / \bar{A}_f, \tag{3.15}$$

$$S_T = U sin(\theta/2) \tag{3.16}$$

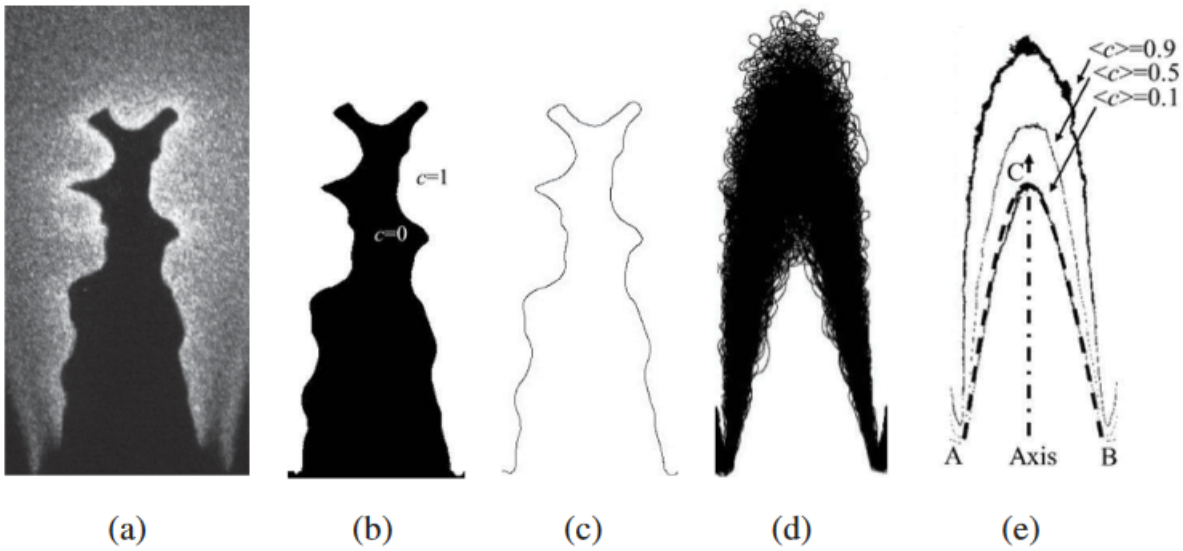


**Figure 3.9:** Averaging procedure for obtaining progress variable contour, $(c)$ and turbulent flame speed. (a) shows a single OH-PLIF shot; (b) binarized image; (c) flame front; (d) flame brush from 500 flame front images; (e) Interpolated progress variable contours. [35]

Similarly, laminar burning velocity, $S_l$ of a bunsen stabilized flame, Figure 3.10, can be obtained through cone angle method, Equation 3.17, or area method in Equation 3.18 [41]. $U_0$ is the average flow velocity, $\alpha$ is the angle of the flame front obtained through Chemiluminescence, $\dot{Q}$ is the volumetric flow rate, and $A_f$ is surface area of the flame.

$$S_l = U_0 sin\alpha \tag{3.17}$$

$$S_l = \dot{Q}/A_f \tag{3.18}$$

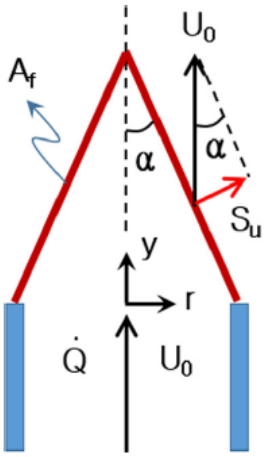


**Figure 3.10:** Illustration of a bunsen stabilized flame [41]

### 3.5.4. Combined OH-PLIF and PIV systems

A different flame speed measurement technique using combined PLIF and PIV systems are also commonly found in literature. This technique should, in theory, be more accurate since there is no concern about determining the correct flame-front based on averaging. An example of the setup is shown in

Figure 3.11. The two systems work in tandem, where PLIF captures the flame fronts at two time instance $t_1$ and $t_2$. The displacement of the flame front divided by the time interval when the two images are taken provide the flame front velocity **w** in Equation 3.13.

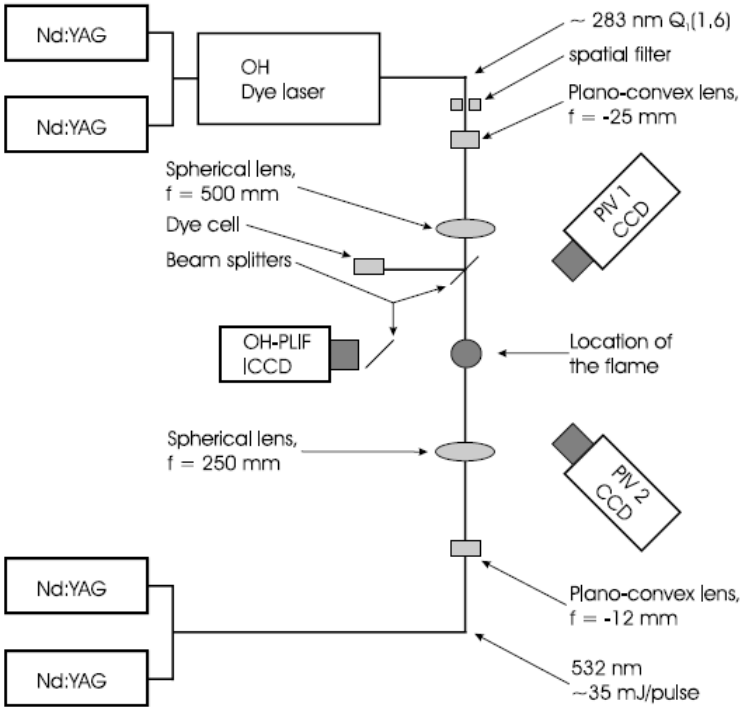


**Figure 3.11:** Simultaneous PLIF and PIV systems for flame speed determination [37]

Meanwhile, PIV captures the flow velocity at time instance $t_1$, through a similar method. Two laser pulses would be fired at a much shorter time interval $t_1$ and $t_1 + \Delta t$ to capture the displacement of seeder particles. The displacement of the seeder particles divided by the time interval provides the flow velocity **v** in Equation 3.13. The difference of the two velocities provides the burning velocity $s_d \cdot \mathbf{n}$. This is illustrated in Figure 3.12, where in the picture $u_t$ is burning velocity, $V_G$ represents the local flow velocity.

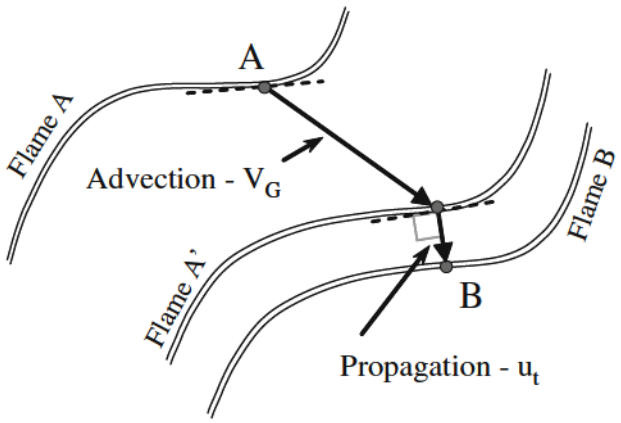


**Figure 3.12:** Calculation of flame speed through determination of flame front displacement and flow velocity, $u_t$ is burning velocity, $V_G$ represents the local flow velocity. [34]

The two systems would be synchronized and triggered at different times, as shown in Figure 3.13. As previously described, the PLIF system would trigger twice at time instance $t_1$ and $t_2$, and the PIV system

would also trigger twice, but a much shorter time interval around $t_1$. Based on observed literature, the typical time interval used in this simultaneous PLIF - PIV system would be tens of micro-seconds for the PIV systems, and hundreds of micro-seconds for the PIV system.

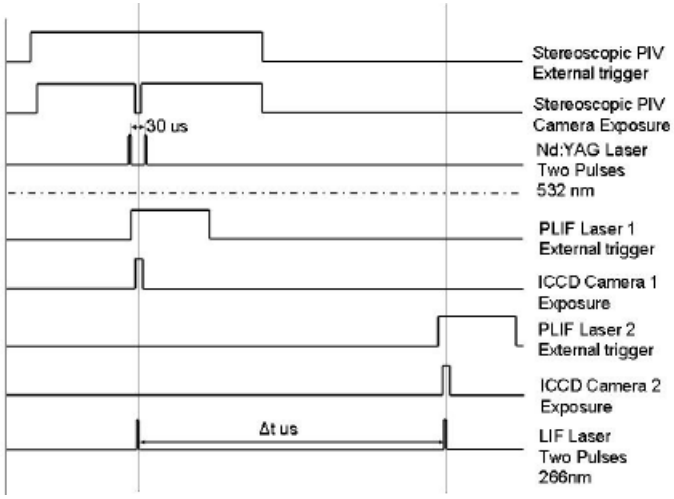


**Figure 3.13:** Timing diagram for simultaneous PLIF and PIV system [42]

### 3.5.5. Turbulent flame speed measurement through flowfield

The aforementioned methods have not been used in practice for swirl stabilized combustion, to the best of the author's knowledge. Literature on turbulent flame speed measurement for swirl stabilized combustion is scare. Some flame speed measurement had been performed on low swirl combustors, although the low swirl number of these combustors do not result in vortex breakdown.

For low swirl flames, measurements are typically estimated by assuming turbulent flame speed to be equal to velocity field at the flame front. Beerer et al. [43] measures turbulent flame speed of hydrogen/methane flame through the use of laser doppler velocimetry (LDV). Similarly, Plessing et al. [44] estimates the turbulent flame speed through the velocity field at the flame front obtained from PIV. The flame front is established based on OH-PLIF images and Rayleigh temperature images. Marshall et al. [45] performed similar measurements for high hydrogen fuels through PIV.

## 3.6. Blowoff and Flashback

Lean blow-off (LBO) and flashback are two aspects that receive significant interest in research on LPP combustion. Lean burning is the process of achieving combustion below the stoichiometric equivalence ratio. It has been established that burning at lean condition would lower emission, especially NOx [10]. The weaker combustion process under lean mixture, however, makes it more vulnerable to small pertubations, which may lead to extinction [46].

The blow-off limits of Jet-A1 for different combustors are relatively well understood. However, the introduction of alternative fuels necessitates that the influence of these fuels on LBO to be investigated. This is part of the requirements for certifying a synthesizing method as outlined in ASTM D4054 [23]. Since these fuel certification test requires large amount of fuel, several papers have looked into identifying general fuel chemical and physical properties that are linked to LBO.

For spray combustion, it is understood that blow-off is greatly influenced by physical and chemical properties of the fuel [47]. Lefebre [48] argues that fuel physical properties that govern atomization and evaporation quality plays a more important role under lower inlet temperature [48]. Fuels which are more difficult to vaporize tend to blow-off at leaner mixture, because it would lead to more inhomogeneous mixture, resulting in pockets of higher equivalence ratio [48]. However, by comparing LBO of n-hexane and iso-octane at two different temperatures, Grohmann et al.[47] argues that fuel chemical properties could still be important at low temperature. For n-hexane and n-dodecane, on the other hand, Grohmann et al. corroborates the findings that fuel physical properties dominates influence on

LBO at low temperature.

For a set of different fuels, Huelskamp et al .[49] demonstrated that ignition delay time could be used to represent the chemical timescale of the fuel, and correlate well with LBO. The least square fit plot was also correlated with the ratio of inlet diameter to velocity $D/U$, that governs fluid mechanics of the flow, Figure 3.14a. When the data is correlated solely with $D/U$, Figure 3.14b is obtained.

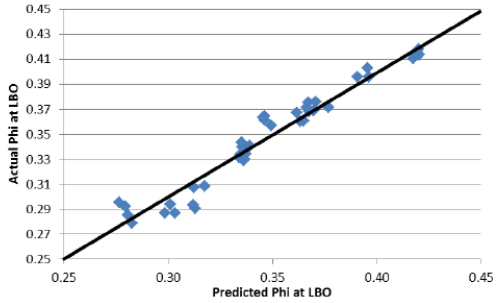


**(a)** Ignition delay and $D/U$ correlation with LBO $R^2 = 0.918$

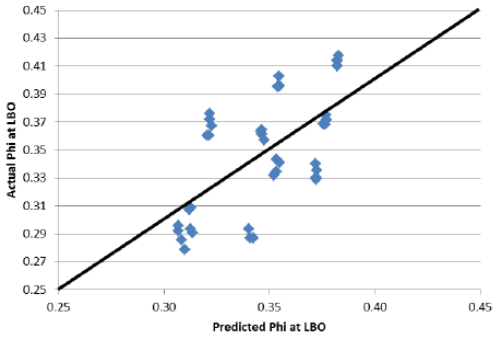


**(b)** $D/U$ correlation with LBO $R^2 = 0.381$

Hydrogen to Carbon ratio H/C also plays a role, where fuels with high H/C ratio have higher cetane number, and thereby lower ignition delay time [49]. Since derived cetane number (DCN) is correlated to ignition delay, DCN of a fuel also shows strong correlation with LBO. Fuels with higher DCN are more difficult to blow-off, especially at elevated temperature where physical properties of the fuels are not as relevant [50] [51]. On the contrary, results from other papers shows that DCN is statistically insignificant in affecting LBO [52]. The author in this paper, however, noted that the set of fuels used DCN values are not as broad as those that show a strong correlation to LBO. The mixture was also premixed, unlike the spray combustion system in the other reports.

In addition to LBO concerns, LPP combustion also has a higher propensity of flashback and risk of auto-ignition [53]. This becomes important when aero-engine operates under higher thrust setting, at elevated temperature and pressure, and higher equivalence ratio. This is because higher temperature induces higher reaction rate, leading to higher flame speed [53][54]. On the other hand, higher pressure increases mixture density, reducing mixture velocity, making flashback more likely [54].

In general, there are four mechanisms that causes flashback:

- Boundary layer induced flashback
- Turbulent flame propagation in the core
- Combustion instabilities
- Combustion induced vortex breakdown

**Boundary layer induced flashback** Boundary layer induced flashback is caused by the low flow velocities within the boundary layer close to the wall. Interaction with the wall may also lead to flame quenching from heat loss to the wall. Lewis and von Elbe observed that there is a critical value of the velocity gradient $g$ at the wall, below which flashback occurs. This critical $g$ value, $g_F$ can be expressed as Equation 3.19, which is the ratio of laminar flame speed $S_L$ to flame penetration distance $d_p$, defined as Equation 3.20. a is burner constant and $d_q$ is flame quenching distance. This flashback mechanism is dominant in low turbulence, non-swirling flows.

$$g_F = \frac{S_L}{d_p} \tag{3.19}$$

$$d_p = a d_q \tag{3.20}$$

**Turbulent flame propagation in the core** Flashback can also be triggered when velocity at the core is lower than burning velocity of the flame. The highly wrinkled and corrugated structure of swirling

flames increases the turbulent flame speed, making this mechanism more likely. Fuels with high laminar burning velocity is also more prone to this flashback mechanism, since turbulent burning velocity is directly correlated to laminar flame speed.

**Combustion instabilities leading to flashback** Fluctuating heat release in the mixture zone may lead to noise and pressure fluctuations. This may lead to periodic velocity fluctuations, leading to oscillations of the reaction zone. This again results in pressure oscillations, leading to a feedback loop and periodic flashbacks.

**Combustion Induced Vortex Breakdown** Swirling flow is one of the most common ways flame is anchored in gas turbine engines. Vortex breakdown (VBD) occurs when there is an adverse pressure gradient in the axial direction in the vortex core, and is controlled by strength of the swirl and Reynolds number [46][55]. This reduces the axial velocity at the core, allowing the flame to move upstream. This causes VBD to move further upstream, leading to a feedback loop that causes the flame to continue propagating upstream [56][55].

## 3.7. Swirl generation

Swirl has been used in combustion to anchor flames, enhance mixing, and improve emission performance [57]. The intensity of the swirl is typically defined as shown in Equation 3.21. $G_\phi$ is axial flux of tangential momentum, and $G'_x$ is the axial flux of axial momentum. R is radius of the nozzle. $G_\phi$ and $G'_x$ are defined in Equation 3.22 and Equation 3.23, respectively. U and W are the axial and tangential velocity components, respectively.

$$S_n = \frac{G_\phi}{RG'_x} \tag{3.21}$$

$$G_\phi = \int_0^R (Wr)\rho U 2\pi r dr \tag{3.22}$$

$$G_x = \int_0^R U\rho U 2\pi r dr + \int_0^R p 2\pi r dr \tag{3.23}$$

Swirl can be used to stabilize flames because at higher swirl number, $S_n > 0.6$, a re-circulation region is generated. This recirculation region mixes flue gases with fresh gases. The heat of the flue gases combined with the fresh gases, and improve combustion and blow-off performance [57] [46]. The flow patterns of swirl stabilized combustion depends on the intensity of the swirl, and are generally classified into three categories, as shown in Figure 3.15. In low swirl flame, no inner recirculation region is generated. At $S_n$ higher than 0.6, inner recirculation zone starts to generate, and combustion is stabilized near the burner. At very high swirl number, however, flame interaction with the wall is high, and is generally undesirable [57].

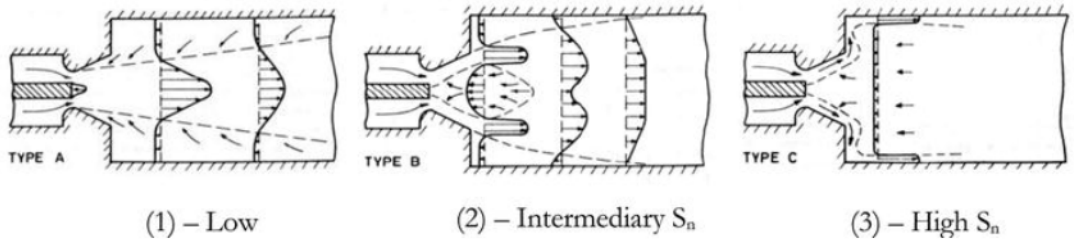


**Figure 3.15:** Effect of different swirl intensity on flow patterns [57]

Below $S_n$ of 0.5, there is no VBD, and no inner recirculation region. Stabilization mechanism occurs through the decrease in flow speed caused by the expansion of flow from the swirl. The centrifugal force from the swirl causes the flow to expand, and decrease in flow speed, as shown in the low swirl flow pattern in Figure 3.15. This decrease in local velocity is what stabilizes the flame as it allows the

flame to settle where local flow speed matches flame speed, as described in Figure 3.16. Figure 3.17 shows the decrease in axial velocity at exit of a low swirl burner (LSB). There is an immediate decrease in velocity at the exit from $U_0$ of 3.0m/s. Local velocity continues to decrease up to the point it matches flame speed, and the flame stabilizes. The increase afterwards is caused by combustion [58].

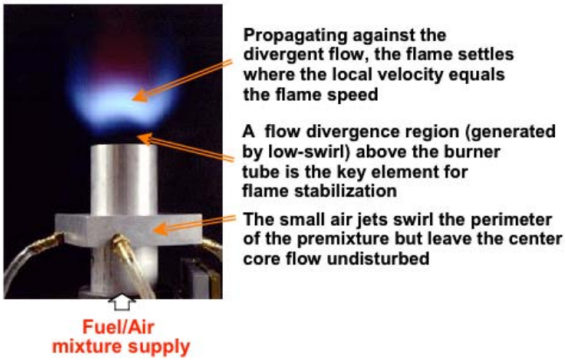


**Figure 3.16:** Low-Swirl flame stabilization with lifted bowl-shaped flame [58].

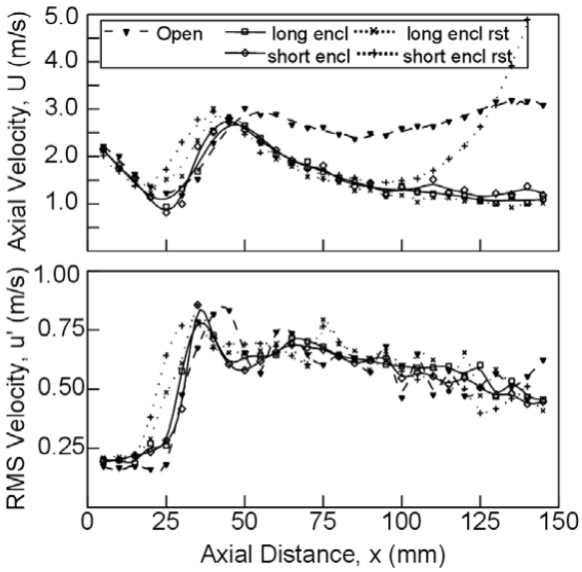


**Figure 3.17:** Axial velocity of $CH_4$ flame at burner exit for different enclosures. $U_0 = 3.0m/s$, $\phi = 0.8$, $P = 18.5kW$ [58].

In this thesis, swirl will be generated with axial vanes modified from the design of van den Bergh [59]. As shown in the book of Beer and Chigier [60], the following derivations can be made on the equations. Equation 3.22 can first be written into Equation 3.24.

Beer and Chigier [60] asserted that the pressure term in Equation 3.23 can be neglected if calculations were made based on the inlet velocity of the swirler.

$$G'_x = 2\pi \int_0^R \rho U^2 r \, \mathrm{d}r \tag{3.24}$$

For vane type swirler, angle $\alpha$ can be defined as $W/U$, Figure 3.18. Assuming the vanes are very thin with constant chord length and $\alpha$, Equation 3.22 reduces to Equation 3.25. The integration of Equation 3.24 results in Equation 3.26, and Equation 3.25 can therefore be written as Equation 3.27.

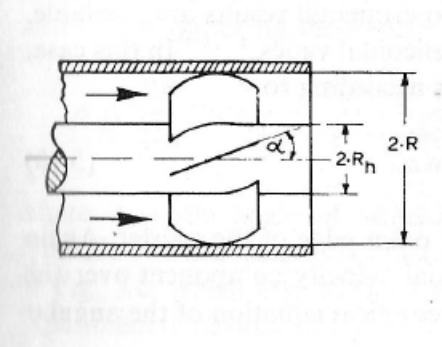


**Figure 3.18:** Schematic of Axial swirler [60]

$$G_\phi = 2\pi\rho {U_0}^2 \tan\alpha_s \frac{R^3 - {R_h}^3}{3} \tag{3.25}$$

$$G'_x = \pi\rho {U_0}^2 \left(R^2 - {R_h}^2\right) \tag{3.26}$$

$$G'_\phi = G'_x \tan\alpha_s R \frac{2}{3} \frac{1-(R_h/R)^3}{1-(R_h/R)^2} \tag{3.27}$$

However, for axial swirler with helicoidal vanes, the thin vanes and constant angle assumption is not valid. $tan\alpha_s$ therefore, has to be written as $\tan\alpha = \frac{r}{R}\tan\alpha_0$, Equation 3.28. Equation 3.27 is then written as Equation 3.29, and the swirl number$S_n$ is written as Equation 3.30. $\psi$ is the blockage factor, which can be written as Equation 3.31 [59].

$$\tan\alpha = \frac{r}{R}\tan\alpha_0 \tag{3.28}$$

$$G'_\phi = 2\pi\rho U_0^2 \tan\alpha_0 \frac{1}{1-\psi} \frac{R^4 - {R_h}^4}{4R} \tag{3.29}$$

$$S' = \frac{G}{G'_x R} = \frac{1}{1-\psi}\left(\frac{1}{2}\right)\frac{1-(R_h/R)^4}{1-(R_h/R)^2} tan\alpha_0 \tag{3.30}$$

$$\psi = \frac{n\int_{R_h}^{R_t} \frac{t}{\cos(\alpha)}\mathrm{d}r}{\left(R_t^2 - R_h^2\right)\pi} \tag{3.31}$$

Aside for swirl generation, the decay of the swirl throughout the mixing tube towards the combustion chamber has to be considered. Viscosity will result in mixing and increase flow uniformity. This would degrade swirl number in the flow because of the degradation in the radial pressure distribution. Steenbergen and Voskamp [61] reviewed a set of literature studying swirl decay in a pipe, and observed that the decay can be estimated as a function of the axial distance Equation 3.32. $\beta$ is the decay constant and D is the diameter of the pipe. The constant depends on the initial swirl number and diameter Reynolds number of the flow, Figure 3.19.The effect of swirl decay will be incorporated in the redesign of the swirler.

$$\frac{S_n}{S_{n_0}} = e^{-\beta\frac{X}{D}} \tag{3.32}$$

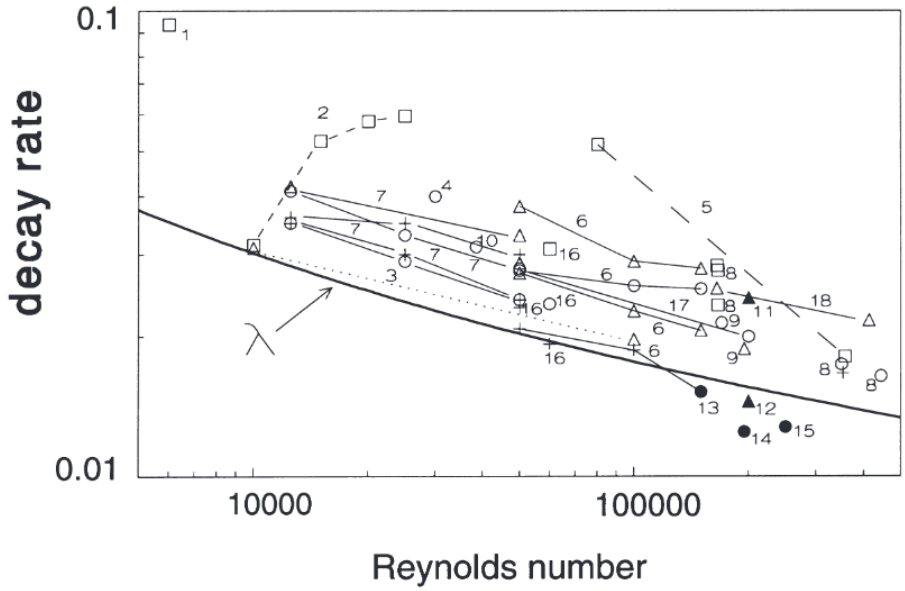


**Figure 3.19:** Swirl decay constant vs Reynolds number.
$\triangle : 0 < S_{n_0} < 0.1; + : 0.1 < S_{n_0} < 0.5; \bigcirc : 0.5 < S_{n_0} < 0.8; \square : S_{n_0} > 0.8$ [61]

In addition, fuel injection after the swirler would also result in swirl number degradation. For hydrogen flames, Vermeijlen estimated up to 15% degradation of swirl number from zero to stoichiometric fuel injection, Figure 3.20.

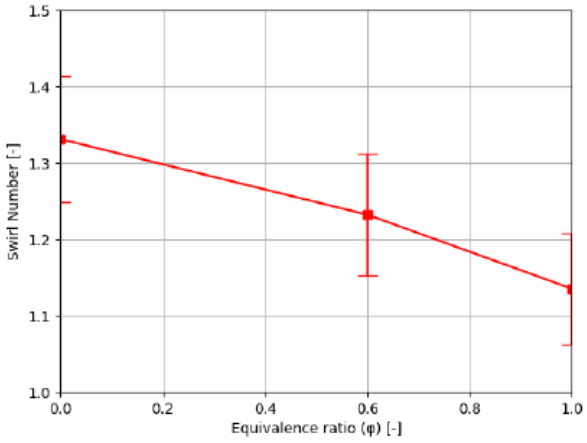


**Figure 3.20:** Swirl number degradation as function of amount of fuel injected [62]

## 3.8. Fuel Injection and Mixing

One of the ways fuel can be injected and mixed with air for the combustion process is through the jet in crossflow configuration, as in the case in the existing setup. Fuel is injected from the radial direction as air flow through the swirler and mixing chamber, as shown in Figure 7.1. In this configuration, the quality of mixing is determined by the momentum ratio of jet to crossflow, jet penetration distance, and the length of mixing chamber.

In the case of fuel being injected from the center of the nozzle, momentum ratio should be high enough to allow the jet flow to penetrate into crossflow, but not too high such that the wall of the nozzle interferes with the vortices formed. This is shown in the study of Chen et al. [63] [64] in Figure 3.21 and Figure 3.22. Z is the axial distance from the point of injection. Ns represents mixing deficiency, and can be calculated

through Equation 3.33. f refers to the fuel mass fraction and $\bar{f}$ refers to the area average fuel mass fraction at the selected plane.

$$Ns = \frac{\iint |f - \bar{f}| \mathrm{dA}}{\mathrm{A}\bar{f}} \times 100\backslash\% \tag{3.33}$$

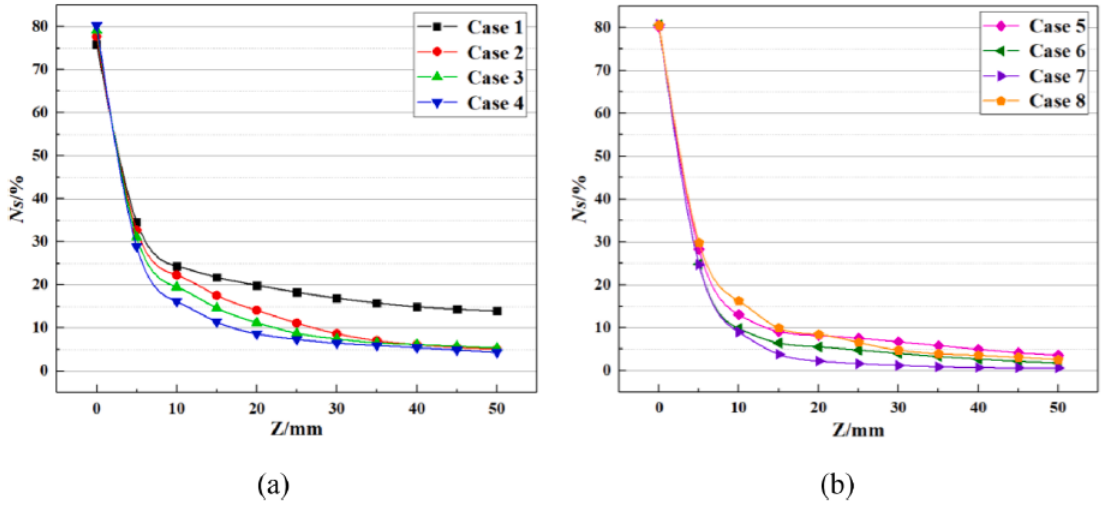


**Figure 3.21:** Mixing deficiency as a function of axial distance. Momentum ratio increases from case 1 to 8 [64]

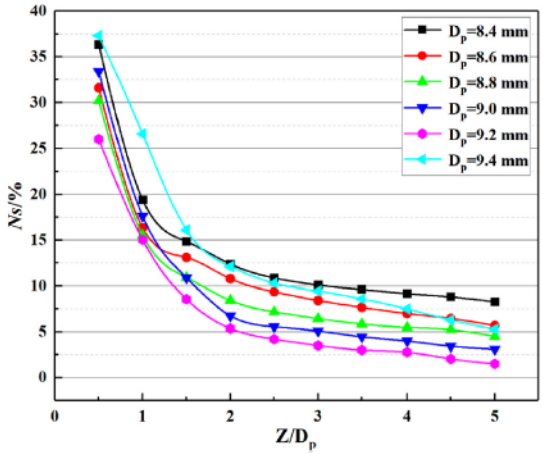


**Figure 3.22:** Mixing deficiency as a function of axial distance. $D_p$ refers to diameter of mixing crossflow channel. Higher $D_p$ results in higher momentum ratio [63].

Alternatively, it is also possible to inject the fuel through multiple streams from the edge of the tube. The higher jet penetration distance of high momentum ratio would allow the jets to collide, enhancing mixing. For different momentum ratio, mixing mechanism could differ, as shown in Figure 3.23. Higher momentum ratio will result in better mixing up to the point of over-penetration, Figure 3.24a. Far downstream of the injection location, it is observed that differences in mixing deficiency is minimal for J of 9 and above. This is because at $J = 9$ and above, the penetration depth of the jets are still high enough for the two jets to interact and enhance mixing. Penetration depth of the jets as a function of axial location can be estimated through Equation 3.34, and the maximum penetration depth is estimated through Equation 3.35 [65]. J can be calculated through Equation 3.36 [64]. The definition of $U_s$ in Figure 3.24a is shown in Equation 3.39. $\overline{C}_i$ is the average concentration at a point.

$$\frac{Y}{d_j} = 0.82 J^{0.5} \left(X/d_j\right)^{0.33} \tag{3.34}$$

$$Y_{\max} = 1.15 d_j J^{0.5} \sin\theta \tag{3.35}$$

$$J = \frac{\rho_{jet} U_{jet}^2}{\rho_{crossflow} u_{crossflow}^2} \tag{3.36}$$

**Table 3.2:** Table of momentum ratio and corresponding maximum penetration depth from Nagao et al., [65]

| Momentum flux ratio $J$ | Jet velocity $V_j$ [m/s] | Cross-flow velocity $V_m$ [m/s] | Max. penetration $Y_{max}/H$ |
|---|---|---|---|
| 4 | 20 | 10 | 0.46 |
| 9 | 20 | 6.67 | 0.69 |
| 16 | 20 | 5 | 0.92 |
| 64 | 20 | 2.5 | 1.84 |

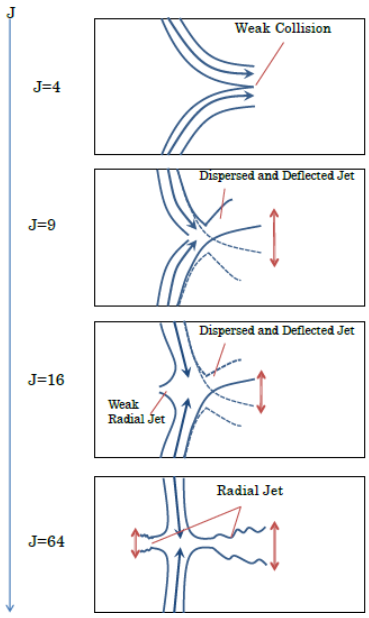


**Figure 3.23:** Mixing mechanism for different momentum ratio for two jets in crossflow [65]. Maximum penetration depth and related values as shown in Table 3.2.

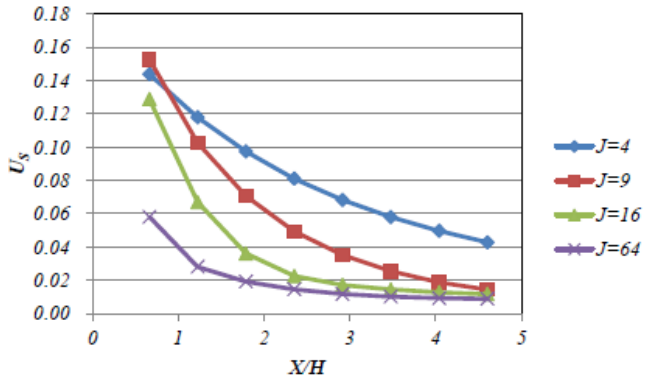


**(a)** Mixing deficiency as a function of axial distance for different momentum ratio [65]. X/H is axial distance from injection plane normalized by channel height.

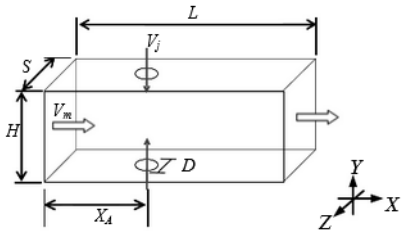


**(b)** Geometry defibition used by Nagao et al.

**Figure 3.24:** Mixing deficiency and geometry definition used by Nagao et al. [65]

$$C_{avg} = w_m/(w_j + w_m) \tag{3.37}$$

$$C_{rms} = \sqrt{\frac{1}{n}\sum_{i=1}^{n}\left(\overline{C}_i - C_{avg}\right)^2} \tag{3.38}$$

$$U_s = C_{rms}/C_{avg} \tag{3.39}$$

Kroll, et al. [66] shows that the optimum maximum jet penetration depth, as defined in Equation 3.35, is at $Y_{max} = 1.244D_p$. As shown in Figure 3.25 mixing is, however, still very effective throughout all the range simulated of $Y_{max} = 1.16D_p$ to $Y_{max} = 1.99D_p$. Standard deviation of mass fraction in the plot is defined as Equation 3.41 , where f is the mixture mass fraction defined as Equation 3.40.

$$f = \frac{T_{\text{measured}} - T_{\text{jet}}}{T_{\text{main}} - T_{\text{jet}}} \tag{3.40}$$

$$\text{STD} = \sqrt{\frac{1}{A}\sum_i a_i(f_i - \bar{f})^2} \tag{3.41}$$

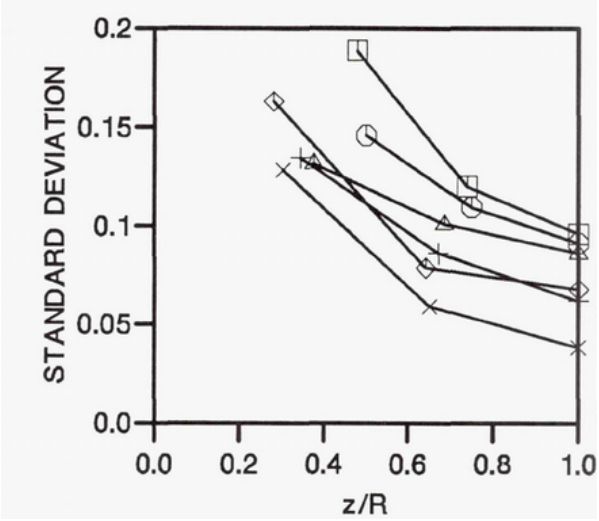


**Figure 3.25:** Mixing Deficiency defined by standard deviation of mass fractions as a function of axial distance normalized against radius. The equivalent $Y_{max}/D_p$ values are: $\square = 1.99$, $\bigcirc = 1.74$, $\triangle = 1.53$, $+ = 1.41$, $\times = 1.244$, $\Diamond = 1.16$

## 3.9. Thermal emissivity of combustion gases

Thermal emissivity of combustion gases can be estimated from the partial pressure of $CO_2$, $H_2O$ and temperature, as shown in Figure 3.26 and Figure 3.27. $P_{H_2O}\delta_{eq}$ & $P_{CO}2\delta_{eq}$ are the partial pressure of the respective gases multiplied by the equivalent length of the combustor. $\delta_{eq}$ can be calculated from Equation 3.42. Emissivity of combustion gases can then be estimated by adding the emissivity of $CO_2$ and $H_2O$. A correction factor is typically used [67], but is negligible in this case.

$$s_{eq} = 0.9\frac{V}{A} \tag{3.42}$$

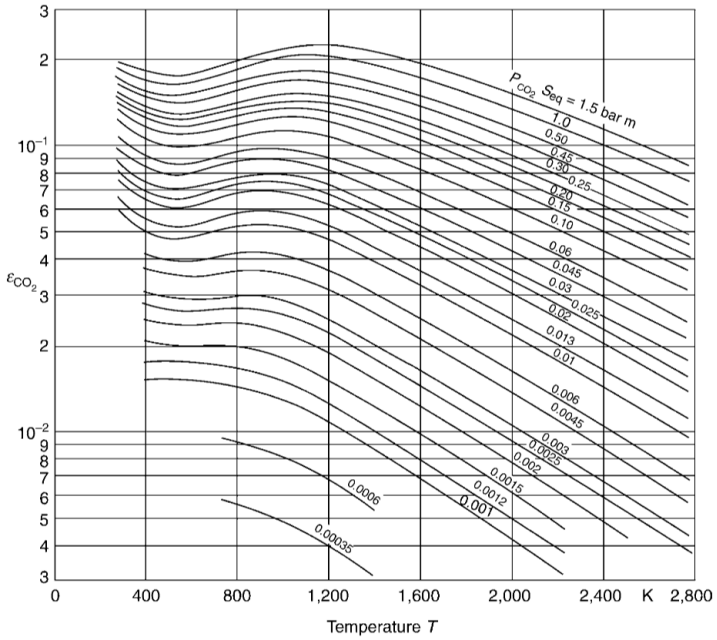


**Figure 3.26:** Emissivity of $CO_2$ as function of temperature

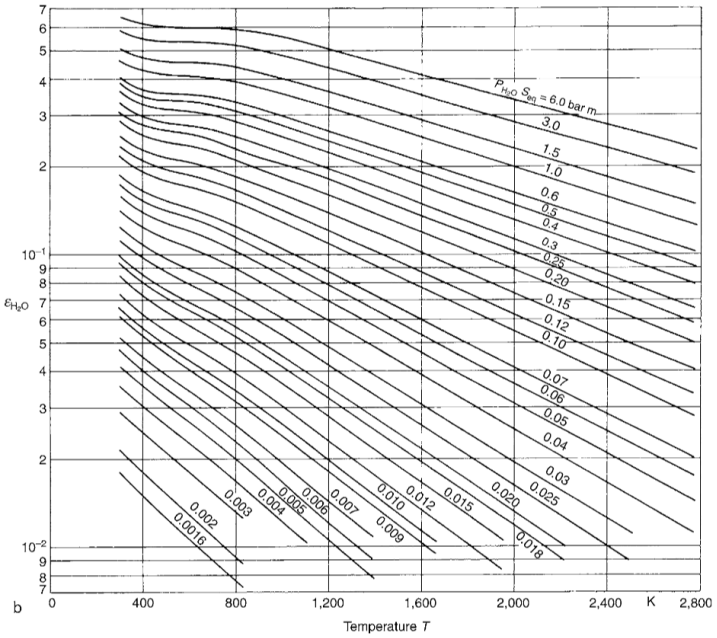


**Figure 3.27:** Emissivity of $H_2O$ as function of temperature

# 4

# Research Objective & Thesis Outline

Following the literature survey presented previously, the objective of the thesis and research questions are presented in this chapter. This is followed by the planning for the execution of the thesis.

## 4.1. Research Objective

The main objective of this thesis project is to:

*Characterize influence of hydrogen and biofuel on jet fuel blends in terms of their emission and combustion characteristics in a bunsen flame by performing OH Chemiluminescence and Exhaust Gas Analysis*

The emission performance and flame speed of jet fuel blended with hydrogen and biofuels will be evaluated through experiment. A simple modification will be made to the existing setup to allow for hydrogen injection. OH chemiluminescence will be used to determine the flame front and flame speed, while gas analyzer will be used to characterize the emission. The knowledge gained from the study will be used to propose modifications to the existing setup to accommodate swirl stabilized premixed prevaporized combustion at 11kW.

## 4.2. Research Question (s)

*What are the effect of blending hydrotreated pyrolysis oil and hydrogen with Jet-A1 in terms of flame speed and NOx and CO emission in a bunsen burner setup?*

To answer this main research question, it is then divided into further subquestions which are:

1. What are the changes in flame speed of Jet-A1 when blended with biofuels and hydrogen?
2. What are the changes in NOx and CO emission that can be observed for jet-A1 blended with biofuel and hydrogen?
3. What modifications have to be made to the existing setup to allow swirl-stabilized premixed prevaporized combustion at 11kW?

The first two research questions would be answered by performing experiments with the modified laminar bunsen burner. Flame speed would first be estimated under freely propagating flame configuration in cantera. This is used to estimate the required flow speed to maintain a stable flame for a given cone angle for the bunsen burner. OH chemiluminescence is then used to determine the flame front, and answer the first research question, while the second research question can be answered from the emission data obtained from the experiment.

Finally, the final research question is answered by estimating the required heater capacity to vaporize liquid fuels and determining the optimal fuel port diameter and penetration depth, as described in the literature survey section. A Single PSR simulation is also performed to help understand the emission results obtained.

## 4.3. Thesis Project Planning

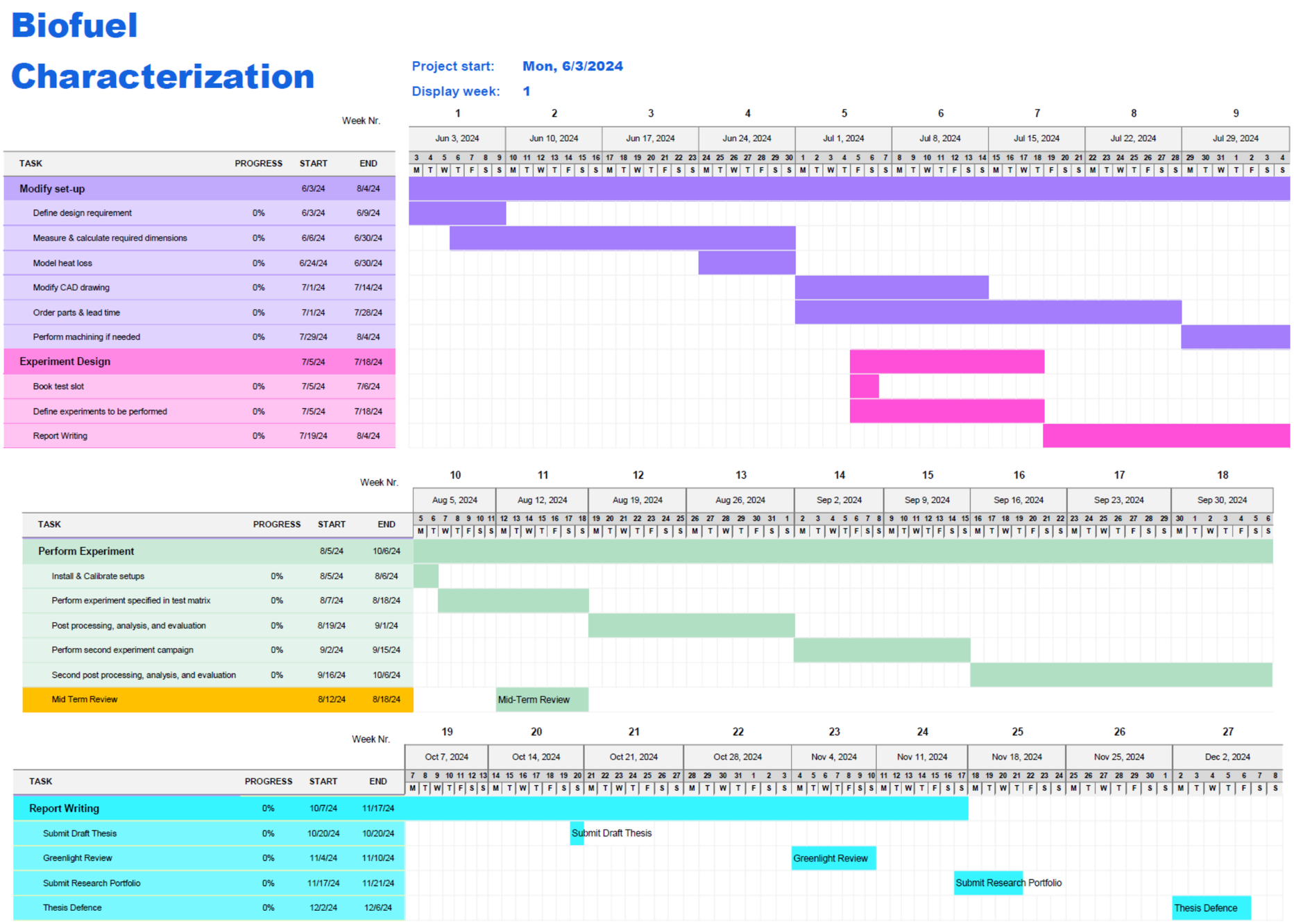


**Figure 4.1:** Gantt Chart for the project

# 5

# Methods & Tools

This chapter describes the methods used in the thesis. The setup used for the experiment is described in section 5.1, followed by the flame speed and emission analysis methods in section 5.2. Subsequently, the experiment matrix is shown in section 5.3 and single PSR simulation used to support analysis of the experiment data is described in section 5.4. Finally, heat loss model used in the simulation is described in subsection 5.4.1.

## 5.1. Bunsen Burner Setup

A simple schematic of the setup used in the experiment is shown in Figure 5.1. The length of the 10.8mm burner tube is kept at about 60 cm to ensure that the mixture is well mixed when it is combusted. A 100W AHPF-062 heater is used to preheat air before injection into the burner tube. Hydrogen and liquid jet fuel are introduced separately to the fuel line, and injected together to the burner tube. The tube is heated to 320 °C to fully vaporize the fuel with a 1kW HBQ-900 heater. The temperature of 320 °C was empirically determined to be the temperature required to maintain the mixture temperature of 250°C at the burner exit during the experiment due to heat loss.

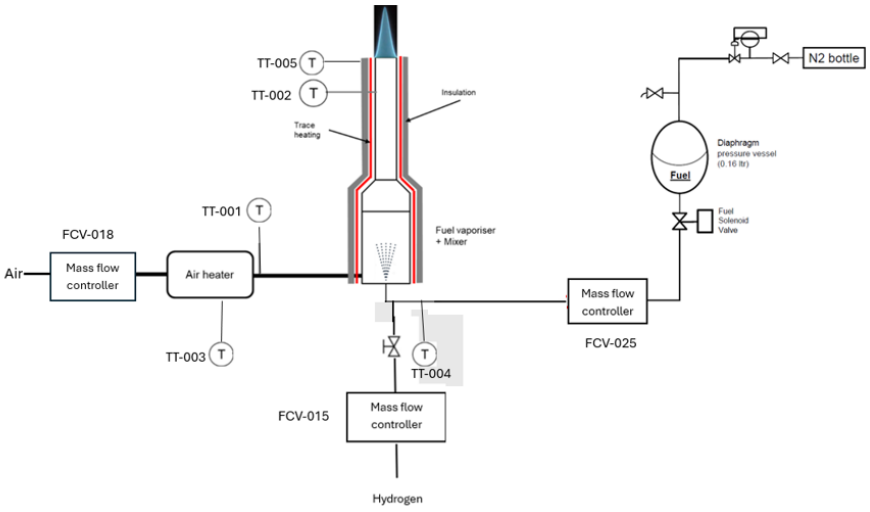


**Figure 5.1:** P&ID of the bunsen burner setup used in the experiment

## 5.2. Flame speed and Emission

Flame speed was obtained through OH chemiluminescence and area method as described in the literature section, subsection 3.5.3. OH-PLIF and PIV were not used because of the complexity of the system and time limitation. The raw image was first normalized to adjust for the lower burning intensity and therefore brightness at the tip. Otsu edge detection was then used to separate the flame region from the environment, and edges were detected through Canny edge detection.

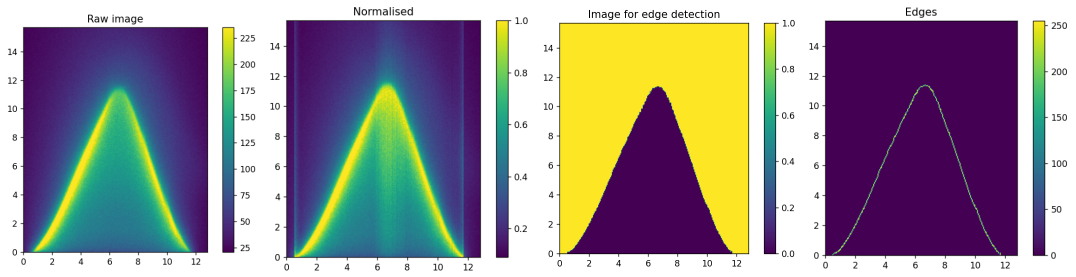


**Figure 5.2:** Edge detection of OH Chemiluminescence Images.

Emission data was collected through an ABB gas analyzer at the exit of the combustion chamber. The measured concentration was corrected for 15% $O_2$, Equation 5.1 [68]. The emissions of hydrogen blends were further normalized to account for the large difference in LHV of the fuel blend, as shown in Equation 5.2 and Equation 5.3 [69]. The emission index assumes all fuel carbon is converted into CO and $CO_2$, and may be less accurate in rich condition since combustion is incomplete and other carbon species are not negligible.

$$X_{corrected} = X_{measured} \times \frac{20.9 - \mathrm{O}_2 reference\%}{20.9 - \mathrm{O}_2 measured\%} \tag{5.1}$$

$$EI_{mass} = \left(\frac{x_i}{x_{\mathrm{Co}} + x_{\mathrm{CO}_2}}\right)\left(\frac{xMW_i}{MW_F}\right) \tag{5.2}$$

$$EI_{LHV} = \frac{EI_{mass}}{LHV} \tag{5.3}$$

## 5.3. Experiment Matrix

The experiment was performed with equivalence ratio of 0.7 up to 1.3, depending on the stability of the flame. Four different fuel samples were tested, with three jet fuel blends of HPO & Jet-A1 at $0\%$, $10\%$, and $20\%$, along with a hydrogen & Jet-A1 mixture of $90\%$ by volume.

Flame speed was estimated with cantera in a freely propagating flame setting with Hychem model [70][71]. A stable cone angle of $20^\circ$ was initially assumed, and used for calculation of the experiment matrix. The angle was later adjusted as needed during the experiment to obtain a stable flame. Bulk velocity of the mixture can then be estimated through the cone angle method, Equation 3.17. The required volumetric flow rate can be obtained from the flow speed, which allows for the calculation of air and fuel flow rate required based on the equivalence ratio and stoichiometric air to fuel ratio (AFR). Since the exact fuel composition of the jet fuel samples is unknown, they are assumed to be $C_{11}H_{22}$ in all three cases. This is based on the average composition typically found in Jet-A1 of $C_{10.8}H_{21.8}$ [72], rounded to $C_{11}H_{22}$. An example of the experiment matrix used is presented in Table 5.1 and Table 5.2 for HPO and hydrogen blends, respectively.

**Table 5.1:** Experiment matrix for HPO blends

| $\phi$ | Air flow rate [lnpm] | Kerosene flow rate [g/h] | Hydrogen flow rate [lnpm] | Angle |
|---|---|---|---|---|
| 0.7 | 5.5 | 20.3 | 0 | 22 |
| 0.8 | 6.03 | 25.4 | 0 | 24 |
| 0.9 | 6.72 | 31.84 | 0 | 24 |
| 1 | 7.06 | 37.2 | 0 | 24 |
| 1.1 | 7.01 | 40.6 | 0 | 24 |
| 1.2 | 6.02 | 38 | 0 | 26 |

**Table 5.2:** Experiment matrix for 90% Hydrogen blend

| $\phi$ | Air flow rate [lnpm] | Kerosene flow rate [g/h] | Hydrogen flow rate [lnpm] | Angle |
|---|---|---|---|---|
| 0.7 | 8.3 | 24 | 0.527 | 20 |
| 0.8 | 10.958 | 36.25 | 0.795 | 18 |
| 0.9 | 12.2594 | 45.618 | 1.009 | 18 |
| 1 | 16.63 | 68.74 | 1.51 | 14 |

## 5.4. Single PSR simulation in cantera

Analysis of the experiment results was also supported by a 0D Perfectly Stirred Reactor (PSR) in Cantera. The reactor system is arranged as shown in Figure 5.3. A mass flow controller is placed at the inlet, with values as shown in Table 5.1 & Table 5.2. A Pressure valve is placed at the outlet to maintain reactor pressure at 1 atm. Reactor volume is set at $0.00223076m^3$ and mixture temperature injected is set at $250°C$, similar to the actual experiment. A "wall" was also implemented in the simulation as a simple model to account for heat loss.

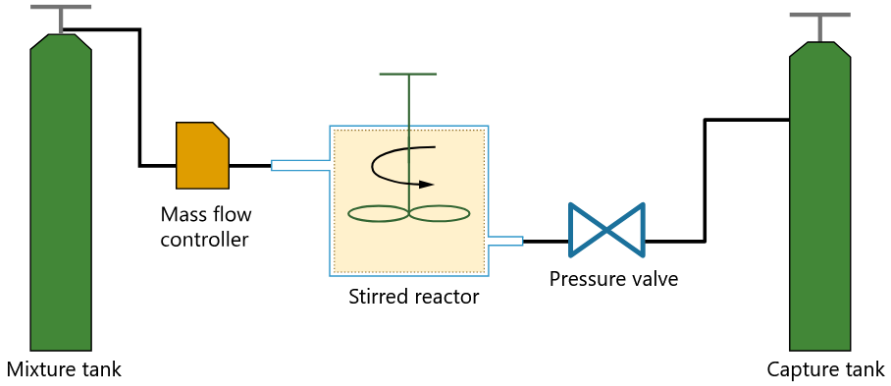


**Figure 5.3:** PSR system arrangement with mass flow control at inlet and pressure valve at outlet. [73]

The simulation was stopped when steady state is achieved, with the emission and net species production rate plotted. Equation 5.4 shows an example of a reaction equation. Reaction rate can be calculated as shown in Equation 5.6 through the Arrhenius reaction rate constant $k_f$. The sum of the all the net contributions is the net production rate of the specified species, Equation 5.7 [74]. The net contributions could also be grouped under different category by assigning specific reactions to the respective category as needed.

$$A + B \rightarrow C + D \tag{5.4}$$

$$k_f = A \cdot T^b \cdot \exp\left(\frac{-E_a}{RT}\right) \tag{5.5}$$

$$R_f = [A][B]k_f \tag{5.6}$$

$$\omega_k = \sum_i R_{f,i} \cdot n_{i,k,product} - \sum_i R_{r,i} \cdot n_{i,k,\text{ reactant}} \tag{5.7}$$

### 5.4.1. Heat loss model

A heat loss model was implemented in the simulation to account for heat transfer of the combustor. Convective heat loss was accounted through a series of equations from Equation 5.8 to Equation 5.14. $\beta$ is the reference temperature taken as the average temperature of the combustion chamber and

surface temperatures for convective heat transfer inside the chamber, and average temperature of the surface and environment for convective heat transfer outside the chamber. Pr number inside the chamber is calculated from Equation 5.9, and is assumed to be constant at 0.74 outside. $v$ is the kinematic viscosity of the mixture inside the combustion chamber and air for calculations inside and outside the combustion chamber, respectively. The two convective heat transfer coefficients can then be determined through by calculating $\Psi$, Nu, and Equation 5.12. k is thermal conductivity and h height of the chamber at 275mm. The overall convective heat transfer coefficient can then be calculated through a thermal resistance network, ignoring the conductive heat transfer resistance since the combustor wall is thin, Equation 5.13.

$$Ra_x = \frac{\beta \Delta T g x^3 Pr}{v^2} \tag{5.8}$$

$$\mathrm{Pr} = \frac{\mu_{\text{reactor}} C_{p_{reactor}}}{k_{reactor}} \tag{5.9}$$

$$\Psi = \left[1 + \left(\frac{0.492}{\mathrm{Pr}}\right)^{9/16}\right]^{-16/9} \tag{5.10}$$

$$\overline{\mathrm{Nu}}_L = 0.68 + 0.670(\mathrm{Ra}_L \Psi)^{1/4} \tag{5.11}$$

$$\bar{h}_c = \left(\frac{k}{h}\right) \overline{\mathrm{Nu}}_L \tag{5.12}$$

$$h_{c_{total}} = \frac{1}{\frac{1}{h_{c_1}} + \frac{1}{h_{c_2}}} \tag{5.13}$$

$$\dot{Q}_{\text{conv}} = h_c \cdot (T_{\text{bulk}} - T_{\text{env}}) \cdot A_{\text{quartz}} \tag{5.14}$$

Similarly, $\dot{Q}_{\text{radiation}}$ can be calculated from Equation 5.15, where $R_1, R_{w1}, R_{w2}, R_2$ are resistances as shown in Figure 5.4. Area is kept constant at $0.09m^2$, while $\varepsilon_1$ and $\varepsilon_2$ are emissivity of the gas inside the combustion chamber and of the environment, respectively. $\varepsilon_w$ is the assumed emissivity of the quartz tube used as combustion chamber, assumed to be 0.7 [75][76]. $\varepsilon_1$ was estimated through the method shown in section 3.9. Partial pressure of the gases and reactor temperature was obtained from cantera solver, while $\delta_{eq}$ was calculated from the dimensions of the actual combustor. $\varepsilon_2$ was assumed to be constant at 0.7. The area used in the calculation for Equation 5.14 & Equation 5.15 are reduced by a factor of 3.5.

$$\dot{Q} = \frac{\sigma(T_1^4 - T_2^4)}{R_1 + R_{w1} + R_{w2} + R_2} A_{quartz} \tag{5.15}$$

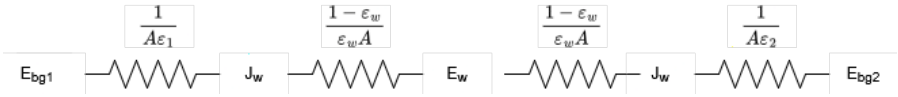


**Figure 5.4:** Radiative resistance network of hot gas and single surface enclosure

# 6

# Results and Analysis

Emission and flame speed results are analysed in this chapter. The emission results of HPO and hydrogen blends are described in section 6.1 and section 6.2. Flame speed of the fuel blends are then shown in section 6.3.

## 6.1. Emission of HPO blends

The NO, NO2, NOx, and CO emission of HPO blends are presented in Figure 6.1. The HPO blends are observed to increase NO and NOx emission quite significantly close to stoichiometric condition. The increase of NOx at lean condition is mainly caused by the increase of $NO_2$, but is relatively insignificant relative to the increase close to stoichiometric conditions.

The change in CO emission at lean condition up to $\phi$ if 1.1 is negligible. This is expected since at lean conditions, combustion is more complete, provided that residence time is higher than the chemical timescale. Unfortunately, data obtained at $\phi = 1.2$ is unreliable for Jet-A1, and a direct comparison could not be made. However, CO emission is observed to increase greatly at higher blend volume under rich conditions. Since AFR is kept constant across the fuel samples, this indicates that the HPO blends consume higher amount of oxygen.

Since the exact composition of the fuels were unknown, the reason for these differences could not be determined for certain. However, several possible reasons for the higher NOx were explored. Combustion temperature was first investigated since higher temperature would cause higher NOx emission through the thermal route. Yet, data supplied by the fuel manufacturer shows that differences in LHV of the fuel samples were negligible, and temperature is thus unlikely to be the cause.

Fuel bound Nitrogen and Oxygen were explored next, but could not justify the differences seen, either. The manufacturer reports no nitrogen content in the fuel, in line with what is typically seen in pyrolysis oil sourced from woody biomass [77][78]. In addition, fuel bound Nitrogen and Oxygen would most likely reduce LHV of HPO, which is inconsistent with the supplied LHV data.

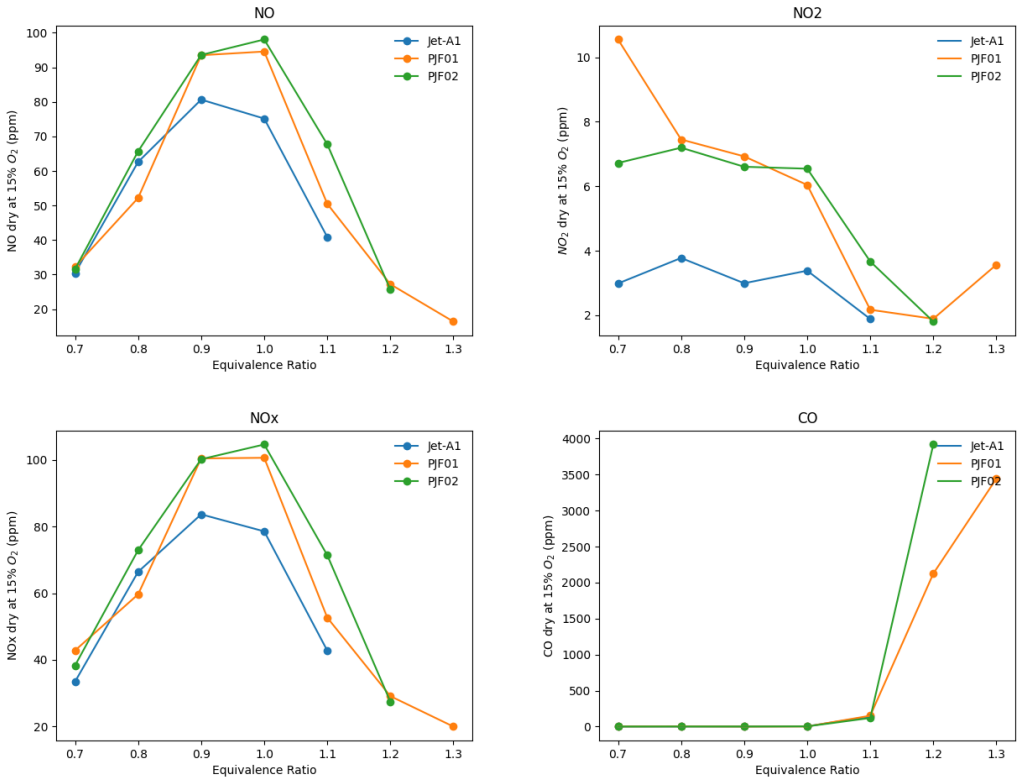


**Figure 6.1:** NO, $NO_2$, NOx, and CO emission of Jet-A1 and HPO at 10% and 20% blends (PJF01 & PJF02). $\phi$ in the plots based on $C_{11}H_{22}$.

A higher C/H ratio could possibly explain the higher NO and NOx observed, as shown in Figure 6.2. Three surrogates were used in the simulation to model different C/H ratios. Higher NO emission is observed for fuel with higher C/H ratio, $C_{10}H_{20}$, with the highest difference at stoichiometric condition. It is important to note that with the exception of Figure 6.3, the equivalence ratio used in the plots are based on the AFR of $C_{11}H_{22}$ for experiment results and $C_{10}H_{22}$ for the single PSR simulations. This is because the average molecular formula of the fuels used in the experiment was unknown. Average molecular formula of Jet-A1 could slight vary for different production batches, and information regarding the molecular formula of the two PureJet fuel blends were also absent at the time of the experiment. Thus, the average composition of Jet-A1 [72] were used as the assumed molecular formula of the fuels. A similar approach of keeping an assumed molecular formula of $C_{10}H_{22}$ were kept for the simulation to allow for a more useful comparison of the effect of C/H ratio.

When $\phi$ in the simulation was adjusted according to their respective molecular formula, the result can be seen in Figure 6.3. It can be observed that if the molecular formulas of the fuels used are assumed to be constant, there is a rightward shift in the plots for fuels with higher C/H ratio. This is because of the higher $O_2$ consumption for the combustion of fuels with lower C/H ratio.

The different contribution of the NO generation pathways are plotted in Figure 6.4. NO production through the thermal route is dominant up to $\phi$ of 1.05, but large differences in emission is only present close to stoichiometric condition. Starting from $\phi$ of 1.05, prompt NO becomes the dominant source of NOx generation. This is because the rich combustion condition favors the consumption of $N_2$ through reaction with hydrocarbon radicals which becomes abundant under rich conditions. The reverse reaction through $N_2O$ route is dominant for the consumption of NO.

It is important to note that the pathways in the plots are generated based on the consumption of $N_2$. Alternatively, the pathways can also be grouped based on equations directly consuming or producing NO, Figure 6.5. The differences are caused by the different bookkeeping. Taking NO generation through the thermal route for instance, Equation 3.1 to Equation 3.3, the grouping based on $N_2$ con-

sumption would consider Equation 3.1 under thermal pathway since it consumes $N_2$. Equation 3.2 & Equation 3.3, however, is not entirely grouped under thermal NO. There are different pathways from which $N$ consumed in the two equations can be generated, including, but not limited to Equation 3.9. Conversely, if only equations directly producing or consuming NO are used to group the pathways, Equation 3.2 & Equation 3.3 would include consumption of N produced from equations not limited to Equation 3.1 under thermal NO.

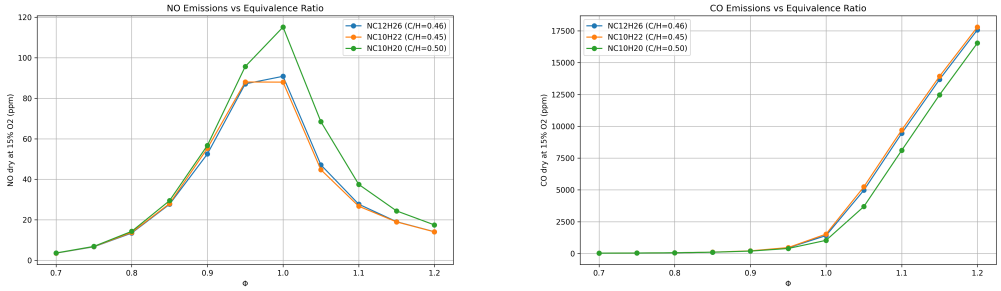


**Figure 6.2:** NO and CO emission of $C_{10}H_{20}$, $C_{10}H_{22}$, $C_{12}H_{26}$ from cantera PSR simulation; $\phi$ in the plots based on $C_{10}H_{22}$.

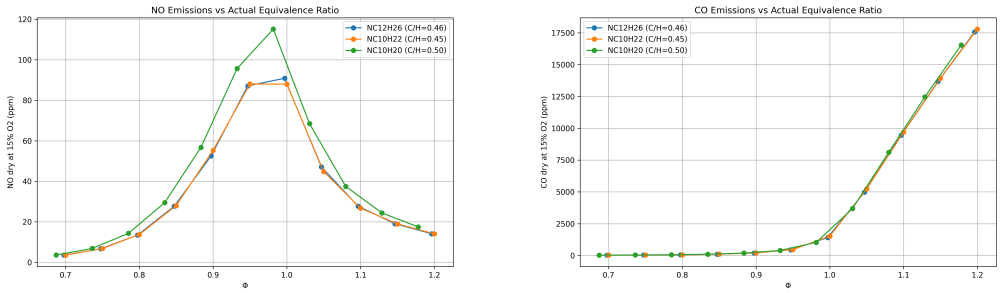


**Figure 6.3:** NO and CO emission from cantera PSR simulation, with actual $\phi$.

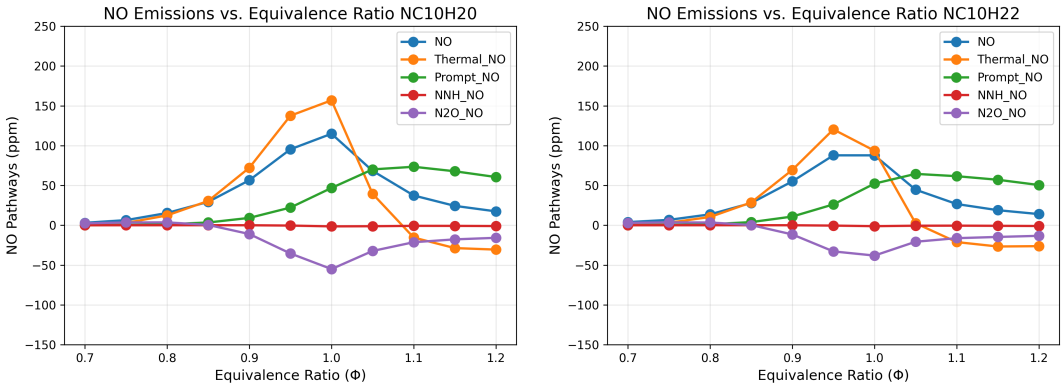


**Figure 6.4:** NO generation pathways of $C_{10}H_{20}$ & $C_{10}H_{22}$ from cantera PSR simulation; grouped based on consumption of $N_2$. $\phi$ in the plots based on $C_{10}H_{22}$

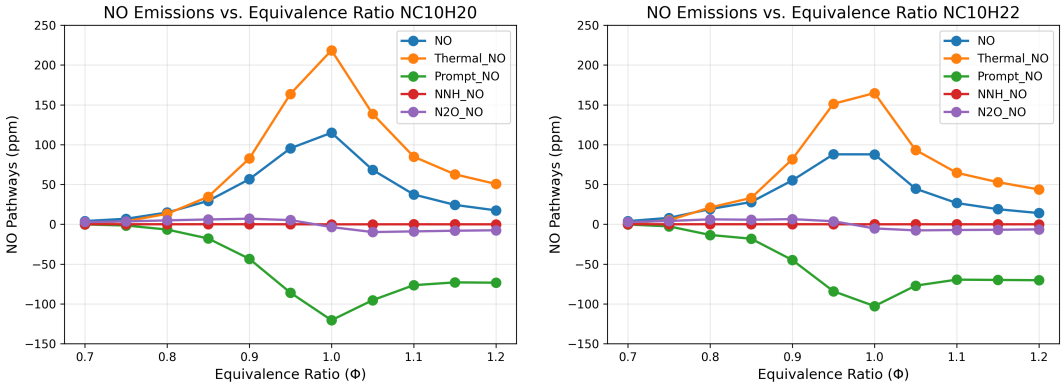


**Figure 6.5:** NO generation pathways of $C_{10}H_{20}$ & $C_{10}H_{22}$ from cantera PSR simulation; grouped based on equations explicitly producing/consuming NO. $\phi$ in the plots based on $C_{10}H_{22}$

Reactor temperature from the PSR simulation is presented in Figure 6.6. At low $\phi$, reactor temperature is nearly identical for the different fuels, and only start to diverge at stoichiometric condition. Compared to the plots of NO emission, Figure 6.2, difference in NO emission is noticeable from $\phi$ of 0.85, and peaks at 1.0. The difference in temperature for $\phi > 1.0$ is likely caused by the higher availability of oxygen for fuels with higher C/H content. For the same fuel mass, the amount of $O_2$ required to burn $C_{10}H_{20}$ is lower than $C_{10}H_{22}$, Equation 6.1 to Equation 6.6. This causes higher peak temperature at higher $\phi$ for fuels with higher C/H ratio if the amount of air supplied is kept constant. While $O_2$ availability for $C_{10}H_{20}$ is also higher at lean conditions, combustion at lean condition is always close to complete, and temperature will not change much across the fuel samples. This higher temperature close to stoichiometric and at rich condition then increases NOx emission, as seen in Figure 6.1 and Figure 6.2.

$$C_{12}H_{26} + 18.5O_2 \rightarrow 12CO_2 + 13H_2O \tag{6.1}$$

$$\text{Moles of } O_2 = 5.88 \times 18.5 \approx 108.78\,\text{mol} \tag{6.2}$$

$$C_{10}H_{22} + 15.5O_2 \rightarrow 10CO_2 + 11H_2O \tag{6.3}$$

$$\text{Moles of } O_2 = 7.04 \times 15.5 \approx 109.12\,\text{mol} \tag{6.4}$$

$$C_{10}H_{20} + 15O_2 \rightarrow 10CO_2 + 10H_2O \tag{6.5}$$

$$\text{Moles of } O_2 = 7.14 \times 15 \approx 107.1\,\text{mol} \tag{6.6}$$

Although higher C/H ratio could explain the increase in NO and NOx emission for HPO blends, the increase in CO emission at rich condition is contradictory to what is expected to be seen for fuels with higher C/H ratio in Figure 6.1. Figure 6.2 shows that fuels with higher C/H ratio will emit less CO at rich conditions for the same reason of $O_2$ availability, encouraging more complete combustion. It is important to note that emission data for $\phi$ of 1.3 may be incorrect, and may thus causes the discrepancy observed. At $\phi$ of 1.3 and possibly also at $\phi$ of 1.2, secondary combustion was observed at the exit of the combustion chamber, facilitated by ambient air. This secondary combustion may affect the emission data collected. The trend of CO increasing dramatically starting at $\phi$ 1.1 is because of the rich combustion conditions.

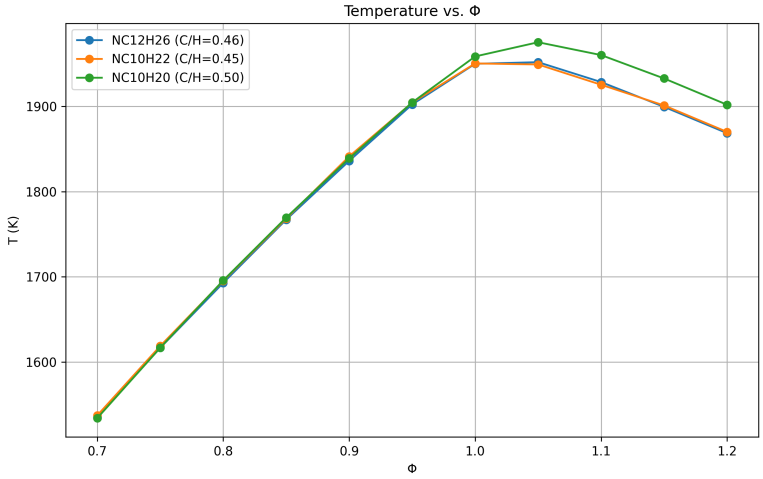


**Figure 6.6:** Temperature of the reactor simulated under cantera PSR. ; $\phi$ in the plots based on $C_{10}H_{22}$.

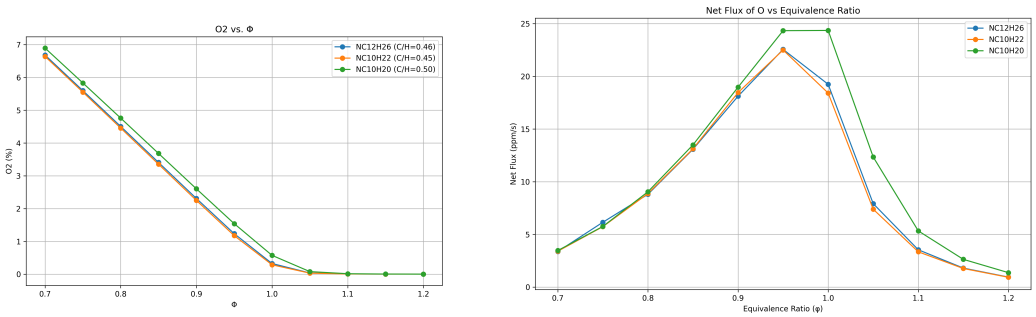


**Figure 6.7:** $O_2$ availability and o radical net fluxes of $C_{10}H_{20}$ & $C_{10}H_{22}$ from cantera PSR simulation. $\phi$ in the plots based on $C_{10}H_{22}$.

### 6.1.1. Comparison with emission of other cellulosic SAFs

Emissions of liquefied cellulosic biomass from literature is shown in Figure 6.8. It is important to note that the difference of the two biomass sources is the absence of the lignin component in cellulosic biomass. Biomass liquefication is also a separate SAF production pathway. NOx emission is seen to decrease for $\phi$ of 0.9, and increase at stoichiometric condition, while CO emission decreases for both $\phi$.

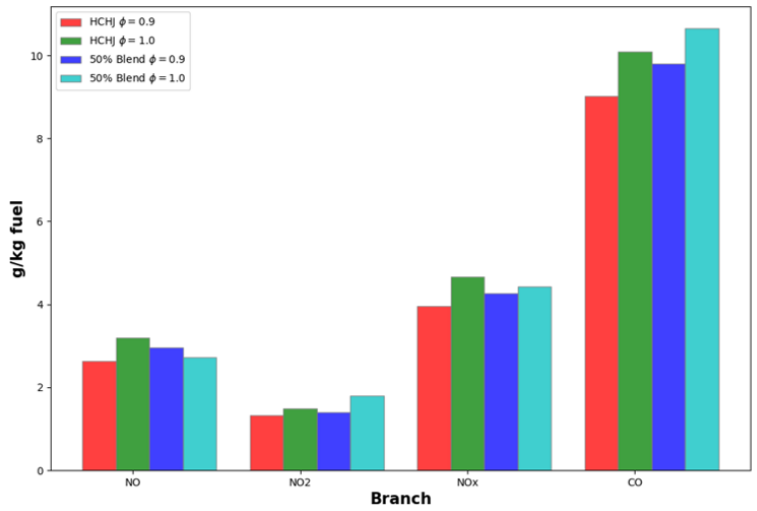


**Figure 6.8:** NOx & CO emissions of liquefied cellulosic biomass in bunsen burner setup relative to RP-3 blend [24]. HCHJ refers to Hydrothermal Condensation Hydrotreating jet fuel, the label used by the author of the paper to refer to liquefied cellulosic biomass. $50\%$ blend refers to fuel blended with RP-3.

Emission data in the current experiment can also be converted to emission index with an assumption that all carbon in the fuel is converted to CO and $CO_2$ in the combustion process, Equation 5.2. The result is presented in Figure 6.9. The trend observed is very similar to emission presented in ppm in the earlier section. This is as expected, since the index is estimated based on the an assumed average fuel composition of $C_{11}H_{22}$ that is kept constant for all fuel samples. Based on the plots presented in this section, HPO sourced from lignocellulosic biomass and HCHJ sourced from liquefied cellulosic biomass emit similar amount of NOx emissions.

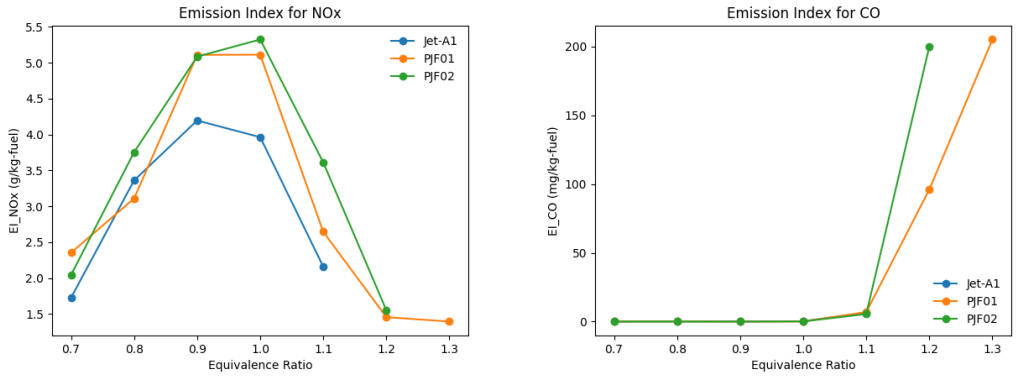


**Figure 6.9:** Emission index of NOx and CO from current experiment. $\phi$ in the plots based on $C_{10}H_{22}$.

## 6.2. Emission of Hydrogen Blends

NOx and CO emission of Jet-A1 & hydrogen blend at $90\%$ volume ratio is presented in Figure 6.10, and emission index normalized by the respective LHV is presented in Figure 6.11. In both version of the plots, NOx is observed to be similar at lean conditions, and only increases greatly at stoichiometric condition. This is likely because of larger difference in temperature for the two fuels at stoichiometric condition. Close to the stoichiometric condition, temperature is high enough to facilitate large NO emission through thermal route, and an increase in temperature at this point results in higher NOx emission. This hypothesis is supported by data from a similar experiment in literature, explained later in the section.

When the results are normalized against LHV of the fuel combusted, NOx plot for $H_2$ blend is seen to shift downward slightly relative to Jet-A1, because of the higher LHV of the hydrogen blend. It is

important to note that the result at $\phi$ of 0.9 is likely an outlier, probably from error made in the experiment, as the trend is seen to drop at that point relative to other equivalence ratios. Similar dip in flame speed at $\phi$ is also observed, as will be presented in the next section. CO emission is very similar to each other at lean condition, but is higher for pure Jet-A1. Emission only increases significantly at stoichiometric condition.

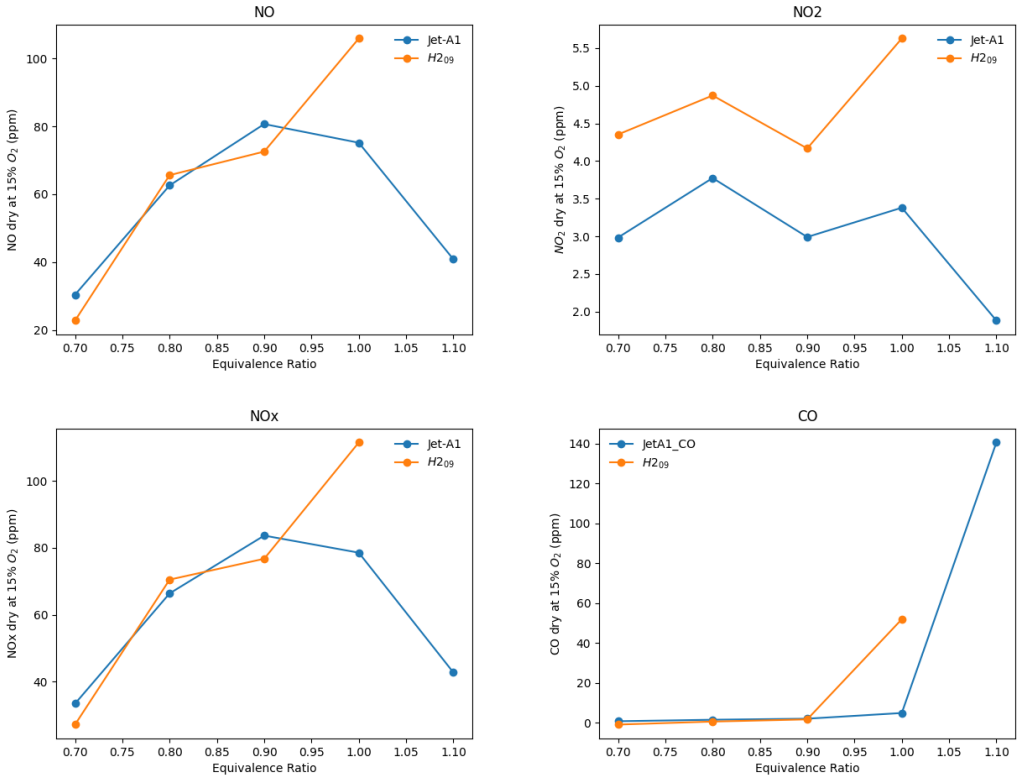


**Figure 6.10:** NOx & CO emission in ppm for Hydrogen blend.

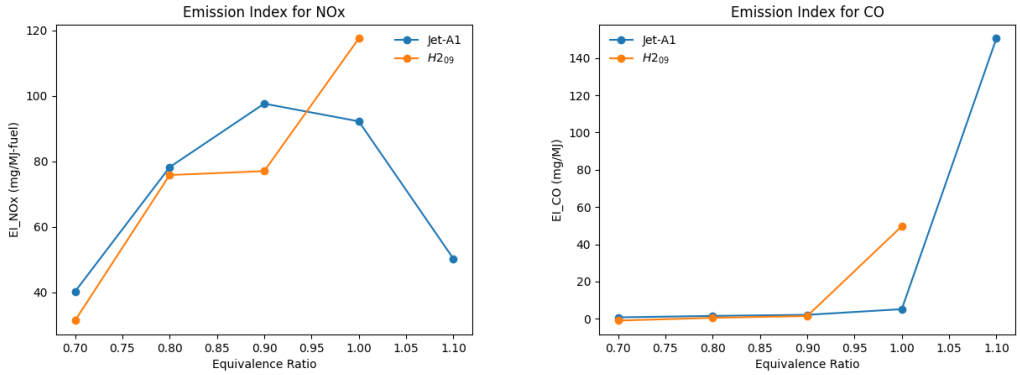


**Figure 6.11:** NOx & CO emission emission index for Hydrogen blend.

A comparison with results obtained by Frenillot et al., can be made through Figure 6.12. The effect of hydrogen addition on emission in Figure 6.12 follows a similar trend, and only a slight leftward shift towards leaner equivalence ratio is observed. NOx emission is practically constant at very lean equivalence ratio, and only starts to increase at $\phi$ of 0.8. This is likely because of higher combustion temperature of hydrogen blend, which reaches the critical temperature of 1800K earlier, a condition favorable for thermal NOx formation. The reasoning of higher combustion temperature is supported by the simulation

performed by van Dalen, S.R. [74] shown in Figure 6.13, which simulates the experiment performed by Frenillot. Keeping combustion power constant at 13kW, combustion temperature reaches 1800K at around $\phi$ of 0.75 for pure jet fuel, and at $\phi$ of 0.7 for $20\%$ mass fraction blending. Frenillot performed his experiment at power of 12.9kW and 16.5kW for $Y_{H2} = 0\%$ and $Y_{H2} = 10\%$, respectively.

The trend for CO emission in this thesis is also similar to one observed in Figure 6.12. CO is slightly lower for hydrogen blends at lean conditions, but increases significantly as it approaches stoichiometric condition, as $O_2$ availability decreases faster for hydrogen blended fuel samples. Decrease in CO emission for hydrogen blends at lean conditions is, however, higher in the results of Frenillot et al.[79].

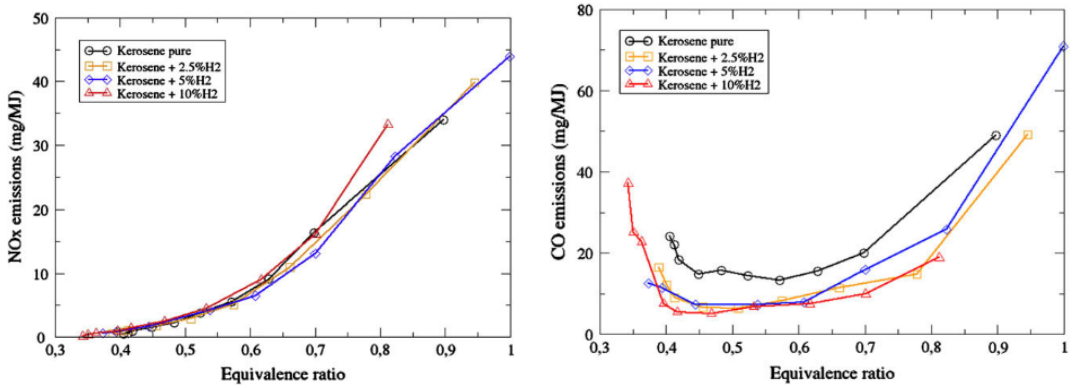


**Figure 6.12:** NOx & CO emission emission index for Hydrogen blend in a swirl stabilized burner; blending in mass fraction [79].
$Y_{H2} = 10\% \approx V_{H2} = 90\%$

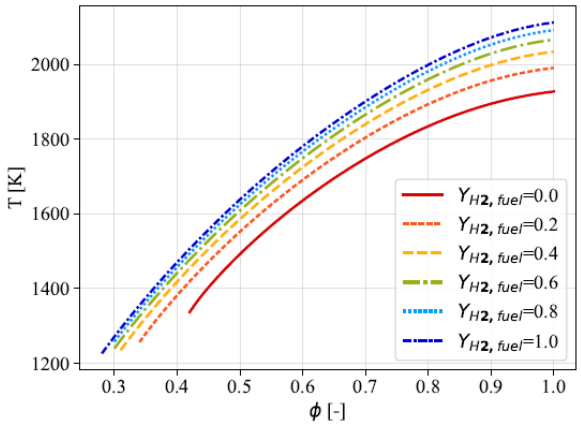


**Figure 6.13:** Estimated reactor temperature from simulation performed by van Dalen based on Frenillot's experiment [74][79].

## 6.3. Flame speed of fuel blends

Flame speed of the fuel blends are presented in Figure 6.15. A comparison of the flame speed of HPO blends with freely propagating flame simulation in cantera is provided in Figure 6.15b. The result of the simulation at mixture temperature of 473K is first compared with results seen in literature for bunsen flame Figure 6.15a to ensure that results from the simulation itself is valid.

The range of flame speed observed in literature is relatively large with difference of above $15\%$ for the peak burning velocity. The reason for this could not be determined precisely. Possible reasons that are often cited in literature are the stretch rate which is uncorrected and flame tip opening [80]. Wu [81], however, shows that effect of flame curvature on flame area is only $2\%$ in his setup and is in the same order of uncertainty from other sources. Meanwhile, flame tip opening is a phenomena observed at conditions where $Le < 1$, typically very rich kerosene flame or lean hydrogen flame [82]. However, in

Figure 6.15a, discrepancy in burning velocity is observed even at lean conditions. Evaluation on the effect of flame stretch is not performed in this paper, and may be one of the sources of uncertainties.

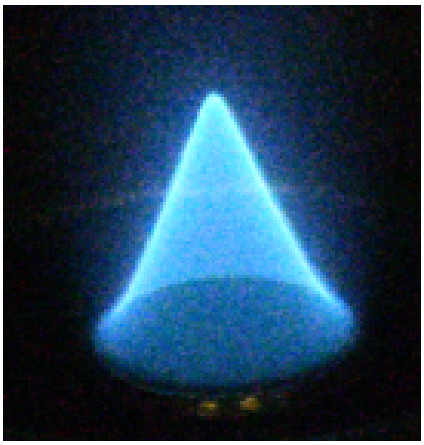

**(a)** DSLR image of PJF02 flame at $\phi = 1.0$.

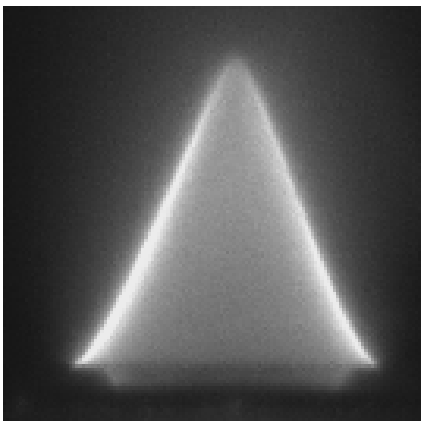

**(b)** UV image of PJF02 flame at $\phi = 1.0$.

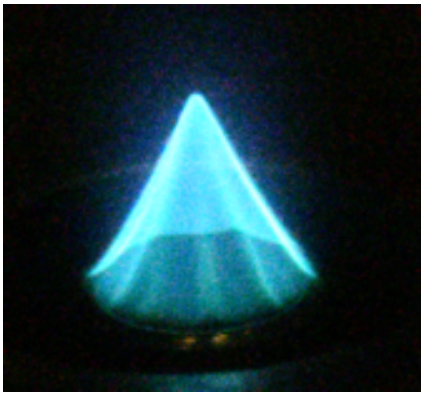

**(c)** DSLR image of PJF02 flame at $\phi = 1.2$ showing polyhderal ridges

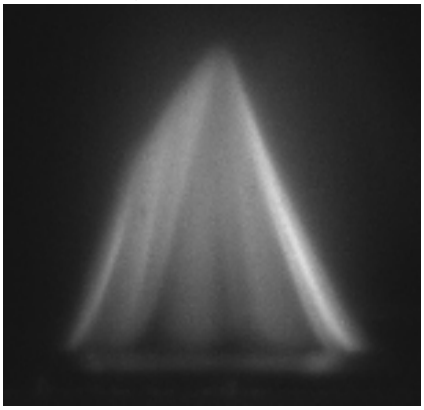

**(d)** UV image of PJF02 flame at $\phi = 1.2$ showing polyhderal ridges

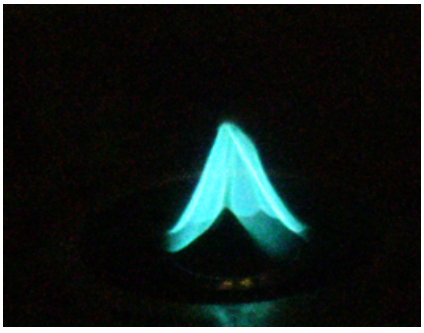

**(e)** DSLR image of PJF01 flame at $\phi = 1.3$ showing polyhderal ridges and partial extinction.

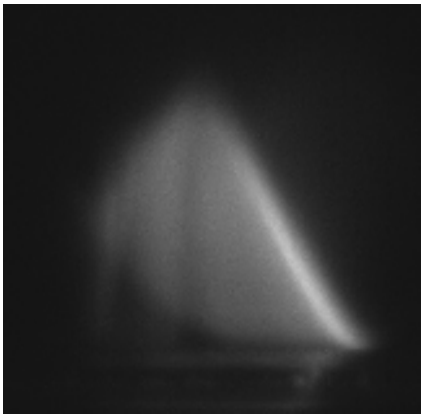

**(f)** UV image of PJF01 flame at $\phi = 1.3$ showing polyhderal ridges and partial extinction. Note that image is taken at a perpendicular angle relative to DSLR image.

**Figure 6.14:** Images of PJF01 & PJF02 flames at stoichiometric and rich conditions.

In the experiment performed for this thesis, tip opening was not observed, although polyhedral ridges were observed above $\phi$ of 1.2 Figure 6.14c & Figure 6.14d. This significantly degraded the performance of flame edge detection algorithm, and the edges were manually determined, then. Result for PJF01 at $\phi$ of 1.3 is excluded because the flame was partially extinguished Figure 6.14e & Figure 6.14f. As comparison, burning velocity typically obtained from a spherical combustion setup is shown in Figure 6.15d.

Result is typically more consistent across papers, and appear to match values in the lower range of bunsen setup.

Flame speed results from the experiment Figure 6.15b shows that HPO blending on Jet-A1 does not alter flame speed. Differences in flame speed across the fuel samples are minimal, and no meaningful trend of increase or decrease in flame speed can be observed. This indicates that the fuel is a suitable candidate as SAF in terms of combustion stability.

Figure 6.15c shows that flame speed of hydrogen blended fuel increases significantly across equivalence ratio. This is expected since hydrogen flame has a much higher burning velocity. The dip in flame speed for $\phi = 0.9$ is likely due to experiment error in the control of fuel/air flow rate or injection. The emission of $H_2$ blend in section 6.2 shows a similar dip at the same point. Flame speed for the hydrogen blend is also lower than the results obtained through simulation. This is likely caused by deficiency in the mechanism in simulating flame speed for hydrogen blends. Zhang [83] performed a similar experiment on flame speed for hydrogen blending in a spherical combustor Figure 6.16. The results shows increasing over-prediction of flame speed at increasing mass ratio. The similar flame speed of the PureJet blends are expected, since the fuels have similar LHVs, and the higher flame speed of hydrogen blend is because of the higher LHV of the fuel.

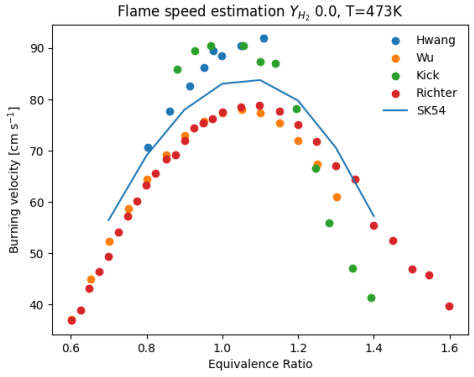


**(a)** Burning velocity of Jet-A1 in a bunsen burner setup from different literature at $T_0 = 473K$ [41][84][85][86][87]; plotted against freely propagating flame speed simulated in cantera with SK54.

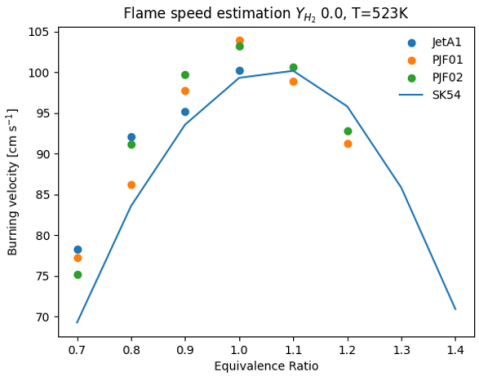


**(b)** Burning velocity of Jet-A1 and HPO blends from experiment in this thesis at $T_0 = 532K$; plotted against freely propagating flame speed simulated in cantera with SK54.

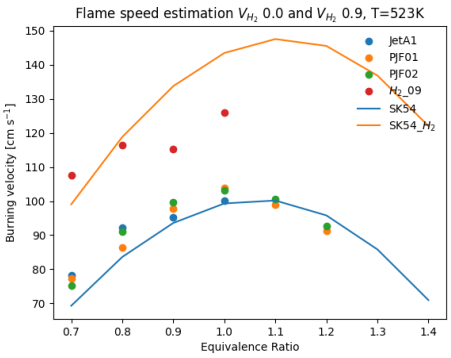


**(c)** Burning velocity of Jet-A1, HPO, and hydrogen blends from experiment in this thesis.

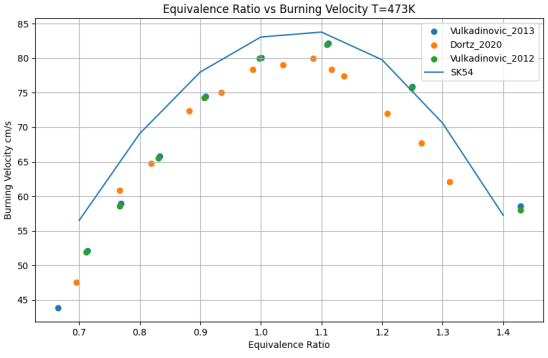


**(d)** Burning velocity of Jet-A1 in a spherical combustion chamber from different papers at $T_0 = 473K$ [88][89][90]

**Figure 6.15:** Burning velocity from literature and experiment conducted for this thesis.

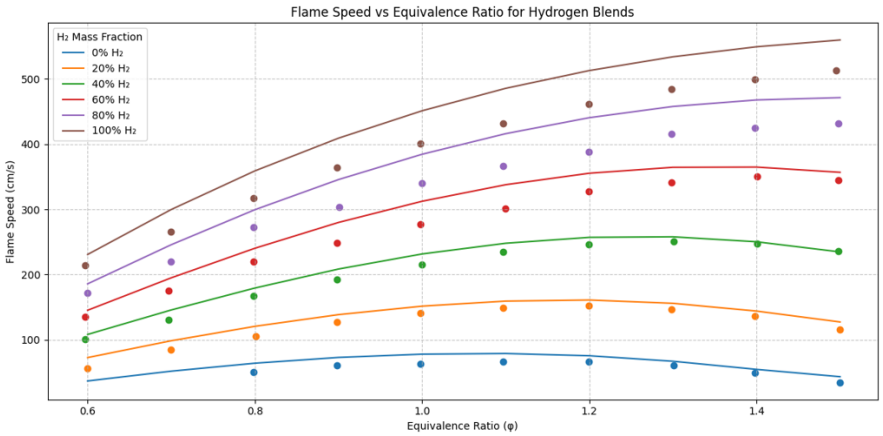


**Figure 6.16:** Burning velocity of n-dodecane & Hydrogen blends, at different mass blending ratio [83].
$Y_{H2} = 10\% \approx V_{H2} = 90\%$

# 7

# Proposed modifications to Swirl Combustor Setup

This chapter explains the modifications performed on the current bunsen setup described in the previous chapters and the swirl combustor in the lab. The modification shall allow for swirl stabilized combustion of premixed pre-vaporized kerosene/biofuels. The existing swirl burner setup is first described in section 7.1. Requirements and parameters of the design is then described in section 7.2, followed by the methods used for the modifications in section 7.3. The resulting modifications proposed is described in section 7.4, with the P&ID and simplified design overview presented in section 7.5.

## 7.1. Existing setup

A separate modification to a setup used in a previous thesis about hydrogen combustion by van den Bergh [59] is proposed to allow future experiments in a swirl stabilized LPP combustor. A visualization of the existing design is shown in Figure 7.1. Most of the air is injected radially through the air ports, which then pass through the swirler. Downstream of the swirler, fuel is again injected radially and undergo mixing in the mixing tube. Part of the air injected can also be injected axially through the Axial Air Injection (AAI) port. This is to improve the flashback performance of the combustion process, which is especially important for hydrogen flames in swirling flows because of VBD described in the previous section.

During previous experiments in this burner, it was discovered that fuel air mixing performance was insufficient. The modification would attempt to resolve this problem, while at the same time integrating several heating systems to allow for combustion of prevaporized kerosene/biofuels. This chapter will thus answer research question number three.

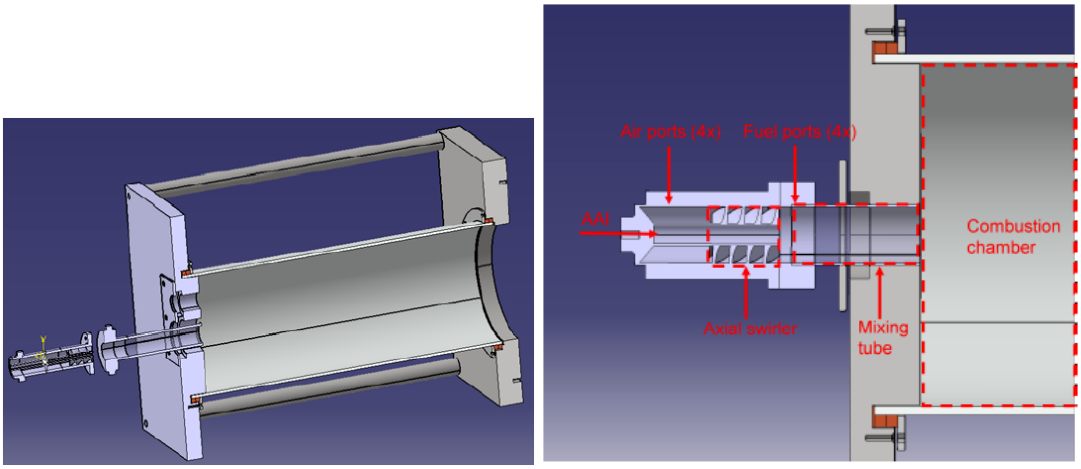


**Figure 7.1:** Current experimental setup, showing the swirler, mixing tube, and combustion chamber.

## 7.2. Design Framework

The objective of the setup redesign is to allow the pre-vaporization and premixing of liquid kerosene/bio-fuels in the current setup. The fuel-air mixture will also be mixed prior to combustion, thereby achieving lean premixed pre-vaporized combustion. This section will outline the requirements, parameters, and constraints derived from the requirements on the design.

### 7.2.1. Design requirements

- Reynolds number in the mixing chamber and swirler shall be above 4000
- Estimated temperature of the mixture before the combustion chamber shall be above $150°C$
- Penetration depth of the jet fuel injection shall be larger than radius of the mixing mixing tube
- Bulk velocity in mixing tube and swirler shall not be lower than the lowest estimated turbulent flame speed
- Heaters shall have sufficient heating capacity to fully vaporize liquid kerosene
- Minimum flow rate of the heaters shall be higher than the minimum experiment airflow
- Setup shall allow experiments to be performed at varying $\phi$ from 0.3 to 1.0.

### 7.2.2. Design Parameters

- **O-Geom-1** Mixing tube length $L_{mt}$
- **O-Geom-2** AAI hub diameter $D_{AAI}$
- **O-Geom-3** Helix pitch, $P_{hel}$
- **O-Flow-1** Heating power required $P_{heat}$
- **I-Geom-1** Geometric Swirl Number $SW_{geo}$
- **I-Geom-2** Wall thickness $t_{wall}$
- **I-Geom-3** Fuel injector diameter $D_{inj}$
- **I-Geom-4** Mixing tube inner diameter $D_{mt}$
- **I-Flow-1** Equivalence Ratio $\phi$
- **I-Flow-2** Combustion power $P_{combustion}$
- **I-Flow-3** Fuel port air amount $m_{air_{fp}}$

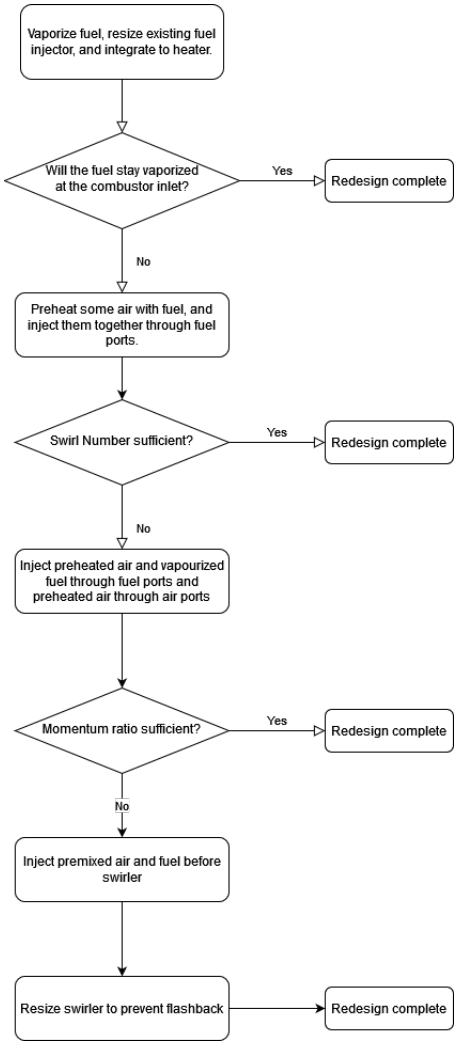


**Figure 7.2:** Flow diagram of the design steps

### 7.2.3. Design Constraints

Design constraints is derived from the requirements listed previously. They are listed as shown below.

- Reynolds Number Re » 4000
- Swirl Number SW > 0.7
- Bulk velocity $U_0 > S_T$. $S_c$ estimated to be around 2 to 2.5m/s[91][92][93].
- Mixture temperature $T_{mix} = 250°C$
- Penetration depth $Y_{max} > \frac{1}{2} D_{mt}$

## 7.3. Methods

A python code was written to determine the optimal design of the setup modifications based on the requirements and constraints defined before. The redesign steps of the setup will follow the logic shown in Figure 7.2 with schematics as shown in Figure 7.3a. The simplest design looks into vaporizing the fuel using the heating system, which will be integrated with the existing system. The prevaporised fuel will then injected through the fuel ports. One problem that can be foreseen in this setup is the insufficiently high temperature at the end of the mixing chamber, which means the it cannot be ensured that the fuel will stay prevaporized at the end of the combustion chamber. The mass of fuel injected for the mixture is usually one to two order of magnitude lower than the amount of air.

A possible solution will be to also preheat some air with the fuel such that the heat balance of the mixture will not drop below the saturation temperature of the fuel Figure 7.3b. However, this may cause a separate problem on the swirl number at the combustion chamber. Increase in the mass of air and fuel injected through the fuel ports will degrade the swirl number of the flow. It is also difficult to maintain temperature at the outlet of the mixing tube since only a minor portion of air is heated.

Another possible redesign option, design C in Figure 7.3c, is to also inject preheated air in the air ports. This will allow temperature at the outlet to be effectively controlled, but still present mixing degradation performance because it will lower the momentum ratio of the injected fuel to injected air. Design D Figure 7.3d, however, would prevent swirl degradation caused by injecting fuel, by installing the swirler downstream of the fuel injection point. This design, however, makes it difficult to locate the point where combustion stabilizes in case of flashback, and therefore, lowers the safety level of the setup.

### 7.3.1. Thermal power required for fuel vaporization

Another aspect that has to be considered is the heater capacity and heat loss in the setup. If heating capacity of the heater is insufficient, trace heating could be used to heat the air upstream of the heater unit, thereby reducing the heat load required. Insulation will also be used in the setup to lower heat loss to the surrounding. A simple heat loss model will be made to estimate the necessary insulation needed.

The required thermal power to vaporize the fuel can be estimated by simple heat capacity estimations, Equation 7.1. $C_{fuel}$ is the fuel heat capacity, assumed to be $2090K/kgK$ [72] in liquid phase, and calculated through NASA polynomial estimations for gaseous phase [94]. Latent heat of vaporization is assumed to be $0.36MJ/kgK$ [72]. A similar equation for the thermal capacity of air is used, and iterated until a balance of temperature is achieved, to obtain the temperature of the fuel-air mixture in the pre-vaporizing section.

In addition, Equation 7.2 to Equation 7.6 are used to estimate heat loss of the fuel line due to convection [95]. Ra is the Rayleigh number, $T_e$ is the estimated environment temperature, $\beta$ is the film temperature, L is the assumed pipe length, Pr is the Prandtl number, and v is the kinematic viscosity.

Equation 7.7 estimates heat loss by radiation to the surrounding. The final temperature of the mixture will be set at $250°C$. A suitable heater power can then be selected based on the required thermal power, accounting for vaporization energy, temperature increase, and heat loss to the surrounding. After the design and dimensions of the parts are finalized, a drawing of the redesigned parts would be made in a CAD software.

$$Q_{fuel} = \dot{m}_{fuel} \cdot C_{fuel} \left(T_2 - T_1\right) + m \cdot L_{vap} \tag{7.1}$$

$$Ra = \beta * (T_{pipe} - T_e) * 9.81 * L^3 * \frac{Pr}{v^2} \tag{7.2}$$

$$\Psi = \left(1 + \left(\frac{.492}{Pr}\right)^{\frac{9}{16}}\right)^{\frac{-16}{9}} \tag{7.3}$$

$$\overline{\mathrm{Nu}}_L = 0.68 + 0.670 \left(\mathrm{Ra}_L \, \Psi\right)^{1/4}; \quad \mathrm{Ra} \leqslant 10^9 \tag{7.4}$$

$$h_{conv} = \frac{Nu \cdot k}{L} \tag{7.5}$$

$$Q_{convection} = h_{conv}(T_{pipe}, T_e, L, k) \cdot \pi \cdot d \cdot L \cdot (T_{pipe} - T_e) \tag{7.6}$$

$$Q_{radiation} = \sigma(T_{system}^4 - T_e^4) \cdot \epsilon \cdot \pi \cdot d \cdot L \tag{7.7}$$

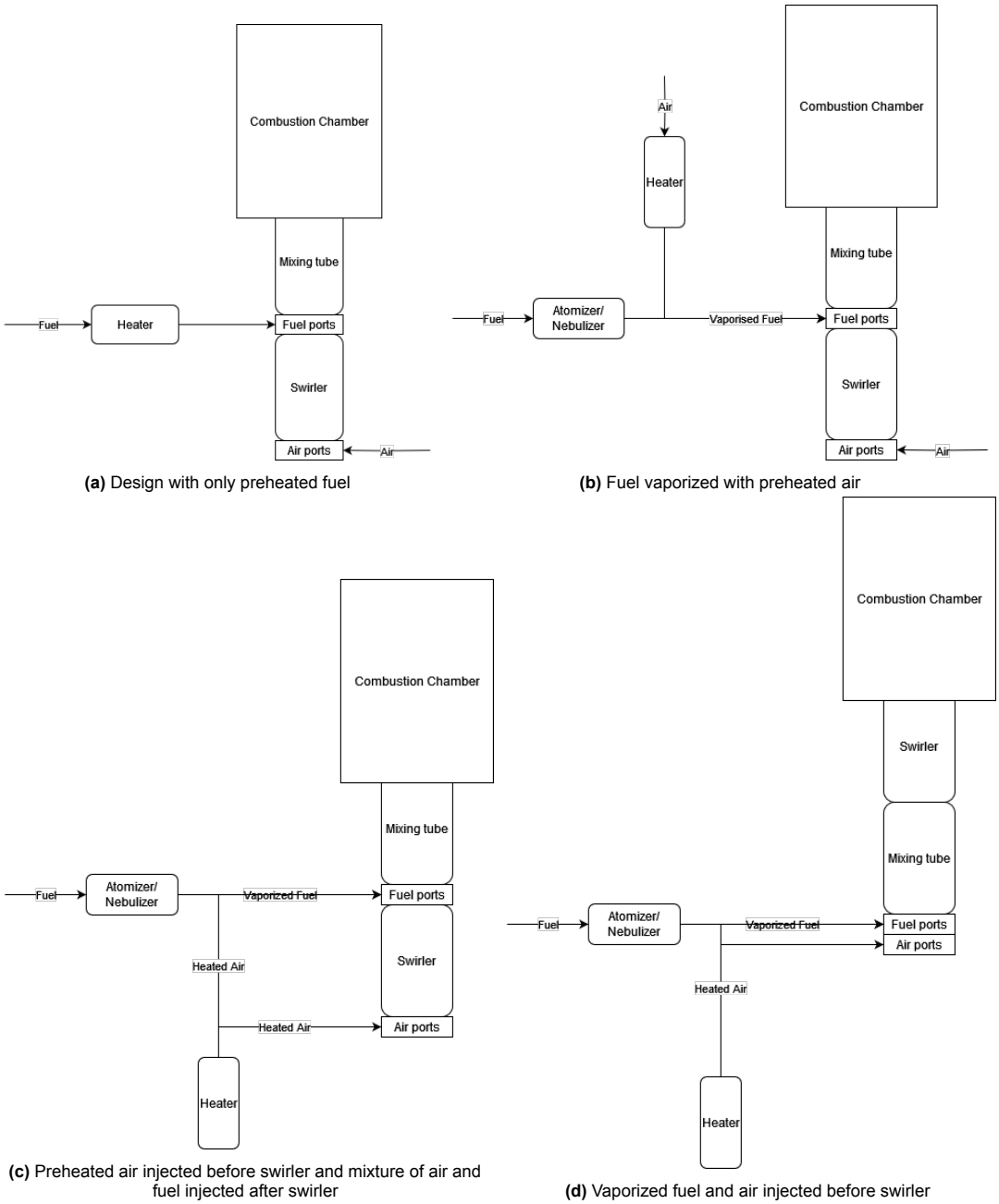


**(a)** Design with only preheated fuel

**(b)** Fuel vaporized with preheated air

**(c)** Preheated air injected before swirler and mixture of air and fuel injected after swirler

**(d)** Vaporized fuel and air injected before swirler

**Figure 7.3:** Possible redesign solutions.

## 7.4. Design Choices and Setup Sizing

The motivation of the choices made in the design and sizing of the modified setup is described in this section. First, one of the four designs presented in Figure 7.3 had to be selected. Design A and B were immediately eliminated, because it was reasoned that if the main combustion air remain unheated, the pre-vaporized fuel could potentially locally condense back into droplets in the mixing tube. Design A is also determined to be less safe because fuel is heated directly with the heater, and may be directly exposed to temperature up to $900°C$ and ambient air if there is a leakage. This increases the risk of unintended fire.

To select between design C and D, the pro and cons of of the two designs were compared. Design C would adversely affect the swirl number of the mixture. Injecting fuel downstream of the swirler could potentially degrade swirl number to low swirl or, potentially eliminate it. Design D, however, would make it difficult to locate the point where the flame stabilizes if flashback occurs, increasing safety risks. Since it is unknown how much exactly the swirl number will be affected, design C is selected for this experiment, considering the more challenging safety requirements for design D. If it was observed during the experiment that the swirl number is degraded to low swirl, design D can be used for future experiments.

An estimation of swirl degradation in the mixing tube was made based on empirical equations shown in Equation 3.32. For mixing tube with length of 5 diameters, and assumed $\beta$ value of 0.1, swirl number at the end of the mixing tube will be $60.7\%$ of the value at inlet of the mixing tube. This does not include the degradation caused by fuel-air jet injection just before the mixing tube.

### 7.4.1. Swirler & Mixing tube geometry

With the general outline of the subsystems fixed, design C was further developed, and the subsystems was sized accordingly. Referring to Table 7.1, some parameters, including mixing tube inner diameter $D_{mt}$, AAI inner diameter $D_{AAI}$, and wall thickness $t_{AAI}$ are kept unchanged because they do not violate the set constraints, and modifying them will not improve the performance of the setup. The length of the mixing tube is lengthened to 120mm ($5D_{mt}$) to facilitate better mixing, as previously shown in Figure 3.24a and Figure 3.22. A plenum is also used just before the swirler. A long plenum would allow for a more stable flow, but will increase heat loss at the same time. A length of 168 was chosen to maintain low heat loss. The length of AAI tube is extended to accommodate the length of the plenum, as shown in Figure 7.4a.

Meanwhile, swirler pitch will be modified to increase the swirl number to 1.5. This is because it can be expected that injecting $20\%$ of combustion air as carrier gas with the fuel will cause significant swirl degradation, as shown in section 3.7. Keeping the original number of vanes at eight, swirl angle and pitch can then be calculated with Equation 3.28 to Equation 3.31. The result is summarized in Table 7.2

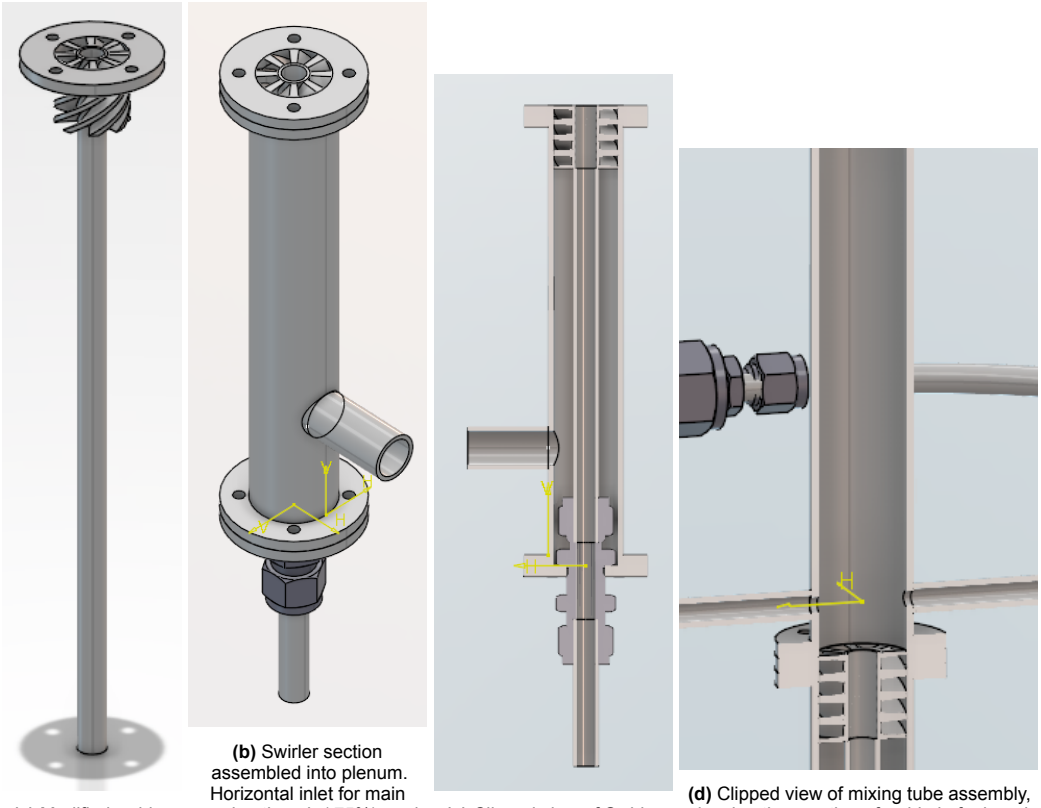

**(a)** Modified swirler, with longer AAI tube

**(b)** Swirler section assembled into plenum. Horizontal inlet for main combustion air ( 75%), and vertical AAI inlet.

**(c)** Clipped view of Swirler assembly.

**(d)** Clipped view of mixing tube assembly, showing the meeting of swirl air, fuel, and AAI.

**Figure 7.4:** Snapshot of inlet and outlet of fuel line. Complete design is available in appendix.

**Table 7.1:** Selected geometry parameters of the modified setup

| Geometry Parameter | Symbol | Value | Unit |
|---|---|---|---|
| Mixing tube inner diameter | $D_{mt}$ | 24 | mm |
| Mixing tube length | $L_{mt}$ | 120 | mm |
| AAI inner diameter | $D_{AAI}$ | 8 | mm |
| AAI wall thickness | $t_{AAI}$ | 1 | mm |
| Plenum length | $L_{plenum}$ | 168 | mm |
| Fuel port diameter (vaporized) | $D_{inj}$ | 4 | mm |
| Air line outer diameter | $D_{air}$ | 16 | mm |

**Table 7.2:** Swirler properties with swirl number 1.5

| Description | Value | Unit |
|---|---|---|
| Blockage Factor | 0.3671 | – |
| Helicoidal pitch | 46.61 | mm |
| Tip radius | 12 | mm |
| Hub radius | 5 | mm |
| Tip angle | 58.28 | ° |
| Hub angle | 33.98 | ° |

### 7.4.2. Heater Selection

The heater power were selected based on estimations of the thermal power required for heating the air to $250°C$ and fuel vaporization, as well as losses to the environment. The estimations made were based

on Equation 7.1 to Equation 7.7. The dimensions used for the calculation were conservative, accounting for margins for design revisions or modifications. These were 25mm for air line diameter and 2m length. Fuel line were assumed to be of diameter 15mm and length 2m, which is also conservative. In addition, the base heating power required, as calculated from Equation 7.1 assumes a $\dot{m}_{fuel}$ for combustion at 20kW instead of 11kW. This is intended to allow for higher combustion power experiments in the future.

This method of heater power requirement was validated on the basis of comparison with literature [96][97][98] for the typical heater power used for their respective flow rates. The estimations were found to under-predict power of the heaters by $30\%$. A correction factor of 1.3 was therefore used to adjust the result of the estimation. The result of these estimations is shown in Table 7.3. Based on the required heating powers, the heater models recommended are Tutco Sureheat 8000W & 4000W, and AHPF-102. The choice of injecting 20% of combustion air through the fuel line is based on the minimum required flow rate of the heater of the Tutco heater of about 28lpm.

**Table 7.3:** Required thermal power to raise temperature to $250°C$

| Item | Heating power [W] | After efficiency & heat loss [W] | After correction factor [W] |
|---|---|---|---|
| Fuel line (H-001) | 1368 | 2290 | 3000 |
| AAI (H-002) | 521.5 | 654 | 850 |
| Main combustion air (H-003) | 4172 | 5150 | 6700 |

### 7.4.3. Fuel line design

The overall design of the fuel line can be viewed in Appendix A. To ensure that the fuel combusted is fully vaporized, it was determined that it is best if a 1 meter fuel pre-vaporizing section is used before being introduced to the mixing tube. This is because the mixing tube is only 120mm long. The fuel is assumed to be fully vaporized before being introduced to mixing tube. Liquid fuel and air will be introduced through a T-joint at inlet of the pre-vaporizer Figure 7.5a. Fuel is injected vertically, and heated air horizontally. This arrangement prevents liquid fuel from inadvertently flowing into the heater because of gravity. An atomizer is placed at the inlet of the fuel section to improve fuel vaporization performance. At the outlet, another T-section is used to split the fuel-air mixture into two lines, before injected to the mixing tube in a jet in co-flow configuration Figure 7.5b.

Fuel ports injection velocity and momentum ratio depends on the selected port diameter, which selection is based on ensuring sufficient fuel penetration depth of at least 0.5 diameter. Care was taken to ensure injection velocity does not reach choking velocity. The proportion of air used to vaporize the liquid fuel is kept at the lowest amount, whilst ensuring that it is always above the heater minimum flow rate. AAI is also kept at the minimum since it can be expected that kerosene is relatively resistant to flashback at the experiment region. A bulkhead joint is used to seal the gap between the AAI tube and plenum bottom flange. The expected penetration depth and flow speed from the 4mm fuel ports is shown in Table 7.4.

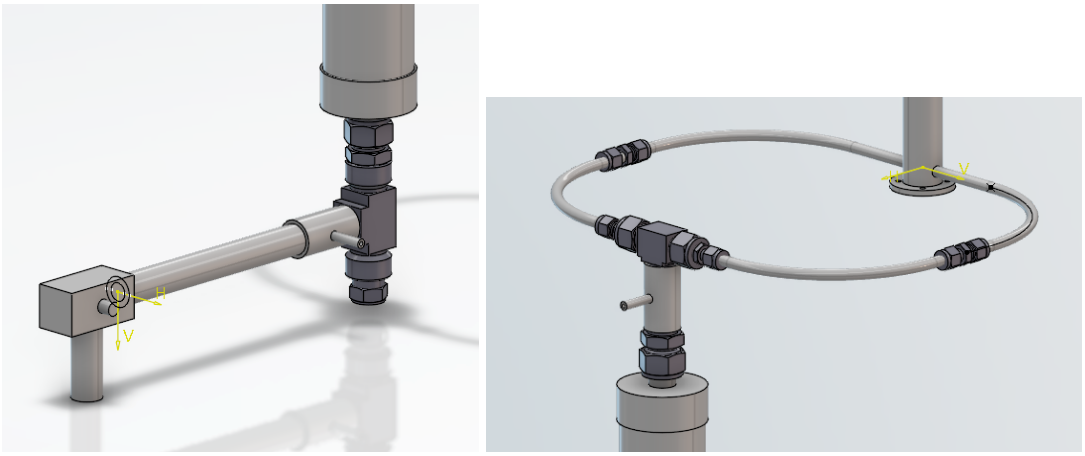


**(a)** Inlet of the fuel line, where liquid fuel and $20\%$ of air are injected through a T-joint

**(b)** Outlet of fuel line and injection of mixture into mixing tube from two separate lines

**Figure 7.5:** Snapshot of inlet and outlet of fuel line. Complete design is available in appendix.

The 1 meter pre-vaporizing section could be made of a typical steel tube wrapped in trace heater and insulation to maintain constant temperature for the pre-vaporizing tube. Alternatively, this section can also be made out of Swagelok's FV series Vacuum-Insulated Metal Hose. The choice of steel tube wrapped in trace heater is preferred, since high temperature could be maintained throughout the section despite of the reduction of temperature from fuel vaporization. However, Swagelok's vacuum tube could be a good alternative to reduce heat loss to the environment.

The flow parameters of the setup is presented in Table 7.4. The combustion power is set at 11kW, continuing the typical power the combustor operates at for previous experiments. $\phi$ is varied from 0.3 to 1.0 by varying the amount of air in the mixture used for combustion. It is ensured that Re number stays above 7000 and bulk velocity is higher than $9m/s$ for all the $\phi$.

**Table 7.4:** Flow and general parameters of the experiment

| Flow parameter | Symbol | Value | Unit |
|---|---|---|---|
| Combustion Power | $P_{combustion}$ | 11 | kW |
| Equivalence ratio hydrogen | $\phi_{C_{11.4}H_{21.7}}$ | 0.3 to 1.0 | – |
| Air volume flow rate | $V_{\text{air}}$ | 170 to 580 | lnpm |
| Fuel volume flow rate | $V_{fuel}$ | 18.3 | ml/min |
| Air mass flow rate | $\dot{m}_{\text{air}}$ | 3.73 to 12.4 | gram/s |
| Fuel mass flow rate | $\dot{m}_{fuel}$ | 0.256 | gram/s |
| Mixing tube Reynolds number | $Re_{mt}$ | >7000 | – |
| Mixing tube bulk velocity | $U_{mt}$ | 9 to 35 | m/s |
| Fuel ports injection velocity | $U_{fp}$ | 45 to 200 | m/s |
| AAI heater power | $P_{AAI}$ | 400 or 1200 | W |
| Fuel line heater power | $P_{fl}$ | 4000 | W |
| Main air line heater power | $P_{al}$ | 8000 | W |
| AAI airflow proportion | $\dot{m}_{\text{AAI}_p}$ | 5 | % |
| Fuel line airflow proportion | $\dot{m}_{\text{fl}_p}$ | 20 | % |
| Maximum penetration depth | $Y_{max}$ | 24.8 to 25.3 | mm |
| Momentum ratio | J | 28.9 to 30.2 | – |

## 7.5. Design Overview

The detailed design choices of the system have been described in the previous section. This section aims to shows how the system operates together. Detailed CAD drawings of the parts are presented in the appendix.

P&ID of the system is shown in Figure 7.6. Cold air from the lab will be supplied to three lines, with $75\%$ of it going through the right, main air line. 20% of the air will go through the left, fuel(-air) line, and the remaining 5% goes through the center AAI line. All three lines are heated. Liquid fuel will be introduced to left fuel line, as described in subsection 7.4.3. The right main air line will go through the swirler in the swirler/plenum tube, while the center AAI line will bypass the swirler through the hollow swirler center, as shown in Figure 7.4c. Finally, air and fuel from the three lines will meet at the mixing tube, as shown in Figure 7.4d. At the end of mixing tube, the mixture introduced into the combustion chamber should be fully premixed and pre-vaporized.

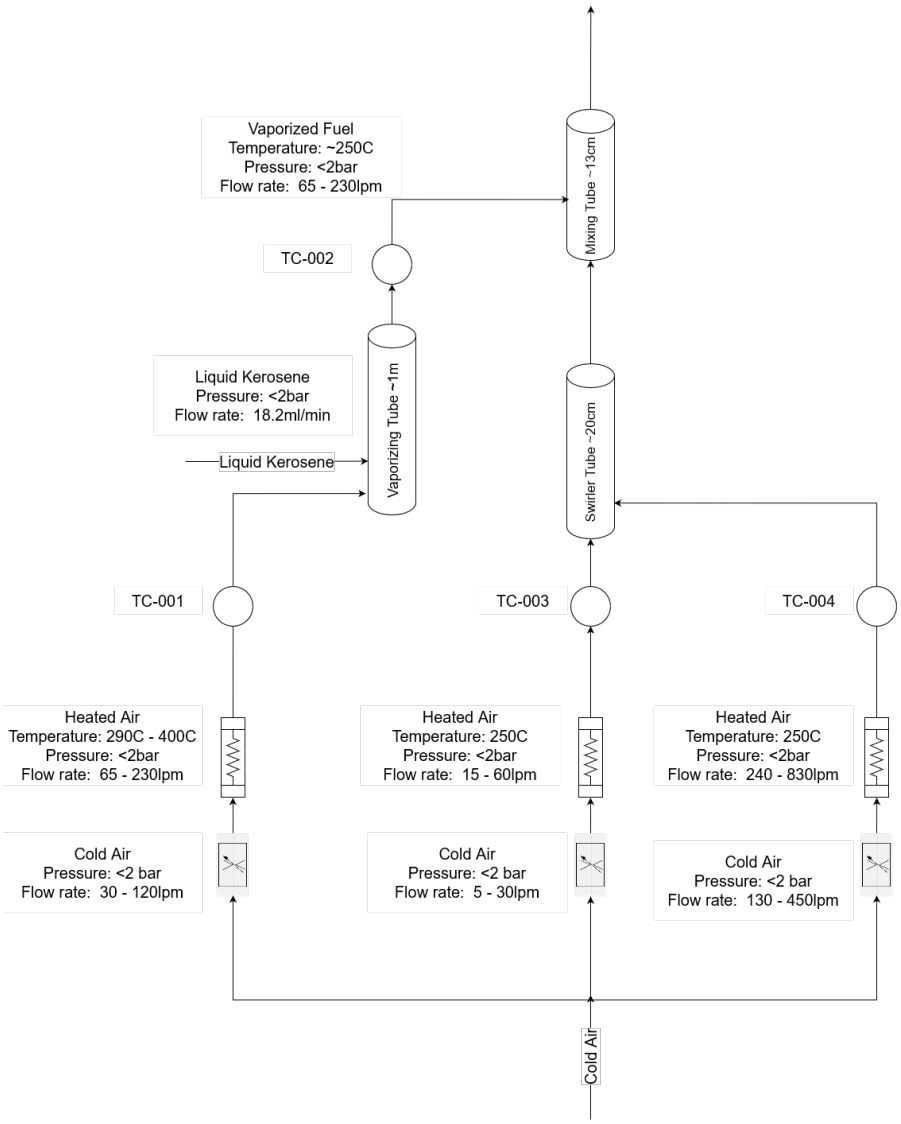


**Figure 7.6:** P&ID of experiment system showing flow properties

# 8

# Conclusion

The transition to sustainable aviation requires a large scaling up in the production of alternative fuels. Aside from the HEFA based SAFs, additional production pathways are required to meet the demand of biofuels in aviation. HPO was proposed to be one of these additional production pathways. Data on flame speed and emissions HPOs as SAF is still scarce in literature. This thesis thus, looks at the suitability of HPO blends as a potential candidate for SAFs in terms on flame speed, as well as NOx and CO emissions. Because of the high interest in hydrogen for the aviation sector, the effect of blending hydrogen in Jet-A1 on flame speed and emissions was also explored.

Experiment was performed in a laminar bunsen setup supported by single PSR simulation in cantera. A modification to existing swirl combustor in the lab was also proposed to accommodate swirl stabilized premixed pre-vaporized combustion. In short, three research (sub)questions are answered, as follows:

1. **What are the changes in flame speed of Jet-A1 when blended with biofuels and hydrogen?**

   Flame speed does not vary much across the different fuels for PureJet blends. This is because of the similar values of the fuels' LHVs. The differences seen in the results likely come from uncertainty in the experiment. In the case of hydrogen blend, flame speed was observed to shift upwards because of the higher LHV of the fuel blend.

2. **What are the changes in NOx and CO emission that can be observed for jet-A1 blended with biofuel and hydrogen?**

   NOx emission increases significantly for PureJet blends close to stoichiometric condition. Single PSR simulation showed that the increase could be cause by a higher C/H ratio of the fuel. There is also a rightward shift of the results because of the different effective equivalence ratio of the higher C/H fuel. When adjusted for their actual equivalence ratio, the simulation showed that NOx emission increases for all equivalence ratio, and the increase still peaked close to stoichiometric conditions. CO emission for PureJet blends increases at rich conditions, but was very similar at lean conditions.

   For hydrogen blends, NO emission was observed to also increase st stoichiometric condition. This is likely caused by combustion temperature at this equivalence ratio. A simulation performed by Sanders [74] for a similar experiment in literature shows that large differences in NO emission is only seen above temperature of 1800K. Similarly, CO emission is also only observed to increase at stoichiometric condition.

3. **What modifications have to be made to the existing setup to allow swirl-stabilized premixed pre- vaporized combustion at 11kW?**

   The modifications proposed focused on the mixing performance and heating power required for a premixed pre-vaporized swirl stabilized burner. Based on literature explored, mixing performance can be optimized by ensuring sufficient maximum jet penetration depth for mixture injected in a jet in co-flow configuration.

Required heating power was determined by estimating heat loss through convection and radiation for the system, which was further adjusted through a correction factor based on systems used in literature. From these two aspects, it was determined that $20\%$ of the combustion air should be used as a carrier gas to vaporize the fuel, $5\%$ of the air for AAI, and the remaining $75\%$ injected through the plenum. Fuel ports through which the air and gaseous fuel mixture are injected are sized at 4mm, to maintain a sufficiently high jet penetration depth, while at the same time the flow is sufficiently far from being choked.

The thesis characterizes the emission and flame speed of jet-A1 blended with HPO and hydrogen in a laminar bunsen flame. Further research on the influence of the blends on burning characteristics of the blends are still required to ensure sufficient drop-in characteristics. This could include experiments conducted in a swirl-stabilized burner as proposed in the final chapter of this thesis. A test conducted with actual gas turbines would also be useful in understanding the actual emission performance of the fuel. This would also a step that is required by regulations to get the production pathway certified.

# References


1. Thomas K. Walker III Marika Tatsutani, J. L. *Decarbonizing Aviation: Enabling Technologies for a Net-Zero Future* tech. rep. (Clean Air Task Force, Apr. 2024).
2. Yusaf, T. *et al.* Sustainable hydrogen energy in aviation – A narrative review. *International Journal of Hydrogen Energy* **52,** 1026–1045. ISSN: 0360-3199. https://www.sciencedirect.com/science/article/pii/S0360319923009187 (2024).
3. Lee, D. *et al.* The contribution of global aviation to anthropogenic climate forcing for 2000 to 2018. *Atmospheric Environment* **244,** 117834. ISSN: 1352-2310. https://www.sciencedirect.com/science/article/pii/S1352231020305689 (2021).
4. Lee, D. *et al.* Transport impacts on atmosphere and climate: Aviation. *Atmospheric Environment* **44.** Transport Impacts on Atmosphere and Climate: The ATTICA Assessment Report, 4678–4734. ISSN: 1352-2310. https://www.sciencedirect.com/science/article/pii/S1352231009004956 (2010).
5. Grewe, V. *et al.* Evaluating the climate impact of aviation emission scenarios towards the Paris agreement including COVID-19 effects. *Nature Communications* **12.** ISSN: 2041-1723. http://dx.doi.org/10.1038/s41467-021-24091-y (June 2021).
6. Abrantes, I., Ferreira, A. F., Silva, A. & Costa, M. Sustainable aviation fuels and imminent technologies - CO2 emissions evolution towards 2050. *Journal of Cleaner Production* **313,** 127937. ISSN: 0959-6526. https://www.sciencedirect.com/science/article/pii/S0959652621021557 (2021).
7. Owen, B., Lee, D. S. & Lim, L. Flying into the Future: Aviation Emissions Scenarios to 2050. *Environmental Science & Technology* **44,** 2255–2260. ISSN: 1520-5851. http://dx.doi.org/10.1021/es902530z (Mar. 2010).
8. Massaro, M. C. *et al.* Potential and technical challenges of on-board hydrogen storage technologies coupled with fuel cell systems for aircraft electrification. *Journal of Power Sources* **555,** 232397. ISSN: 0378-7753. https://www.sciencedirect.com/science/article/pii/S0378775322013742X (2023).
9. Quante, G., Bullerdiek, N., Bube, S., Neuling, U. & Kaltschmitt, M. Renewable fuel options for aviation – A System-Wide comparison of Drop-In and non Drop-In fuel options. *Fuel* **333,** 126269. ISSN: 0016-2361. https://www.sciencedirect.com/science/article/pii/S0016236122030939 (2023).
10. Undavalli, V. *et al.* Recent advancements in sustainable aviation fuels. *Progress in Aerospace Sciences* **136,** 100876. ISSN: 0376-0421. https://www.sciencedirect.com/science/article/pii/S0376042122000689 (2023).
11. Manigandan, S., Praveenkumar, T., Ir Ryu, J., Nath Verma, T. & Pugazhendhi, A. Role of hydrogen on aviation sector: A review on hydrogen storage, fuel flexibility, flame stability, and emissions reduction on gas turbines engines. *Fuel* **352,** 129064. ISSN: 0016-2361. https://www.sciencedirect.com/science/article/pii/S0016236123016770 (2023).
12. Maull, L. *Boeing Company - Boeing publicly launches "Cascade" to support ...* Accessed 17 March 2024. May 2023. https://investors.boeing.com/investors/news/press-release-details/2023/Boeing-Publicly-Launches-Cascade-to-Support-Aviations-Net-Zero-Goal/default.aspx.
13. Standard Specification for Aviation Turbine Fuel Containing Synthesized Hydrocarbons. **D7566-23b** (2023).
14. Dahman, Y., Syed, K., Begum, S., Roy, P. & Mohtasebi, B. in *Biomass, Biopolymer-Based Materials, and Bioenergy* 277–325 (Elsevier, 2019). http://dx.doi.org/10.1016/B978-0-08-102426-3.00014-X.

15. *Sustainable Aviation Fuels Technology Basics* https://skynrg.com/sustainable-aviation-fuel/technology-basics/. [Accessed 10-04-2024].

16. Sathendra, E. R., Praveenkumar, R., Gurunathan, B., Chozhavendhan, S. & Jayakumar, M. in *Biofuels and Bioenergy* (eds Gurunathan, B., Sahadevan, R. & Zakaria, Z. A.) 87–110 (Elsevier, 2022). ISBN: 978-0-323-85269-2. https://www.sciencedirect.com/science/article/pii/B9780323852692000162.

17. Su, G., Ong, H. C., Mofijur, M., Mahlia, T. I. & Ok, Y. S. Pyrolysis of waste oils for the production of biofuels: A critical review. *Journal of Hazardous Materials* **424,** 127396. ISSN: 0304-3894. https://www.sciencedirect.com/science/article/pii/S0304389421023645 (2022).

18. Palies, P. *Stabilization and dynamic of premixed swirling flames* (Academic Press, San Diego, CA, July 2020).

19. *The in-service performance of the Trent XWB* Accessed 19-03-2024. Dec. 2019. https://www.aircraft-commerce.com/wp-content/uploads/aircraft-commerce-docs1/General%20Articles/2019/127_MTCE_B.pdf.

20. Endicott, D. S. *Experimental Development of a Lean Direct Injection Combustor Utilizing High-Low Swirl Intensity Combinations* in (2014). https://api.semanticscholar.org/CorpusID:138860678.

21. Liu, Y. *et al.* Review of modern low emissions combustion technologies for aero gas turbine engines. *Progress in Aerospace Sciences* **94,** 12–45. ISSN: 0376-0421. https://www.sciencedirect.com/science/article/pii/S037604211630118X (2017).

22. McKinney, R., Cheung, A., Sowa, W. & Sepulveda, D. *The Pratt & Whitney TALON X Low Emissions Combustor: Revolutionary Results with Evolutionary Technology* in. **7** (Jan. 2007). ISBN: 978-1-62410-012-3.

23. Standard Practice for Evaluation of New Aviation Turbine Fuels and Fuel Additives. *ASTM* **D4054-22** (2022).

24. Liu, Z., Wang, Z. & Yang, X. Emission characteristics of cellulosic jet biofuel blend under laminar and turbulent combustion. *Biotechnology for Biofuels and Bioproducts* **16** (Dec. 2023).

25. Khandelwal, B., Cronly, J., Ahmed, I., Wijesinghe, C. & Lewis, C. The effect of alternative fuels on gaseous and particulate matter (PM) emission performance in an auxiliary power unit (APU). *The Aeronautical Journal* **123,** 617–634 (2019).

26. Khandelwal, B., Wijesinghe, C. & Sriraman, S. *Effect of Alternative Fuels on Emissions and Engine Compatibility* 27–50. ISBN: 978-981-10-7472-1 (July 2018).

27. Corporan, E., DeWitt, M. J., Klingshirn, C. D., Striebich, R. & Cheng, M.-D. Emissions Characteristics of Military Helicopter Engines with JP-8 and Fischer-Tropsch Fuels. *Journal of Propulsion and Power* **26,** 317–324. https://doi.org/10.2514/1.43928 (2010).

28. Timko, M. T. *et al.* Particulate Emissions of Gas Turbine Engine Combustion of a Fischer−Tropsch Synthetic Fuel. *Energy & Fuels* **24,** 5883–5896. ISSN: 1520-5029. http://dx.doi.org/10.1021/ef100727t (Nov. 2010).

29. Corporan, E., DeWitt, M. J., Klingshirn, C. D. & Anneken, D. *ALTERNATIVE FUELS TESTS ON A C-17 AIRCRAFT: EMISSIONS CHARACTERISTICS* tech. rep. (Air Force Research Laboratory, Propulsion Directorate Wright-Patterson Air Force Base, 2010).

30. Riebl, S., Braun-Unkhoff, M. & Riedel, U. A Study on the Emissions of Alternative Aviation Fuels. *Journal of Engineering for Gas Turbines and Power* **139.** ISSN: 1528-8919. http://dx.doi.org/10.1115/1.4035816 (Mar. 2017).

31. Lobo, P. *et al.* Impact of Alternative Fuels on Emissions Characteristics of a Gas Turbine Engine - Part 1: Gaseous and Particulate Matter Emissions. *Environmental science & technology* **46,** 10805–11 (Aug. 2012).

32. Gokulakrishnan, P. & Klassen, M. S. in *Renewable Fuels* 451–484 (Cambridge University Press, Nov. 2022). ISBN: 9781316512883. http://dx.doi.org/10.1017/9781009072366.017.

33. Liu, Y., Tan, J., Wan, M. & Yao, X. OH* and CH* chemiluminescence characteristics in low swirl methane-air flames. *AIP Advances* **10.** ISSN: 2158-3226. http://dx.doi.org/10.1063/5.0002660 (May 2020).

34. Long, E. J. & Hargrave, G. K. Experimental Measurement of Local Burning Velocity Within a Rotating Flow. *Flow, Turbulence and Combustion* **86,** 455–476. ISSN: 1573-1987. http://dx.doi.org/10.1007/s10494-011-9331-6 (Mar. 2011).

35. Zhang, W. *et al.* Investigation of the fuel effects on burning velocity and flame structure of turbulent premixed flames based on leading points concept. *Combustion Science and Technology* **190,** 1354–1376. ISSN: 1563-521X. http://dx.doi.org/10.1080/00102202.2018.1451848 (Mar. 2018).

36. Griebel, P., Siewert, P. & Jansohn, P. Flame characteristics of turbulent lean premixed methane/air flames at high pressure: Turbulent flame speed and flame brush thickness. *Proceedings of the Combustion Institute* **31,** 3083–3090. ISSN: 1540-7489. http://dx.doi.org/10.1016/j.proci.2006.07.042 (Jan. 2007).

37. Daniele, S., Jansohn, P. & Boulouchos, K. *Flame Front Characteristic and Turbulent Flame Speed of Lean Premixed Syngas Combustion at Gas Turbine Relevant Conditions* in *Volume 2: Combustion, Fuels and Emissions* (ASMEDC, Jan. 2009). http://dx.doi.org/10.1115/gt2009-59477.

38. Daniele, S., Mantzaras, J., Jansohn, P., Denisov, A. & Boulouchos, K. Flame front/turbulence interaction for syngas fuels in the thin reaction zones regime: turbulent and stretched laminar flame speeds at elevated pressures and temperatures. *Journal of Fluid Mechanics* **724,** 36–68. ISSN: 1469-7645. http://dx.doi.org/10.1017/jfm.2013.141 (Apr. 2013).

39. Griebel, P. *et al. Flame Characteristics and Turbulent Flame Speeds of Turbulent, High-Pressure, Lean Premixed Methane/Air Flames* in *Volume 2: Turbo Expo 2005* (ASMEDC, Jan. 2005). http://dx.doi.org/10.1115/gt2005-68565.

40. Zhang, M. *et al.* Flame front structure and burning velocity of turbulent premixed CH4/H2/air flames. *International Journal of Hydrogen Energy* **38,** 11421–11428. ISSN: 0360-3199. http://dx.doi.org/10.1016/j.ijhydene.2013.05.051 (Aug. 2013).

41. Hwang, B. J., Kang, S., Lee, H. J. & Min, S. Measurement of laminar burning velocity of high performance alternative aviation fuels. *Fuel* **261,** 116466. ISSN: 0016-2361. http://dx.doi.org/10.1016/j.fuel.2019.116466 (Feb. 2020).

42. Filatyev, S., Thariyan, M., Lucht, R. & Gore, J. *Application of Simultaneous Stereo PIV and Double Pulsed Acetone PLIF to Study Turbulent Premixed Flames* in *45th AIAA Aerospace Sciences Meeting and Exhibit* (American Institute of Aeronautics and Astronautics, Jan. 2007). http://dx.doi.org/10.2514/6.2007-1346.

43. Beerer, D., McDonell, V., Therkelsen, P. & Cheng, R. K. Flashback and Turbulent Flame Speed Measurements in Hydrogen/Methane Flames Stabilized by a Low-Swirl Injector at Elevated Pressures and Temperatures. *Journal of Engineering for Gas Turbines and Power* **136,** 031502. ISSN: 0742-4795. https://doi.org/10.1115/1.4025636 (Nov. 2013).

44. Plessing, T., Kortschik, C., Peters, N., Mansour, M. & Cheng, R. Measurements of the turbulent burning velocity and the structure of premixed flames on a low-swirl burner. *Proceedings of the Combustion Institute* **28,** 359–366. ISSN: 1540-7489. https://www.sciencedirect.com/science/article/pii/S0082078400802313 (2000).

45. Marshall, A., Lundrigan, J., Venkateswaran, P., Seitzman, J. & Lieuwen, T. Measurements of Stretch Statistics at Flame Leading Points for High Hydrogen Content Fuels. *Journal of Engineering for Gas Turbines and Power* **139,** 111503. ISSN: 0742-4795. eprint: https://asmedigitalcollection.asme.org/gasturbinespower/article-pdf/139/11/111503/6175992/gtp_139_11_111503.pdf. https://doi.org/10.1115/1.4035819 (July 2017).

46. Muruganandam, T. M. & Seitzman, J. M. Fluid Mechanics of Lean Blowout Precursors in Gas Turbine Combustors. *International Journal of Spray and Combustion Dynamics* **4,** 29–60 (2012).

47. Grohmann, J., Rauch, B., Kathrotia, T., Meier, W. & Aigner, M. Influence of Single-Component Fuels on Gas-Turbine Model Combustor Lean Blowout. *Journal of Propulsion and Power* **34,** 97–107. ISSN: 1533-3876. http://dx.doi.org/10.2514/1.B36456 (Jan. 2018).

48. Lefebvre, A. H. Fuel Effects on Gas Turbine Combustion—Ignition, Stability, and Combustion Efficiency. *Journal of Engineering for Gas Turbines and Power* **107,** 24–37. ISSN: 1528-8919. http://dx.doi.org/10.1115/1.3239693 (Jan. 1985).

49. Huelskamp, B. C., Kiel, B. V. & Gokulakrishnan, P. *Influence of Fuel Characteristics in a Correlation to Predict Lean Blowout of Bluff-Body Stabilized Flames* in *Volume 4B: Combustion, Fuels and Emissions* (American Society of Mechanical Engineers, June 2015). http://dx.doi.org/10.1115/GT2015-43433.

50. Rock, N., Emerson, B., Seitzman, J. & Lieuwen, T. Near-lean blowoff dynamics in a liquid fueled combustor. *Combustion and Flame* **212,** 53–66. ISSN: 0010-2180. http://dx.doi.org/10.1016/j.combustflame.2019.10.010 (Feb. 2020).

51. Rock, N. *et al.* Liquid Fuel Property Effects on Lean Blowout in an Aircraft Relevant Combustor. *Journal of Engineering for Gas Turbines and Power* **141.** ISSN: 1528-8919. http://dx.doi.org/10.1115/1.4042010 (Jan. 2019).

52. Huelskamp, B., Monfort, J., Kiel, B. V., Neuroth, C. & Caswell, A. W. *Comparison of Alternative Jet Fuel Lean Blowouts for Bluff-Body Stabilized Flames* in *54th AIAA Aerospace Sciences Meeting* (American Institute of Aeronautics and Astronautics, Jan. 2016). http://dx.doi.org/10.2514/6.2016-0450.

53. Liu, Y. *et al.* Review of modern low emissions combustion technologies for aero gas turbine engines. *Progress in Aerospace Sciences* **94,** 12–45. ISSN: 0376-0421. http://dx.doi.org/10.1016/j.paerosci.2017.08.001 (Oct. 2017).

54. Verma, H. K., Kumar, A., Kumar, K. & Mohammed, R. *Flashback and Lean Blow Out Study of a Lean Premixed Pre-Vaporized Can Combustor* in *Volume 1: Compressors, Fans and Pumps; Turbines; Heat Transfer; Combustion, Fuels and Emissions* (American Society of Mechanical Engineers, Dec. 2017). http://dx.doi.org/10.1115/GTINDIA2017-4642.

55. Choudhuri, A. *Effects of Combustion-Induced Vortex Breakdown on Flashback Limits of Syngas-Fueled Gas Turbine Combustors* http://dx.doi.org/10.2172/1025558 (Mar. 2011).

56. Fritz, J., Kro¨ner, M. & Sattelmayer, T. Flashback in a Swirl Burner With Cylindrical Premixing Zone. *Journal of Engineering for Gas Turbines and Power* **126,** 276–283. ISSN: 1528-8919. http://dx.doi.org/10.1115/1.1473155 (Apr. 2004).

57. Boushaki, T. in *Swirling Flows and Flames* (ed Boushaki, T.) chap. 1 (IntechOpen, Rijeka, 2019). https://doi.org/10.5772/intechopen.86495.

58. Smith, L., Karim, H., Etemad, S. & Pfefferle, W. C. *The Gas Turbine Handbook* Book 3 (National Energy Technology Laboratory, 2006).

59. Van den Bergh, A. *Swirl Stabilized Combustor with Axial Air Injection* June 2022.

60. J. M. Beér, N. A. C. *Combustion aerodynamics* (Krieger, 1972).

61. Steenbergen, W. & Voskamp, J. The rate of decay of swirl in turbulent pipe flow. English. *Flow Measurement and Instrumentation* **9,** 67–78. ISSN: 0955-5986 (1998).

62. Vermeijlen, S. *Swirl-Stabilised Hydrogen Combustor with Axial Air Injection* 2021.

63. Chen, X., Wang, H., Wang, X., Liu, X. & Zhu, Y. Fuel/air mixing characteristics of a Micromix burner for hydrogen-rich gas turbine. *Energy* **282,** 128786. ISSN: 0360-5442. http://dx.doi.org/10.1016/j.energy.2023.128786 (Nov. 2023).

64. Chen, X. *et al.* Numerical investigation into fuel–air mixing characteristics and cold flow field of single hydrogen-rich Micromix nozzle. *Fuel* **332,** 126181. ISSN: 0016-2361. http://dx.doi.org/10.1016/j.fuel.2022.126181 (Jan. 2023).

65. Nagao, T., Matsuno, S. & Hayashi, A. Effect of Cross-flow Momentum on Opposing Jet Mixing. *International Journal of Gas Turbine, Propulsion and Power Systems* **6,** 1–8 (2014).

66. KROLL, J., SOWA, W., SAMUELSEN, G. & HOLDEMAN, J. *Optimization of circular orifice jets mixing into a heated crossflowin a cylindrical duct* in *31st Aerospace Sciences Meeting* (American Institute of Aeronautics and Astronautics, Jan. 1993). http://dx.doi.org/10.2514/6.1993-249.

67. *VDI Heat Atlas* (ed Stephan, P. D.-I. P.) (Springer Berlin Heidelberg, 2010).

68. Best, T., Finney, K., Ingham, D. & Pourkashanian, M. Impact of CO2-enriched combustion air on micro-gas turbine performance for carbon capture. *Energy* **115,** 1138–1147 (Nov. 2016).
69. El-Zoheiry, R. M., EL-Seesy, A. I., Attia, A. M., He, Z. & El-Batsh, H. M. Combustion and emission characteristics of Jojoba biodiesel-jet A1 mixtures applying a lean premixed pre-vaporized combustion techniques: An experimental investigation. *Renewable Energy* **162,** 2227–2245. ISSN: 0960-1481. http://dx.doi.org/10.1016/j.renene.2020.10.031 (Dec. 2020).
70. Wang, H. *et al.* A physics-based approach to modeling real-fuel combustion chemistry - I. Evidence from experiments, and thermodynamic, chemical kinetic and statistical considerations. *Combustion and Flame* **193,** 502–519. ISSN: 0010-2180. http://dx.doi.org/10.1016/j.combustflame.2018.03.019 (July 2018).
71. Xu, R. *et al.* A physics-based approach to modeling real-fuel combustion chemistry – II. Reaction kinetic models of jet and rocket fuels. *Combustion and Flame* **193,** 520–537. ISSN: 0010-2180. http://dx.doi.org/10.1016/j.combustflame.2018.03.021 (July 2018).
72. Edwards, J. T. *Reference Jet Fuels for Combustion Testing* in *55th AIAA Aerospace Sciences Meeting* (American Institute of Aeronautics and Astronautics, Jan. 2017). http://dx.doi.org/10.2514/6.2017-0146.
73. *Continuously Stirred Tank Reactor* @misc{ContinuouslyStirredTankReactor-Cantera3.2.0a1documentation}. [Accessed 20-02-2025]. https://cantera.org/dev/examples/python/reactors/continuous_reactor.html.
74. Van Dalen, S. *Chemical Kinetics of Hydrogen-assisted Combustion of Kerosene* 2024.
75. Petrov, V. & Reznik, V. Measurement of the emissivity of quartz glass. *High Temperatures-High Pressures* **v. 4,** pp. 687–693 (Jan. 1972).
76. Barnes, B. T., Forsythe, W. E. & Adams, E. Q. The Total Emissivity of Various Materials at 100–500°C. *Journal of the Optical Society of America* **37,** 804. ISSN: 0030-3941. http://dx.doi.org/10.1364/josa.37.000804 (Oct. 1947).
77. Buffi, M., Cappelletti, A., Rizzo, A. M., Martelli, F. & Chiaramonti, D. Combustion of fast pyrolysis bio-oil and blends in a micro gas turbine. *Biomass and Bioenergy* **115,** 174–185. ISSN: 0961-9534. http://dx.doi.org/10.1016/j.biombioe.2018.04.020 (Aug. 2018).
78. Broumand, M., Khan, M. S., Yun, S., Hong, Z. & Thomson, M. J. Feasibility of running a micro gas turbine on wood-derived fast pyrolysis bio-oils: Effect of the fuel spray formation and preparation. *Renewable Energy* **178,** 775–784. ISSN: 0960-1481. http://dx.doi.org/10.1016/j.renene.2021.06.105 (Nov. 2021).
79. Frenillot, J., Cabot, G., Cazalens, M., Renou, B. & Boukhalfa, M. Impact of H2 addition on flame stability and pollutant emissions for an atmospheric kerosene/air swirled flame of laboratory scaled gas turbine. *International Journal of Hydrogen Energy* **34,** 3930–3944. ISSN: 0360-3199. http://dx.doi.org/10.1016/j.ijhydene.2009.02.059 (May 2009).
80. Konnov, A. A. *et al.* A comprehensive review of measurements and data analysis of laminar burning velocities for various fuel+air mixtures. *Progress in Energy and Combustion Science* **68,** 197–267. ISSN: 0360-1285. http://dx.doi.org/10.1016/j.pecs.2018.05.003 (Sept. 2018).
81. Wu, Y., Modica, V., Rossow, B. & Grisch, F. Effects of pressure and preheating temperature on the laminar flame speed of methane/air and acetone/air mixtures. *Fuel* **185,** 577–588. ISSN: 0016-2361. http://dx.doi.org/10.1016/j.fuel.2016.07.110 (Dec. 2016).
82. Natarajan, J., Lieuwen, T. & Seitzman, J. Laminar flame speeds of H2/CO mixtures: Effect of CO2 dilution, preheat temperature, and pressure. *Combustion and Flame* **151,** 104–119. ISSN: 0010-2180. http://dx.doi.org/10.1016/j.combustflame.2007.05.003 (Oct. 2007).
83. Zhang, X. *et al.* Laminar flame speed modeling of pre-vaporized jet fuel/hydrogen mixtures under engine conditions. *Fuel* **380,** 133149. ISSN: 0016-2361. http://dx.doi.org/10.1016/j.fuel.2024.133149 (Jan. 2025).
84. Chong, C. T. & Hochgreb, S. Measurements of laminar flame speeds of liquid fuels: Jet-A1, diesel, palm methyl esters and blends using particle imaging velocimetry (PIV). *Proceedings of the Combustion Institute* **33,** 979–986. ISSN: 1540-7489. http://dx.doi.org/10.1016/j.proci.2010.05.106 (2011).

85. Wu, Y., Modica, V., Yu, X. & Grisch, F. Experimental Investigation of Laminar Flame Speed Measurement for Kerosene Fuels: Jet A-1, Surrogate Fuel, and Its Pure Components. *Energy & Fuels* **32,** 2332–2343. ISSN: 1520-5029. http://dx.doi.org/10.1021/acs.energyfuels.7b02731 (Jan. 2018).

86. Kick, T. *et al.* An experimental and modeling study of burning velocities of possible future synthetic jet fuels. *Energy* **43,** 111–123. ISSN: 0360-5442. http://dx.doi.org/10.1016/j.energy.2012.01.035 (July 2012).

87. Richter, S. *et al.* Experimental and modeling study of farnesane. *Fuel* **215,** 22–29. ISSN: 0016-2361. http://dx.doi.org/10.1016/j.fuel.2017.10.117 (Mar. 2018).

88. Vukadinovic, V., Habisreuther, P. & Zarzalis, N. Experimental Study on Combustion Characteristics of Conventional and Alternative Liquid Fuels. *Journal of Engineering for Gas Turbines and Power* **134.** ISSN: 1528-8919. http://dx.doi.org/10.1115/1.4007333 (Oct. 2012).

89. Vukadinovic, V., Habisreuther, P. & Zarzalis, N. Influence of pressure and temperature on laminar burning velocity and Markstein number of kerosene Jet A-1: Experimental and numerical study. *Fuel* **111,** 401–410. ISSN: 0016-2361. http://dx.doi.org/10.1016/j.fuel.2013.03.076 (Sept. 2013).

90. Le Dortz, R., Strozzi, C., Sotton, J. & Bellenoue, M. Evaluation of the surrogates capacity to reproduce the laminar burning velocities and the sensitivity to stretching of a commercial kerosene under constant volume combustion conditions. *Fuel* **287,** 119426. ISSN: 0016-2361. http://dx.doi.org/10.1016/j.fuel.2020.119426 (Mar. 2021).

91. Alkhalifa, A., Bonebrake, J. & Blunck, D. L. *Effects of thermal stressing on the turbulent flame speed of jet fuel* in *AIAA Scitech 2020 Forum* (American Institute of Aeronautics and Astronautics, Jan. 2020). http://dx.doi.org/10.2514/6.2020-2276.

92. Schorn, N., Bonebrake, J. M., Pendergrass, B., Fillo, A. & Blunck, D. L. *Turbulent Consumption Speed of Large Hydrocarbon Fuels at Sub-Atmospheric Conditions* in *AIAA Scitech 2019 Forum* (American Institute of Aeronautics and Astronautics, Jan. 2019). http://dx.doi.org/10.2514/6.2019-0735.

93. Fillo, A. J., Bonebrake, J. & Blunck, D. L. *Impact of fuel chemistry on the global consumption speed of large hydrocarbon fuel/air flames* 2022. https://arxiv.org/abs/2201.00102.

94. Wang, T.-S. Thermophysics Characterization of Kerosene Combustion. *Journal of Thermophysics and Heat Transfer* **15** (May 2001).

95. Mills, A. F. *Heat Transfer* (McGraw-Hill, New York, NY, Dec. 1992).

96. Masoud, S. M., Attia, A. M., Salem, H. & El-Zoheiry, R. M. Investigation of jet A-1 and waste cooking oil biodiesel fuel blend flame characteristics stabilized by radial swirler in lean pre-vaporized premixed combustor. *Energy* **263,** 125830. ISSN: 0360-5442. http://dx.doi.org/10.1016/j.energy.2022.125830 (Jan. 2023).

97. El-Zoheiry, R. M., EL-Seesy, A. I., Attia, A. M., He, Z. & El-Batsh, H. M. Combustion and emission characteristics of Jojoba biodiesel-jet A1 mixtures applying a lean premixed pre-vaporized combustion techniques: An experimental investigation. *Renewable Energy* **162,** 2227–2245. ISSN: 0960-1481. http://dx.doi.org/10.1016/j.renene.2020.10.031 (Dec. 2020).

98. Attia, A. M., Belal, B. Y., El-Batsh, H. & Moneib, H. Effect of waste cooking oil methyl ester – Jet A-1 fuel blends on emissions and combustion characteristics of a swirl-stabilized lean pre-vaporized premixed flame. *Fuel* **267,** 117203. ISSN: 0016-2361. http://dx.doi.org/10.1016/j.fuel.2020.117203 (May 2020).

# A

# CAD Drawings

**Figure A.1:** Complete System of Proposed Swirl Burner. The long tube on the left is the fuel-prevaporizer system with heater installed horizontally. The AAI line pass through the heater installed vertically on the center, towards the swirler plenum. The main air line is on the right with the vertical heater and injected through an elbow to the swirler plenum.

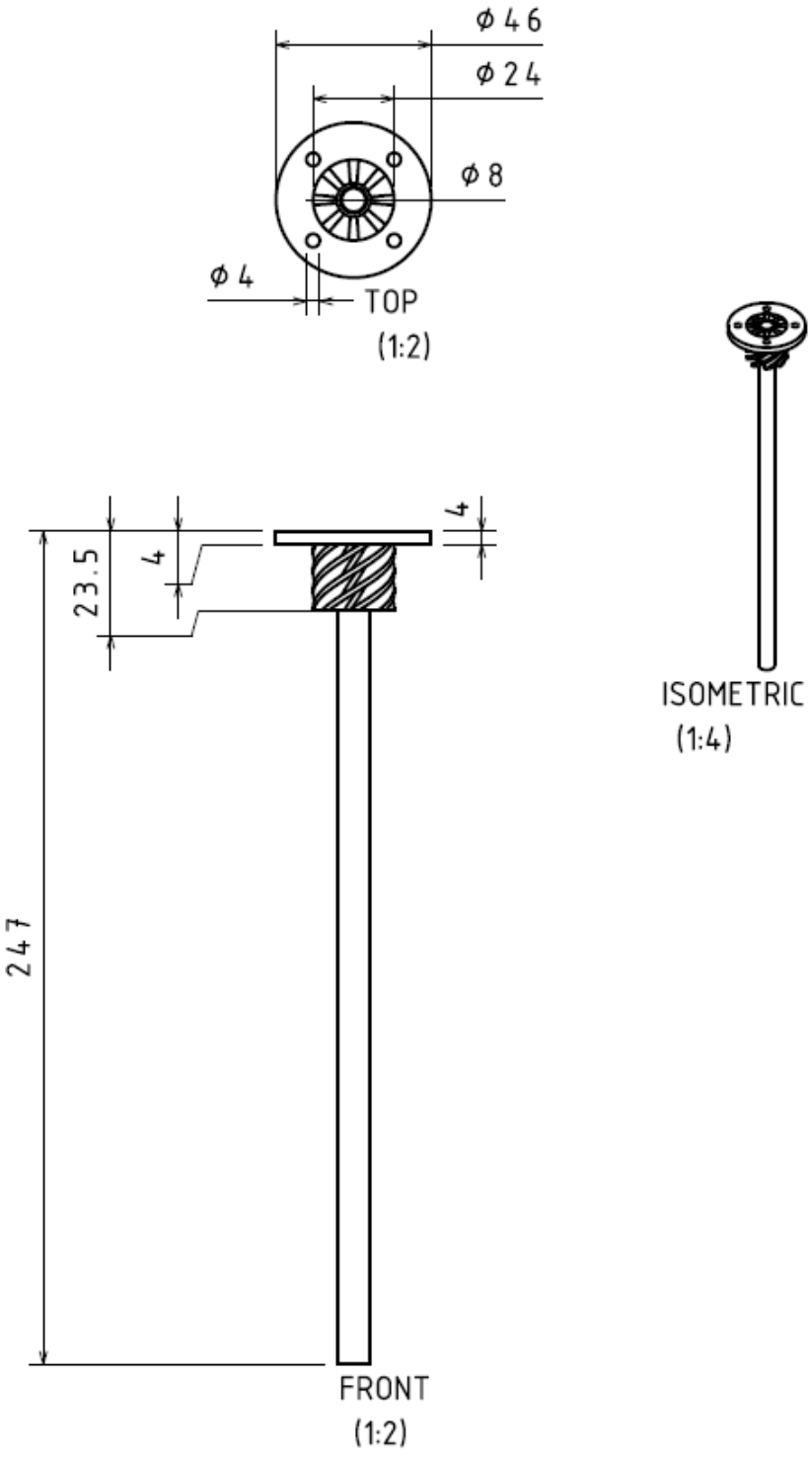


**Figure A.2:** Drawing of Swirler insert.

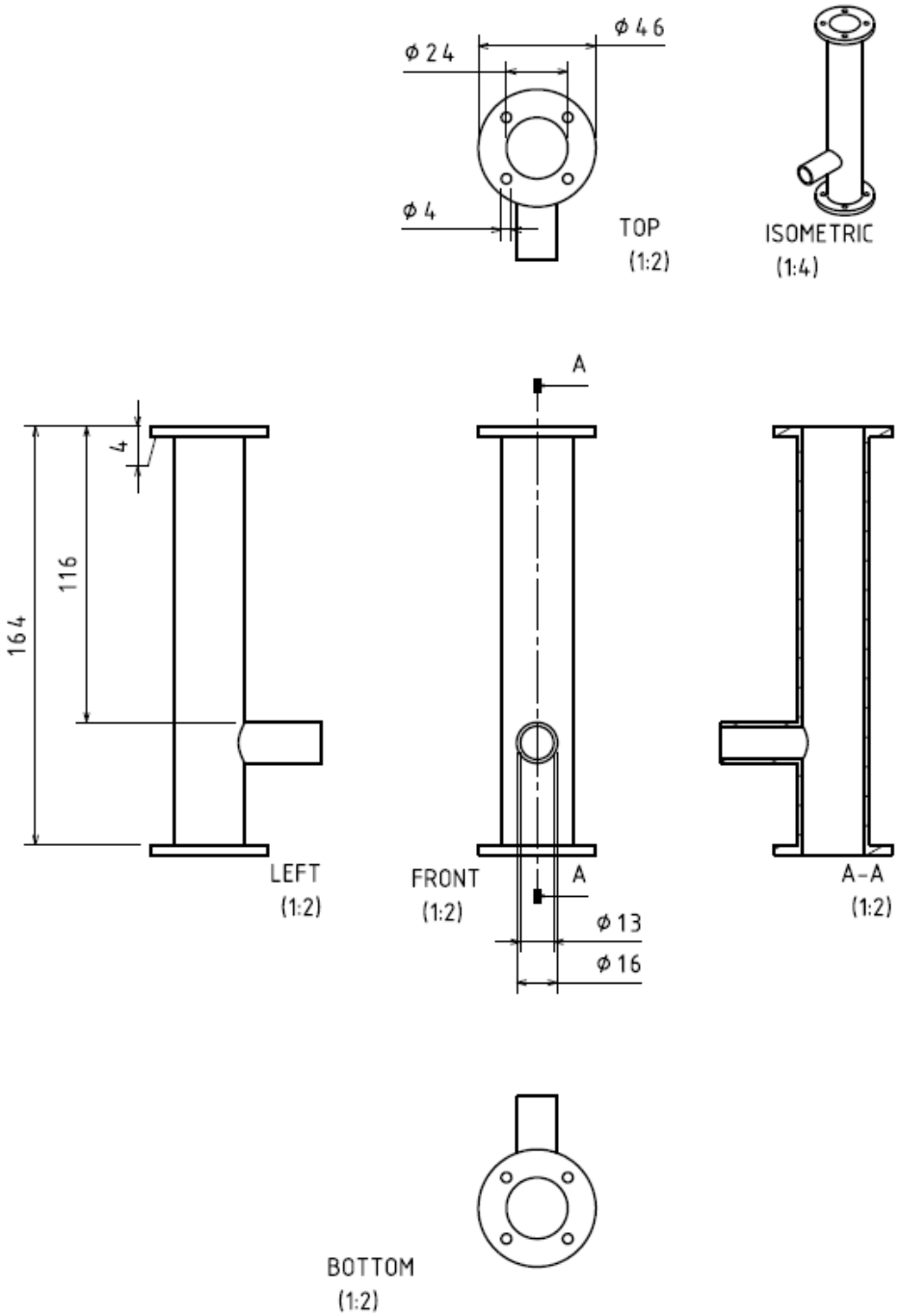


**Figure A.3:** Drawing of plenum housing swirler. The horizontal section shows main air inlet.